BORON NITRIDE AND GRAPHENE 2D NANOSTRUCTURES FROM FIRST-PRINCIPLES

A DISSERTATION

SUBMITTED TO THE DEPARTMENT OF PHYSICS

AND THE INSTITUTE OF ENGINEERING AND SCIENCE

OF BILKENT UNIVERSITY

IN PARTIAL FULFILLMENT OF THE REQUIREMENTS

FOR THE DEGREE OF

DOCTOR OF PHILOSOPHY

By

Rasim Volga Ovalı

September, 2010

I certify that I have read this thesis and that in my opinion it is fully adequate, in scope and in quality, as a dissertation for the degree of doctor of philosophy.

Assoc. Prof. Dr. Oğuz Gülseren(Advisor)

I certify that I have read this thesis and that in my opinion it is fully adequate, in scope and in quality, as a dissertation for the degree of doctor of philosophy.

Assoc. Prof. Dr. M. Özgür Oktel

I certify that I have read this thesis and that in my opinion it is fully adequate, in scope and in quality, as a dissertation for the degree of doctor of philosophy.

Assoc. Prof. Dr. Ceyhun Bulutay

I certify that I have read this thesis and that in my opinion it is fully adequate, in scope and in quality, as a dissertation for the degree of doctor of philosophy.

Assist. Prof. Dr. Erman Bengü

I certify that I have read this thesis and that in my opinion it is fully adequate, in scope and in quality, as a dissertation for the degree of doctor of philosophy.

Assoc. Prof. Dr. Engin Özdaş

Approved for the Institute of Engineering and Science:

Prof. Dr. Levent Onural
Director of the Institute

ABSTRACT

BORON NITRIDE AND GRAPHENE 2D NANOSTRUCTURES FROM FIRST-PRINCIPLES

Rasim Volga Ovalı
PhD. in Physics
Supervisor: Assoc. Prof. Dr. Oğuz Gülseren
September, 2010

In this thesis, the structures as well as mechanical and electronic properties of various boron nitride (BN) and graphene based two dimensional (2D) nano-structures are investigated in detail from first-principle calculations using planewave pseudopotential method based on density functional theory.

At the beginning of the thesis, essentials of the density functional theory (DFT) and a guidance for performing ab-initio calculations in the framework of DFT is presented. In addition, fundamentals about the exchange-correlation potential as well as approaches approximating it like local density approximation (LDA) and generalized gradient approximation (GGA) are discussed.

Along with this thesis, first of all, in order to understand the relation between the hexagonal boron nitride (h-BN) and cubic boron nitride (c-BN) and the growth of three dimensional (3D) BN structures, various defect structures introduce to BN monolayer, including point defects and especially highly curved defects such as n-fold rings, are investigated in detail. The calculated formation energies and structural analysis showed that 4-fold BN rings are the transient phase between h-BN to c-BN during c-BN nucleation. The charge density plots and density of states analysis further provide information about the electronic structure of these defect formations.

Second of all, we have studied the formation of boron-nitride-carbon (BNC) ternary thin films, so we observed the carbon nucleation in BN monolayer. These DFT based calculations show that carbon prefers the nitrogen site at first step and the calculated defect energy indicates that carbon atoms tends to aggregate in BN hexagonal network, and hence increases the number of C-C bonds. BNC structures have magnetization of μ=1.0μ_B for odd number of carbon adsorption. Further substitution of carbon atoms into BN layer showed that carbon atoms

form hexagonal rings instead of armchair or zigzag formations. Moreover, we calculated the vibrational modes of BN monolayer and BNC structures, and phonon density of states graphs are presented. The phonon frequencies intrinsic to C-C bond oscillations are observed, which is in good agreement with the experiment.

Finally, point defects and ring formations on graphene are investigated in order to understand the Y-junction and kink formation in carbon nanotubes (CNTs). Pentagonal rings are the good candidates to initiate such 2D networks in CNTs. The curvature increases with increasing number of pentagonal rings. Moreover, interaction of sulphur atoms with graphene defects is studied. Final geometries and binding energies suggest that sulphur prefers to adsorb on defected regions, but it is not responsible for the formation of these structures or defects.

Keywords: Boron nitride, graphene, carbon nanotubes, sulphur, point defects, vacancies, highly curved defects, n-fold rings, Y-junction, ab-initio, density functional theory .

ÖZET

BORON NİTRÜR VE GRAFEN İKİ BOYUTLU NANOYAPILARIN TEMEL PRENSİPLER METODU İLE İNCELENMESİ

Rasim Volga Ovalı
Fizik, Doktora
Tez Yöneticisi: Doç. Dr. Oğuz Gülseren
Eylül, 2010

Bu tezde, çeşitli boron nitrür ve grafen tabanlı iki boyutlu (2B) nano-yapılarının geometrik yapıları ve bunların mekanik ve elektronik özellikleri yoğunluk fonksiyoneli teorisine (YFT) dayanan düzlem dalga sanki potansiyel metodu kullanılarak temel prensipler hesapları ile incelendi.

Bu hesaplamalar yoğunluk fonksiyoneli teorisine (YFT) dayanmaktadır. Bu yüzden bu tezin giriş bölümünde yoğunluk fonksiyoneli teorisinin ana hatları özetlenerek hesaplamalarda kullanılan metodlara yer verildi. Özellikle kullanımı kritik olan değiş-tokuş potansiyelinin genel özellikleri ve bunun tarifinde kullanılan yerel yoğunluk yaklaşımı (LDA) ve genelleştirilmiş gradyant yaklaşımı (GGA) tartışıldı.

İlk olarak kübik boron nitrür (c-BN) ve heksagonal boron nitrür (h-BN) yapıları arasındaki ilişki ve buradan yola çıkarak üç boyutlu (3B) boron nitrür yapıların büyüme modellerini anlamak için tek katmanlı boron nitrür üzerinde oluşabilecek çeşitli kusur yapıları ele alındı. Formasyon enerjileri ve yapı analizleri sonucunda 4-yanlı BN halkanın kübik-BN sentezi sırasında altıgen-BN ile kübik-BN arasında geçiş fazı olduğu görüldü. Bu kusur yapıları ile alakalı yük yoğunlukları ve durum yoğunlukları çıkartılarak bu yapıların elektronik özellikleri incelendi.

İkinci olarak, boron-azot-karbon üçlü ince filimlerin oluşumunu anlamak üzere tek katmanlı BN yapılarına karbon katışma etkileri incelendi. YFT hesaplarına dayanarak eklenen ilk karbon atomunun azot atomunun yerine geçmek istediği gözlemlendi. Sisteme daha fazla karbon katılması durumunda karbon atomlarının bir araya geldiği ve karbon-karbon bağı sayısının arttığı görüldü. Altı karbon ve

on karbon ile yapılan hesaplarda boron nitrür yapısı içindeki karbon atomları halka yapıları oluşturdu. Ayrıca, yine bu sistemler için salınım modları hesaplandı. Bunun sonucunda belirli enerji aralıklarında karbon-karbon bağından kaynaklanan salınımlar gözlemlendi.

Üçüncü olarak, grafen yapısında bulunabilecek kusur oluşumları incelendi. Bunlar arasında beşgen yüzük yapısının karbon nanotüp sentezi sırasında sıkça görülen Y- ve T- kavşak oluşumlarına temel olabileceği anlaşıldı. Ayrıca beşgen halka sayısı arttıkça yapıdaki kavislenme arttı. Son olarak, sülfür ve kusurlu grafen yapıları arasındaki etkileşme incelendi. Sülfür atomunun kusurlu bölgelere tutunduğu fakat bu tutunmanın grafen üzerinde kavisli yapı oluşturmadığı anlaşıldı.

Anahtar sözcükler: Boron nitrür, grafen, karbon nanotüpler, sülfür, noktasal kusurlar, eksiklikler, yüksek kavisli kusurlar, n-yanlı halkalar, T- kavşağı, ilk prensipler metodu, yoğunluk fonksiyoneli teorisi .

Acknowledgement

I am indebted to Assoc. Prof. Dr. Oğuz Gülseren for constant help, support and encouragement as a supervisor during my PhD.

I would like to thank Assist. Prof. Dr. Erman Bengü for valuable, informative and educative discussions.

I am grateful to my colleagues Dr. Deniz Çakır, Selcen İslamoğlu, Kurtuluş Abak, Cem Murat Turgut, Dr. Engin Durgun, Dr. Haldun Sevinçli, Dr. Sevilay Sevinçli, Dr. Levent Subaşı, Dr. Mehmet Emre Taşgın, Dr. Onur Umucalılar, Hüseyin Şener Şen, Dr. Selin Damla Ahıpaşaoğlu and Dr. Cem Sevik for their help and invaluable friendship.

And finally I would like to thank my family for their great support.

Contents

List of Figures

List of Tables

Chapter 1

Introduction

Boron nitride (BN) is a III-V compound and can be synthesized in bulk forms such as cubic boron nitride (c-BN) and layered hexagonal boron nitride (h-BN) as well as 0D fullerennes and 1D boron nitride nanotubes (BNNTs). c-BN is one of the hardest material known and hence it is used extensively in industry. On the other hand, h-BN is used as a lubricant in the industry due to its layered structure and the weak bonds between these layers, analogous to graphite. Additionally, it is worth to note the thermal stability and chemical inertness of h-BN. Moreover, BNNTs are the wide band-gap semiconductors regardless of their radius and chirality therefore they have potential applications in nanotechnology.

Graphene is 2D honeycomb lattice of carbon atoms with bond length of 1.42 Å. It has a planar structure and it can be extracted from graphite. Graphene is a semi-metal or zero band-gap semiconductor. Due to its electronic, magnetic and other properties it takes extreme attention in recent years. Carbon nanotubes are rolled up versions of graphene. They are one dimensional materials showing different band gaps depending on their chirality and radii. Also, mechanical properties of CNTs are very unique. Although, they are very soft in radial direction and can change their shape elastically, they are very stiff in axial direction. Furthermore, they can form 2D or 3D networks such as Y- or T- junctions and kinks.

In this thesis, 2D honeycomb lattices of boron-nitride and graphene, their defect structures and boron-carbon-nitrogen (BCN) ternary systems are investigated in the framework of density functional theory. In second chapter, the theory of DFT and computational methods are briefly discussed. In third chapter, we introduce the defect structures such as point defects and n-fold ring defects of boron nitride. Third chapter covers the calculations and discussion of carbon substitution into BN layer. The phonon density of states of BNC systems are also included. Chapter five is related with graphene and possible defect formations on graphene as well as the calculations of interaction of sulphur with graphene defects. Finally, chapter six summarizes the conclusions.

Chapter 2

Density functional theory and theoretical background

The physical and chemical properties of condensed matter can be exactly determined by solving the many-body Schrödinger equation. The equation consists of potentials of interacting P nuclei and N electrons in three dimensions in total of $3P + 3N$ degrees of freedom as well as spin degrees of freedom. Unfortunately, the exact solutions of many-body Schrödinger equation are limited to few systems even with computational methods. In the general form, the Hamiltonian of such a system is:

$$\begin{aligned} H &= -\sum_{I=1}^{P} \frac{\hbar^2}{2M_I} \nabla_I^2 - \sum_{i=1}^{N} \frac{\hbar^2}{2m} \nabla_i^2 + \frac{e^2}{2} \sum_{I=1}^{P} \sum_{J \neq I}^{P} \frac{Z_I Z_J}{\mid \mathbf{R}_I - \mathbf{R}_J \mid} \\ &\quad + \frac{e^2}{2} \sum_{i=1}^{N} \sum_{j \neq i}^{N} \frac{1}{\mid \mathbf{r}_i - \mathbf{r}_j \mid} - e^2 \sum_{I=1}^{P} \sum_{i=1}^{N} \frac{Z_I}{\mid \mathbf{R}_I - \mathbf{r}_j \mid} \\ &= T_N + T_e + V_{NN}(\mathbf{R}) + V_{ee}(\mathbf{r}) + V_{Ne}(\mathbf{R}, \mathbf{r}). \end{aligned} \tag{2.1}$$

First two terms are the kinetic energy terms of nuclei and electrons, respectively. Remaining terms denote the Coulombic potentials for nucleus-nucleus, nucleus-electron and electron-electron interaction. Then, the following

Schrödinger equation is:

$$\begin{aligned} H\Psi_i(\mathbf{r},\mathbf{R},t) &= E_i\Psi_i(\mathbf{r},\mathbf{R},t) \quad (2.2) \\ \left[T_N + T_e + V_{NN}(\mathbf{R}) + V_{ee}(\mathbf{r}) + V_{Ne}(\mathbf{R},\mathbf{r})\right]\Psi_i(\mathbf{r},\mathbf{R},t) &= E_i\Psi_i(\mathbf{r},\mathbf{R},t). \end{aligned}$$

For most of the systems, exact solution of many-body Schrödinger equation is not an easy task. Difficulty arises mainly due to two reasons:

(1) Schrödinger equation cannot be easily decoupled into a set of independent equations.

(2) Particles that form the system can obey different statistics. Electrons obey the Fermi-Dirac statistics so that the total wave function should be antisymmetric and the nuclei can be fermions, bosons or distinguishable particles.

In order to simplify this complex many-body problem, we should consider some approximations. The first approximation is Born-Oppenheimer Approximation, also known as Adiabatic Approximation.

2.1 Born-Oppenheimer Approximation

Since the time scales of nuclear and electronic motions are different, as the velocity of the nucleus is much slower than the electrons due to large mass difference between electrons and nuclei, the nuclei can be treated as in the same stationary state of the electronic Hamiltonian. Hence, the full wave function can be separable into electronic and nuclear wave functions [1]. The nuclear wave function may vary in time because of the Coulombic interactions but the electronic wave function instantaneously adjusts itself to the nuclear wave function because of the very fast response of electrons to the ionic motion.

According to the approximation the full wave function factorizes as:

$$\Psi_i(\mathbf{r},\mathbf{R},t) = \Theta_m(\mathbf{R},t)\Phi_m(\mathbf{R},\mathbf{r}) \quad (2.3)$$

where $\Theta_m(\mathbf{R},t)$ and $\Phi_m(\mathbf{R},\mathbf{r})$ are nuclear and electronic wave functions, respectively. Then, the decoupled adiabatic Schrödinger equations of electrons and nuclei are:

$$\begin{aligned}\left[T_e + V_{ee}(\mathbf{r}) + V_{Ne}(\mathbf{R},\mathbf{r})\right]\Phi_m(\mathbf{R},\mathbf{r}) &= \epsilon_m(\mathbf{R})\Phi_m(\mathbf{R},\mathbf{r}) \\ \left[T_N + V_{NN}(\mathbf{R})\right]\Theta_m(\mathbf{R},t) &= i\hbar\frac{\partial}{\partial t}\Theta_m(\mathbf{R},t) \end{aligned} \tag{2.4}$$

where m is any electronic eigenstate but it is often taken as ground state in many applications. The Coulombic interaction between electrons and nuclei is still taken into consideration in the electronic Hamiltonian but the nuclear positions enter as parameters. By varying the nuclear positions adiabatically one can form the potential energy surface, then the motion of the nuclei can be solved.

By neglecting the quantum effects on ionic dynamics, the time dependent Schrödinger equation for nuclei can be replaced by classical Newtonian equation of motion as

$$\frac{\partial^2\mathbf{R}_I(t)}{\partial t^2} = -\nabla_I E_0(\mathbf{R}) \tag{2.5}$$

where

$$E_0(\mathbf{R}) = \varepsilon_0(\mathbf{R}) + V_{NN}(\mathbf{R}). \tag{2.6}$$

Then the force $-\nabla_I E_0(\mathbf{R})$ acting on nucleus contains contributions from ion-ion interaction and a term from the gradient of the electronic total energy which is given as the expectation value of derivative of the electronic Hamiltonian in the ground state from Hellmann-Feynman theorem [2, 3, 4, 5].

$$\begin{aligned}\nabla_I\varepsilon(\mathbf{R}) &= \frac{\partial}{\partial\mathbf{R}_I}\langle\Phi_0|H_e(\mathbf{R})|\Phi_0\rangle \\ &= \langle\nabla_I\Phi_0|H_e(\mathbf{R})|\Phi_0\rangle \\ &\quad +\langle\Phi_0|\nabla_I H_e(\mathbf{R})|\Phi_0\rangle \\ &\quad +\langle\Phi_0|H_e(\mathbf{R})|\nabla_I\Phi_0\rangle \qquad (2.7) \\ &= \langle\Phi_0|\nabla_I H_e(\mathbf{R})|\Phi_0\rangle. \qquad (2.8)\end{aligned}$$

First and third terms vanish due to variational property of the ground state.

Now, we are left with solving the electronic Schrödinger equation. But, again this is not an easy task even numerically and further approximations are necessary.

2.2 Hartree and Hartree-Fock Methods

Even though, the complexity of many-body Schrödinger equation reduces with Born-Oppenheimer approximation, the electronic part is still a difficult problem due to complex electron-electron interaction. In late 1920s, two basic particle-independent methods were introduced which are known as Hartree [6] and Hartree-Fock methods [7]. Both approximations define an effective potential for the single electron Hamiltonian. The electron-electron interaction term is not explicitly included in these effective potentials. Both methods neglect the correlation among electrons, but Hartree-Fock method includes the antisymmetric property of the electronic wave function.

In 1928, Hartree proposed a method that electronic wave function can be expressed in terms of single electron wave-functions and each electron is subjected to the effective potential created by other ions and electrons. According to Hartree approximation;

$$\Phi(\mathbf{R},\mathbf{r}) = \Pi_i \varphi(\mathbf{r}_i) \tag{2.9}$$

$$\left(-\frac{\hbar^2}{2m}\nabla^2 + V_{eff}^{(i)}(\mathbf{R},\mathbf{r})\right)\varphi_i(\mathbf{r}) = \varepsilon_i \varphi_i(\mathbf{r}) \tag{2.10}$$

The effective potential is the sum of the potentials of ions at positions $\mathbf{R}$ ($V(\mathbf{R})$) and the potential created by other electrons is taken into account in a mean field way.

$$V_{eff}^{(i)}(\mathbf{R},\mathbf{r}) = V(\mathbf{R}) + \int \frac{\sum_{j\neq i}^{N} \rho_j(\mathbf{r}')}{|\mathbf{r}-\mathbf{r}'|} \tag{2.11}$$

where $\rho_j(\mathbf{r})$ is the charge density;

$$\rho_j(\mathbf{r}) = |\varphi_i(\mathbf{r})|^2 \tag{2.12}$$

The electronic potential in Eq. 2.11 is also called Hartree potential. The

charge density is expressed in terms of electronic eigenstates, thus the Hartree potential, so that the solution of Schrödinger equation in Eq. 2.10 is *self-consistent field* problem which has to be solved iteratively. For this reason, Hartree method is often called self-consistent field (SCF) method. The procedure works as follows. At the first step, the appropriate trial wave function is chosen from which the charge density and the initial effective potential are created. By solving the Schrödinger equation the wave function is re-calculated. The steps are repeated until the self consistency is achieved between the initial and final wave functions.

Then, the total energy of the system can be calculated as:

$$E_H = \sum_{n=1}^{N} \varepsilon_n - \frac{1}{2} \int \int \frac{\rho(\mathbf{r})\rho(\mathbf{r}')}{|\mathbf{r} - \mathbf{r}'|} d\mathbf{r} d\mathbf{r}' \tag{2.13}$$

where $\rho(\mathbf{r})$ is the final electronic charge density, and the second term on right hand side is the Hartree energy which corresponds to the classical electrostatic energy of the charge density $\rho(\mathbf{r})$.

Hartree method can be improved by including the antisymmetric property of the electronic wave function since electrons obey the Fermi statistics. According to the Hartree-Fock method the total wavefunction is written as a determinant of one-particle orbital (called Slater determinant), including both position and spin components. Neglecting the spin-orbit interaction, Slater [8] determinant will be:

$$\Phi = \frac{1}{\sqrt{N!}} \begin{vmatrix} \varphi_1(\mathbf{r}_1, \sigma_1) & \varphi_1(\mathbf{r}_2, \sigma_2) & ... & \varphi_1(\mathbf{r}_N, \sigma_N) \\ \varphi_2(\mathbf{r}_1, \sigma_1) & \varphi_2(\mathbf{r}_2, \sigma_2) & ... & \varphi_2(\mathbf{r}_N, \sigma_N) \\ ... & ... & ... & ... \\ \varphi_N(\mathbf{r}_1, \sigma_1) & \varphi_N(\mathbf{r}_2, \sigma_2) & ... & \varphi_N(\mathbf{r}_N, \sigma_N) \end{vmatrix} \tag{2.14}$$

where $\varphi_i(\mathbf{r}_j, \sigma_j)$ are the single particle spin-orbital. The Hartree-Fock method considers the exchange interaction among electrons which gives additional coupling term in the Schrödinger equation. For the i^{th} electron, the equation will be;

$$\left(-\frac{\hbar^2}{2M_I} \nabla_I^2 + V(\mathbf{R}) + \int \frac{\sum_{\sigma',j=1}^{N} \rho_j(\mathbf{r}', \sigma')}{|\mathbf{r} - \mathbf{r}'|} d\mathbf{r}' \right) \varphi_i(\mathbf{r}, \sigma)$$

$$-\sum_{j=1}^{N}\left(\sum_{\sigma'}\int\frac{\varphi_j^*(\mathbf{r}',\sigma')\varphi_i^*(\mathbf{r}',\sigma')}{|\mathbf{r}-\mathbf{r}'|}d\mathbf{r}'\right)\varphi_j(\mathbf{r},\sigma)=\sum_{j=1}^{N}\lambda_{ij}\varphi_i(\mathbf{r},\sigma) \tag{2.15}$$

where the last term at left hand side is the exchange term. The exchange of electrons with same spin should be spatially separated, thus lowers the coulomb energy of the system. The calculation of electronic properties of a system by Hartree-Fock method is similar to Hartree method by iterative minimization techniques described before. Note that for $i = j$ (self-interaction), the 3^{rd} and 4^{th} terms exactly cancel each other as required. Hartree-Fock method is a sufficient method for calculating the electronic structure of molecules and makes a good approximation for interatomic bonding.

Both methods are simple but have some disadvantages. For few electron systems the methods are effective, but the computation time increases rapidly with increasing number of electrons. For insulators and semiconductors, the methods predict the band gap too large and for molecules HOMO-LUMO gap is overestimated. Moreover, the many-body correlations are neglected in both of the formulation.

2.3 Thomas-Fermi Model

For the first time in 1927, Thomas and Fermi [9, 10, 11] proposed that the electronic density $\rho(r)$ is the central variable and the total energy can be written in terms of electronic density. Actually, the theory is the crude model of modern density functional theory, however it did not include the exchange and correlation effects. The Thomas-Fermi energy functional given as

$$E_{TF}(\rho)=C_k\int\rho(\mathbf{r})^{5/3}d\mathbf{r}+\int\nu(\mathbf{r})\rho(\mathbf{r})d\mathbf{r}+\frac{1}{2}\int\int\frac{\rho(\mathbf{r})\rho(\mathbf{r}')}{|\mathbf{r}-\mathbf{r}'|}d\mathbf{r}d\mathbf{r}' \tag{2.16}$$

where the first term represents the kinetic energy and it can be calculated from the kinetic energy density of non-interacting electrons in homogenous electron gas. Remember that, the Fermi wavevector is related with the electron density as

$$k_F=[3\pi^2\rho(\mathbf{r})]^{1/3} \tag{2.17}$$

Integrating over all filled states up to Fermi wavevector via classical kinetic energy formula yields the Thomas-Fermi kinetic energy.

$$T_{TF} = \frac{3h^2}{10m}\left(\frac{3}{8\pi}\right)^{2/3}\int \rho(\mathbf{r})^{5/3}d\mathbf{r} \tag{2.18}$$

The ground state density that minimize the total energy can be calculated using Lagrange multipliers. Since the total number of electrons is constant, we can introduce a Lagrange multiplier μ;

$$\frac{\delta}{\delta\rho(\mathbf{r})}(E_{tot} - \mu N) = 0 \tag{2.19}$$

$$\frac{5}{3}C_k\rho(\mathbf{r})^{2/3} + \nu(\mathbf{r}) + \frac{1}{2}\int \frac{\rho(\mathbf{r}')}{|\mathbf{r}-\mathbf{r}'|}d\mathbf{r} = \mu \tag{2.20}$$

where μ is the chemical potential.

Although, the Thomas-Fermi theory is precursor to the density functional theory, it is insufficient for calculating the electronic structure so as the total energy. The theory expresses the kinetic energy term in a crude way and quantum effects such that exchange and correlation are totally absent. The theory cannot predict the molecular bonding, for example the total energy of a molecule is higher than its constituent atoms.

2.4 Density Functional Theory

Density functional theory is the main computational method for calculating the electronic and mechanical properties of many-body systems for the last forty years. The key point of the theory is the use electron density functionals (name refers to functions of a function) instead of using many-body wavefunction, for describing properties of the system. In other words, ground state total energy is the unique functional of the electron density. In addition, the perturbation methods are developed in the literature for the description of the excited states. However, the exchange and correlation effects are taken into account within an approximation during the implementation of the DFT.

The total energy of a many-body system can be written as;

$$E = \langle\Phi|\hat{T} + \hat{V} + \hat{V_{ee}}|\Phi\rangle = \langle\Phi|\hat{T}|\Phi\rangle + \langle\Phi|\hat{V}|\Phi\rangle + \langle\Phi|\hat{V_{ee}}|\Phi\rangle \tag{2.21}$$

where the first term is the kinetic energy, second term is the energy due to nuclei (or ions) or external fields and last term denotes the electron-electron energy. The last term can be written as (e=1);

$$V_{ee} = \langle\Phi|\hat{V_{ee}}|\Phi\rangle = \left\langle \Phi \left| \frac{1}{2}\sum_{i=1}^{N}\sum_{j\neq i}^{N}\frac{1}{|\mathbf{r_i} - \mathbf{r_j}|}\right|\right\rangle = \int \frac{\rho_2(\mathbf{r},\mathbf{r}')}{|\mathbf{r}-\mathbf{r}'|}d\mathbf{r}d\mathbf{r}' \tag{2.22}$$

where ρ_2 is two electron density matrix and 1/2 comes from double counting. Two electron density matrix can be written in terms of annihilation and creation operators as

$$\rho_2(\mathbf{r},\mathbf{r}') = \frac{1}{2}\sum_{\sigma,\sigma'}\langle\Phi|a^\dagger_\sigma(\mathbf{r})a^\dagger_{\sigma'}(\mathbf{r}')a_{\sigma'}(\mathbf{r}')a_\sigma(\mathbf{r})|\Phi\rangle. \tag{2.23}$$

where two-body correlation function defined as

$$\rho_2(\mathbf{r},\mathbf{r}') = \frac{1}{2}\rho(\mathbf{r},\mathbf{r})\rho(\mathbf{r}',\mathbf{r}')g(\mathbf{r},\mathbf{r}') \tag{2.24}$$

where $\rho(\mathbf{r},\mathbf{r}')$ is the one-body density matrix.

$$\rho(\mathbf{r},\mathbf{r}') = \sum_\sigma \rho_\sigma(\mathbf{r},\mathbf{r}') \tag{2.25}$$

and

$$\rho_\sigma(\mathbf{r},\mathbf{r}') = \langle\Phi|a^\dagger_\sigma(\mathbf{r})a_\sigma(\mathbf{r}')|\Phi\rangle. \tag{2.26}$$

Therefore, the electron-electron interaction term Eq. 2.22 will be

$$V_{ee} = \frac{1}{2}\int\frac{\rho(\mathbf{r})\rho(\mathbf{r}')}{|\mathbf{r}-\mathbf{r}'|}d\mathbf{r}d\mathbf{r}' + \frac{1}{2}\int\frac{\rho(\mathbf{r})\rho(\mathbf{r}')}{|\mathbf{r}-\mathbf{r}'|}[g(\mathbf{r},\mathbf{r}')-1]d\mathbf{r}d\mathbf{r}'. \tag{2.27}$$

The first term in Eq. 2.27 corresponds to classical electrostatic interaction energy and the second term is the quantum correlation energy among electrons. Since the electrons are fermions, the total wavefunction should be antisymmetric. Therefore, electrons with same spin should be spatially separated and hence the coulomb energy reduces. This energy reduction is called exchange energy and can be taken into calculations via Hartree-Fock method by defining Slater determinant wavefunction as described before. Due to Coulomb interaction, electrons with opposite spin also repel each other. This effect lowers the Coulomb

energy, but increases the kinetic energy of the electrons. The correlation energy is defined as difference between the total energy of the system and its calculated Hartree-Fock energy. The total energy of the system from Eq. 2.21 and Eq. 2.27 will be

$$E = T + V + \int \frac{\rho(\mathbf{r})\rho(\mathbf{r}')}{|\mathbf{r} - \mathbf{r}'|} d\mathbf{r} d\mathbf{r}' + E_{XC}, \tag{2.28}$$

and the kinetic energy and energy due to external field can be expressed as

$$T = \left\langle \Phi | - \frac{\hbar^2}{2m} \sum_{i=1}^{N} \nabla_i^2 | \Phi \right\rangle = -\frac{\hbar^2}{2m} \int [\nabla_r^2 \rho(\mathbf{r}, \mathbf{r}')]_{\mathbf{r}'=\mathbf{r}} d\mathbf{r} \tag{2.29}$$

$$V = \sum_{I=1}^{P} \left\langle \Phi | \sum_{i=1}^{N} \nu(\mathbf{r}_i - \mathbf{R}_I) | \Phi \right\rangle = \sum_{I=1}^{P} \int \rho(r) \nu(\mathbf{r} - \mathbf{R}_I) d\mathbf{r}, \tag{2.30}$$

and the exchange-correlation energy is;

$$E_{XC} = \frac{1}{2} \int \frac{\rho(\mathbf{r})\rho(\mathbf{r}')}{|\mathbf{r} - \mathbf{r}'|} [g(\mathbf{r}, \mathbf{r}') - 1] d\mathbf{r} d\mathbf{r}'. \tag{2.31}$$

2.5 Hohenberg-Kohn Theorem

In 1964, Hohenberg and Kohn [12] proved two fundamental theorems of the density functional Theory. These theorems can be applied to any interacting system in an external potential. While, Hohenberg-Kohn formulation is valid for non-degenerate case, Levy and Lieb made general formulation for degenerate cases [13, 14]. Hohenberg-Kohn theorems are:

Theorem 1: External potential acting on an interacting system is univocally determined by ground state particle density, apart from an additive constant. Since all the terms in Hamiltonian is now described by particle density, ground state energy and wavefunction can be determined in terms of ground state particle density.

Theorem 2: Total energy functional can be written in terms of particle density and the global minimum of this functional with respect to particle density is the total ground state energy.

The proofs of these theorems are rather simple. Let us assume that two different external potentials ν and ν' can be generated by same particle density $\rho(r)$. External potential ν corresponds to H which have ground state energy E_0 and ground state wavefunction ψ. Similarly, external potential ν' corresponds to H' which have ground state energy E_0' and ground state wavefunction ψ'. Since ψ' is not the ground state wavefunction of H, calculating expectation values:

$$\begin{aligned} E_0 < \langle\psi'|H|\psi'\rangle &= \langle\psi'|H'|\psi'\rangle + \langle\psi'|H - H'|\psi'\rangle \\ &= E_0' + \int \rho(\mathbf{r})(\nu(\mathbf{r}) - \nu'(\mathbf{r}))d\mathbf{r}, \end{aligned} \tag{2.32}$$

Similarly,

$$\begin{aligned} E_0' < \langle\psi|H'|\psi\rangle &= \langle\psi|H|\psi\rangle + \langle\psi|H' - H|\psi\rangle \\ &= E_0 - \int \rho(\mathbf{r})(\nu(\mathbf{r}) - \nu'(\mathbf{r}))d\mathbf{r}. \end{aligned} \tag{2.33}$$

Combining Eq. 2.32 and Eq. 2.33 gives $E_0 + E_0' < E_0' + E_0$. So that, the initial assumption is inconsistent and two external potentials should be the same except for an additive constant. Thus, the external potentials are uniquely determined by electron density. The universal total energy functional can be written in terms of arbitrary electron density as;

$$E_\nu[\tilde{\rho}] = F_\nu[\tilde{\rho}] + \int \tilde{\rho}(\mathbf{r})\nu(\mathbf{r})d\mathbf{r} \tag{2.34}$$

where

$$F_\nu[\tilde{\rho}] = \langle\psi[\tilde{\rho}]|T + V|\psi[\tilde{\rho}]\rangle. \tag{2.35}$$

Let us assume that ρ corresponds to ground state electron density, the total energy evaluated for the ground state density is lower than energy calculated for any other density.

$$\begin{aligned} \langle\psi[\tilde{\rho}]|H|\psi[\tilde{\rho}]\rangle &= F_\nu[\tilde{\rho}] + \int \tilde{\rho}(\mathbf{r})\nu(\mathbf{r})d\mathbf{r} \\ &= E_\nu[\tilde{\rho}] \geq E_\nu[\rho] = E_0 = \langle\psi[\rho]|H|\psi[\rho]\rangle \end{aligned} \tag{2.36}$$

Then,

$$\delta\left\{E_\nu[\rho] - \mu\left(\int \rho(\mathbf{r})d\mathbf{r} - N\right)\right\} = 0 \tag{2.37}$$

which gives generalized Thomas-Fermi equation as

$$\mu = \frac{\delta E_\nu[\rho]}{\delta\rho} = \nu(\mathbf{r}) + \frac{\delta F[\rho]}{\delta\rho}. \tag{2.38}$$

2.6 Kohn-Sham Equations

In 1965, Kohn and Sham [15] showed that total energy of an interacting system can be calculated from the non-interacting particle equations. All terms in the single particle total energy can be expressed as a functional of electron density. The Kohn-Sham total energy functional is

$$\begin{aligned} E[\Phi_i] &= 2\sum_i \int \Phi_i \left[-\frac{\hbar^2}{2m}\right] \nabla^2 \Phi_i d\mathbf{r} \\ &+ \int V_{ext}\rho(\mathbf{r})d\mathbf{r} + \frac{e^2}{2}\int \frac{\rho(\mathbf{r})\rho(\mathbf{r}')}{|\mathbf{r}-\mathbf{r}'|} d\mathbf{r}d\mathbf{r}' + E_{XC}[\rho(\mathbf{r})] \end{aligned} \tag{2.39}$$

with

$$\rho(\mathbf{r}) = 2\sum_i |\Phi_i(\mathbf{r})|^2 \tag{2.40}$$

where factor two comes from the spin states. The single particle Kohn-Sham equation is given as

$$\left[-\frac{\hbar^2}{2m} + V_{ext}(\mathbf{r}) + V_H(\mathbf{r}) + V_{XC}(\mathbf{r})\right] \Phi_i(\mathbf{r}) = \epsilon \Phi_i(\mathbf{r}) \tag{2.41}$$

where V_H is the Hartree potential

$$V_H(\mathbf{r}) = e^2 \int \frac{\rho(\mathbf{r}')}{|\mathbf{r}-\mathbf{r}'|} d\mathbf{r}' \tag{2.42}$$

and V_{XC} is the exchange-correlation potential

$$V_{XC}(\mathbf{r}) = \frac{\delta E_{XC}[\rho(\mathbf{r})]}{\delta \rho(\mathbf{r})}. \tag{2.43}$$

The main difference between Kohn-Sham and Hartree-Fock approximations is the exchange-correlation functional which is included within single particle Kohn-Sham equations. Moreover, fundamental variable in Kohn-Sham method is charge density whereas Hartree-Fock method uses the antisymmetrized Slater determinants and minimizes the energy in terms of these functions.

The kinetic energy, classical coulomb energy, and the energy due to external potential are exact functionals, but all quantum many-body interactions are included in exchange-correlation term. Thus, the precision of the approximation

highly depends on the accurate description of exchange-correlation(XC) functional. There are some approximations like local density approximation (LDA) and generalized gradient approximation (GGA) which are derived in order to deal with XC functional. The Kohn-Sham approach works nicely in systems such as insulators, sp-bonded metals, group IV and II-V semiconductors, and molecules with covalent or ionic bonding. The accuracy of the approximation is reduced for strongly correlated systems and the method has some difficulties of calculating van der Waals forces, band gap in semiconductors etc.

Similar to the Hartree and Hartree-Fock methods, the iterative algorithm for Kohn-Sham method works as follow: After creating reasonable charge density, the Kohn-Sham equation can be solved and single particle wave functions can be obtained. Then, Hartree potential and exchange-correlation potentials can be calculated. Afterwards, new charge density is calculated and the procedure is repeated. After enough successive iterations, the ground state electron density and thus minimum of the total energy can be found. The total energy is the sum of single-particle Kohn-Sham eigenvalues but the double counting terms in the Hartree energy and exchange-correlation energy have to be subtracted. In fact, the Kohn-Sham eigenvalues are not, strictly speaking, the energies of the single particle electron states, but rather the derivatives of the total energy with respect to the occupation numbers of these states. Nevertheless, the highest occupied eigenvalue in an atomic or molecular calculation is nearly the unrelaxed ionization energy for that system [16].

2.7 Local Density Approximation

In density functional theory, due to complex nature of exchange-correlation interaction some approximation needs to be made. Local density approximation (LDA) assumes that the exchange-correlation energy density of an electronic system is equal to the exchange-correlation energy density of a homogenous electron gas with same density.

$$\epsilon_{XC} = \epsilon_{XC}^{hom}[\rho(\mathbf{r})]. \tag{2.44}$$

Moreover, the exchange-correlation potential is accepted as purely local. In this limit, the energy can be written as

$$E_{XC}[\rho(\mathbf{r})] = \int \epsilon_{XC}(\mathbf{r})\rho(\mathbf{r})d\mathbf{r} \tag{2.45}$$

and

$$\frac{\delta E_{XC}[\rho(\mathbf{r})]}{\delta \rho \mathbf{r}} = \frac{\partial \epsilon_{XC}(\mathbf{r})\rho(\mathbf{r})}{\partial \rho \mathbf{r}}. \tag{2.46}$$

The local spin density approximation (LSDA) is the generalization of LDA, that is energy density in Eq.2.45 is replaced with the spin averaged energy density which is taken as the energy density of polarized homogeneous electron gas.

The exchange-correlation energy of the homogeneous electron gas is given in analytical form by Ceperley and Alder [17]. The locality of exchange-correlation potential depends on the nearby inhomogeneities in the electron density. The accuracy of LDA depends on how much the charge density system is close to density of homogeneous electron gas. Thus, LDA works best for some solids like nearly-free-electron metal. In such solids, the effects of exchange and correlation is short ranged. The LDA tends to fail for inhomogeneous cases like atoms where the density must go continuously to zero outside the atom [16]. Moreover, in weak molecular bonds, like hydrogen bonding, the binding energy affected by inhomogeneities, thus LDA approach is failed. Similarly, for van der Waals type of bonds the binding is due charge-charge correlations and therefore the interaction is non-local. One of the difficulties related with LDA is self-interaction. In LDA, self-interaction is taken into account by an approximate value and for confined systems like atoms the self-interaction term will be large.

The important features for the LDA are listed below [18]:

1. For homogenous system LDA works better. For systems where large deviations in the electronic density occurs, the LDA tends to fail because the exchange-correlation energy becomes more non-local.

2. LDA gives higher binding energy for molecules and solids.

3. LDA predicts chemical trends, e.g. chemical bonds, well.

4. For covalent, ionic and metallic systems, bond lengths, bond angles and phonon frequencies are well predicted by LDA whereas dielectric properties are overestimated by about an 10 percent error.

5. For weakly bound systems, bond lengths are estimated too short.

2.8 Generalized Gradient Approximation

The gradient expansion of the electronic density, $\rho(\mathbf{r})$, which can be used to represent the exchange-correlation energy, is widely used non-local extension of the LDA. The exchange-correlation energy has gradient expansion as;

$$E_{XC}[\rho(\mathbf{r})] = \int A_{XC}[\rho]\rho(\mathbf{r})^{4/3}d\mathbf{r} + \int C_{XC}[\rho]|\nabla\rho(\mathbf{r})|^2/\rho(\mathbf{r})^{4/3}d\mathbf{r} + ... \qquad (2.47)$$

Thus, the exchange-correlation energy has the form;

$$E_{XC}[\rho(\mathbf{r})] = \int \rho(\mathbf{r})\epsilon_{XC}[\rho(\mathbf{r})]d\mathbf{r} + \int F_{XC}[\rho(\mathbf{r}), \nabla\rho(\mathbf{r})]d\mathbf{r} \qquad (2.48)$$

where F_{XC} is dimensionless and should satisfy the formal conditions such that sum rules, long range decay, etc, otherwise, GGA calculations often leads worse results [18]. There are several exchange-correlations functionals developed by Langreth-Mehl [19], Perdew-Wang '86 [20], Perdew-Wang '91 [21], Becke '88 [22], etc. The important features for the GGA are listed below:

1. Atomic and molecular binding energies are better predicted with GGA.

2. GGA results for the systems containing hydrogen bonds are better than LDA.

3. Bond lengths and angles are improved with GGA.

4. GGA is more realistic approach for magnetic solids.

5. For noble metals, LDA predictions are better than GGA.

6. For semiconductors, except for the binding energies LDA gives better results.

Both GGA and LDA are the approximations and the exact forms for the exchange-correlation term is not yet known. Thus, it is worthy to check which of the approximation works better for the system under consideration. The comparison with the experimental values shows which approach is in good agreement with the real case.

2.9 Computational Details

In the preceding sections, we showed that many-particle Schrödinger equation can be reduced to single-particle Schrödinger equations in terms Kohn-Sham formulation and every component in the equations are the functionals of electronic density $\rho(\mathbf{r})$. Moreover, we examined two different approaches to handle exchange-correlation energy. But, there are very large number of ions and very large number of non-interacting electrons moving in an effective potential in a crystal so that very large number of single-particle Schrödinger equations have to solved. In addition, every wave function extends over the entire crystal so that infinite number of basis set has to be used in computational calculation. To overcome these difficulties, first the Bloch's theorem will be discussed.

2.10 Bloch's Theorem

Bloch's theorem [23] states that each electronic wave function in a periodic potential can be chosen to have the form of a plane wave times a function with the periodicity of the lattice

$$\psi_i(\mathbf{r}) = exp(i\mathbf{k}.\mathbf{r}) f_i(\mathbf{r}). \tag{2.49}$$

The lattice periodic part $f_i(\mathbf{r})$ can be expanded in terms of discrete plane-wave basis set with reciprocal lattice vectors $\mathbf{G}$ such that

$$f_i(\mathbf{r}) = \sum_{\mathbf{G}} c_{i,\mathbf{G}} exp(i\mathbf{G}.\mathbf{r}), \tag{2.50}$$

where $c_{i,\mathbf{G}}$ are the plane wave coefficient and $\mathbf{G}.l = 2\pi m$ with $\mathbf{l}$ is a lattice vector and m is any integer. Eq. 2.49 and Eq. 2.50 gives

$$\psi_i(\mathbf{r}) = \sum_{\mathbf{G}} c_{i,\mathbf{k}+\mathbf{G}} exp[i(\mathbf{k}+\mathbf{G}).\mathbf{r}]. \tag{2.51}$$

2.11 Plane-wave basis sets

In order to solve Kohn-Sham equations (Eq. 2.39), we should expand the wave function at each k vector in terms of some basis set (for example if the basis set is the atomic orbital the method is called Linear Combination of Atomic Orbital (LCAO) or tight binding). Plane wave basis sets are very convenient and simple way of expressing the wavefunctions of a periodic system. Plane wave basis sets are different from the localized sets such that they do not depend the nuclear positions. Moreover, same plane wave basis set can be applied to different atomic species. Combining Bloch theorem (Eq. 2.51) with Kohn-Sham equations (Eq. 2.39) gives

$$\begin{aligned} \sum_{G'}[\frac{\hbar^2}{2m}|\mathbf{k}+\mathbf{G}|^2\delta_{\mathbf{G}\mathbf{G}'} &+ V_H(\mathbf{G}-\mathbf{G}') + V_{ion}(\mathbf{G}-\mathbf{G}') \\ &+ V_{XC}(\mathbf{G}-\mathbf{G}')]c_{i,\mathbf{k}+\mathbf{G}'} = \varepsilon_i c_{i,\mathbf{k}+\mathbf{G}}, \end{aligned} \tag{2.52}$$

where V_{ion}, V_H and V_{XC} are the Fourier transforms of the ion-ion, Hartree and exchange-correlation potentials. The derivation of total energy in the momentum space is performed by Ihm et al. [24] and given as

$$\begin{aligned} E_{total} = \sum_i \varepsilon_i &- \frac{1}{2}\Omega\left[\sum_{\mathbf{G}} V_H(\mathbf{G})\rho(\mathbf{G}) + \frac{1}{4}\sum_{\mathbf{G}} \mu_{xc}(\mathbf{G})\rho(\mathbf{G})\right] \\ &+ \frac{1}{2}\sum_{\mu,\nu\neq\mu} \frac{Z^2}{|\mathbf{R}_\mu - \mathbf{R}_\nu|}, \end{aligned} \tag{2.53}$$

where Ω is the volume and μ_{xc} is

$$E_{XC}(\mathbf{r}) = \int \mu_{xc}(\mathbf{r}) d\rho(\mathbf{r}). \tag{2.54}$$

Equation 2.52 is a matrix equation in which the kinetic energy is diagonal and the solution can be obtained by diagonalization. In principle, infinite number of plane

waves should be used the expand the wavefunctions, therefore the matrix equation in Eq. 2.52 contains infinite terms, however plane waves with high kinetic energy do not contribute significantly to the total energy. Hence, by choosing appropriate cutoff energy (E_{cutoff}), plane wave basis set can be truncated at some point. Energy cutoff depends on the atomic species in the system and on which pseudopotentials are used in order to describe these atoms. Before starting calculations on a system, energy cutoff test should be performed and appropriate energy cutoff value that satisfies convergence criteria should be used.

For the non-periodic systems, such as defected systems or isolated molecules, plane wave formalism can also be applied. The periodic boundary conditions are still valid, however interactions between molecules or defect-defect interactions might become negligible by choosing a large enough supercell. The size of the supercell depends on the system, for instance for isolated systems, the distance between nearest atoms of neighbor cell should be about 10 Å.

2.12 Pseudopotentials

Since the Coulomb potential is inversely proportional with position ($\mathbf{r}$), valence electrons move in a strong ionic potential in the core region so that the wave functions of the valence electrons oscillate rapidly at core region. The wavefunctions of core electrons and valence electrons should be orthogonal and orthogonality is maintained by these oscillations. In order to expand these high oscillatory valance wavefunctions in the core region, very large number of plane wave basis set should be used. The same is correct for tightly bound core electrons. The pseudopotential theory (for theoretical approach see Kaxiras [25]) is used to expand the valance electrons wave functions at the core regions with small number of plane-wave basis set [16].

Many of the electronical properties of solids depends on the valance electrons rather than core electrons. Moreover, in different chemical environments the core electron wave functions do not differ too much. Pseudopotential approximation

removes the core electrons and consider the crystal as ions and valence electrons. It also replaces the strong ionic potential with weaker pseudopotential that acts on a set of pseudo wave functions rather than true wave functions. Figure 2.1 shows the schematic illustration of real and pseusopotentials, and corresponding wave functions.

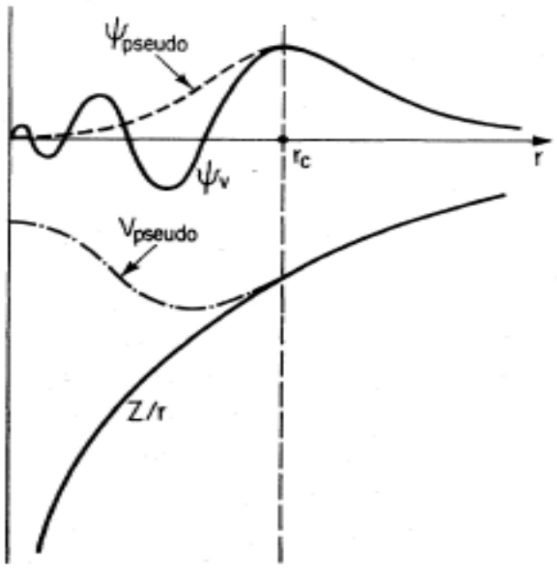

Figure 2.1: Schematic presentation of real (solid) and pseudo wavefunctions (dashed) of the valance electrons in the core region. Reproduced from Ref. [16].

2.13 k-point Sampling

In principle, the Brillouin zone (BZ) integrations should be performed for infinite number of k vectors in the first BZ. However, for the close k vectors, the wave-functions are almost identical and the finite number of k-point mesh is enable to map the first BZ. Furthermore, the point group symmetry of the lattice allows to reduce the k-point mesh. After utilizing the group symmetry, there will be finite number of k-points within the irreducible part of the BZ, which have certain weights.

The calculation time, accuracy and memory requirements are highly depend on the chosen k-point mesh in DFT calculations. Dense meshes allow more accurate calculations but increase the calculation time and memory usage. Therefore, k-point test should be performed (i.e. to attain energy convergence criterion) before full DFT calculations.

In the literature, different kinds of methods are developed to create special sets of k points in the Brillouin zone (Chadi and Cohen [26]; Joannopoulos and Cohen [27]; Monkhorst and Pack [28]; Evarestov and Smirnov [29]). A Monkhorst-Pack grid is a uniform distribution of k-points in the first BZ. For insulators and semiconductors, few number of k-points are required but for metallic systems denser k point mesh should be used to obtain desired convergence.

Chapter 3

Defects on boron-nitride nanostructures

3.1 Introduction

Boron nitride (BN) can assume several different crystal structures [30]; like sp^2-bonded hexagonal BN (h-BN), rhombohedral BN (r-BN), sp^3 bonded cubic BN (c-BN) and wurtzite BN (w-BN). It can also be synthesized in nanotube (BNNT) [31] and fullerene [32, 33] structures. BN structures are wide band-gap semiconductors and isoelectronic of carbon structures and other III-V compounds like GaAs. Band-gap of cubic phase is 6.4 eV and hexagonal phase is 5.2 eV [34, 35]. BN structures can be doped both p-type and n-type [36, 37].

As first synthesized by Wentorf [38], c-BN has a sphalerite crystal structure, same as zinc-blende structure. The hardness of c-BN has been found to be 70 GPa, which makes c-BN one of the hardest materials [34]. Cubic BN exhibits high thermal stability and chemical inertness. Similarly, c-BN is chemically inactive for metals like iron, nickel and their alloys. Moreover, it has high thermal conductivity, high melting temperature, wide band gap as well as low dielectric constant. Because of all these properties, c-BN is extensively used in industrial applications. The bulk synthesis of c-BN can be performed by using high pressure

and temperature technique from hexagonal polymorph [39] similar to production of synthetic diamond from graphite. At low pressures nucleation of c-BN thin films can be achieved by various methods [40] involving bombardment of growing films by high energy ions required for the nucleation of the cubic phase. The nucleation of the cubic phase in the c-BN films is a subject of many studies, and there are several models on this. One of the models proposed is nanoarch method [41] which suggests that nucleation of cubic phase occurs on top of h-BN layer, triggered by transient structures called arches.

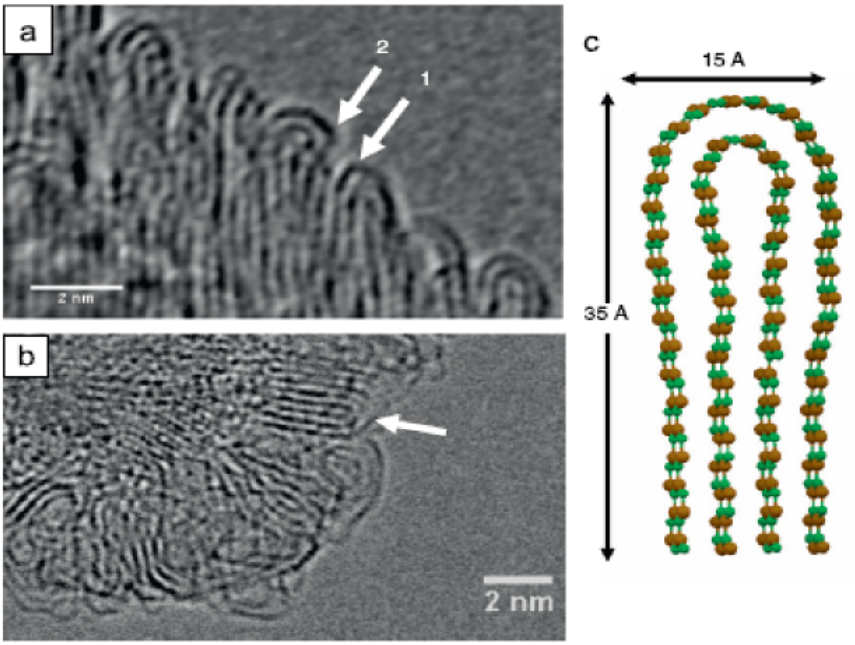

Figure 3.1: (a) and (b) Hexagonal nanoarches are observed during c-BN nucleation. Arrows indicate the defect formation on these nanoarches. (c) Final geometry of an atomic simulation of a two-layer nanoarch. Reproduced from Reference [41].

Eventhough, c-BN is thermodynamically stable boron nitride polymorph at ambient conditions and room temperature [42], the h-BN is the most commonly used form of boron nitride and it is a candidate material for many advanced technological applications. This is possible because of the considerable activation barrier for the direct solid-state transformation of h-BN into c-BN [42]. Hexagonal BN has multi-layer honeycomb lattice similar to graphite but with partly ionic layer-layer interaction. The localization of π electrons around nitrogen atoms makes h-BN a wide band-gap semiconductor [43].

Boron nitride nanotubes are first synthesized by Chopra *et. el.* [31] and they exhibit unique properties. Carbon nanotubes can be metallic or semiconductor depending on diameter or chirality, but BN nanotubes are wide band-gap semiconductors independent of tube chirality and morphology with band-gap of 4.5-5.5 eV [44].

Cubic BN nucleation takes place on hexagonal boron nitride layers growing perpendicular to the substrate surface during thin film synthesis. Nucleation and growth of the cubic phase has also drawn significant interest due to its complexity and unusual structure. Studies focused on the nucleation of the cubic phase suggest the possibility that transient phases and/or defects on these h-BN structures have a role in sp3 bonded cubic phase nucleation. In this study, we have investigated the nature, energetics, and structure of several possible defects on BN basal planes, including point defects, 4-, and 5-fold BN rings, that may possibly match the experimentally observed transient phase fine structure. DFT calculations are used to relax these structures while minimizing their respective total energies. Data from DFT calculations and analysis of simulated images from the proposed atomic structures suggest that 4-fold BN rings are more likely to exist on the transient phase possibly leading to c-BN nucleation.

3.2 Computational Methods

For the investigation of defects on h-BN nano-structures, we have performed the first-principles plane-wave calculations [16] within density functional theory (DFT) [12, 15] by the projector-augmented-wave (PAW) potentials [45, 46] using Vienna ab-initio simulation package (VASP) program [47, 48, 49]. The exchange-correlation potential was expressed in terms of the generalized gradient approximation (GGA) (Perdew-Wang 91 type [50]). To achieve the desired accuracy, a plane-wave cutoff energy of 500 eV was used in all calculations. A BN large supercell with 10 Angstroms of vacuum is introduced to minimize the ion-ion interaction in the non-periodic directions. Therefore, only the Γ point is used as

Monkhorst-Pack [28] mesh in order to model the k-point sampling in the Brillouin zone. The partial occupancy around the Fermi level is treated by Gaussian smearing with a smearing parameter of 0.08 eV. For all calculations energy was converged to within 10^{-5} eV accuracy. In all calculations, edges of finite sized structures are saturated by H atoms and then all of the atoms are relaxed to their minimum energy configurations by using conjugate gradient method where total energy and atomic forces are minimized. Maximum force magnitude remained on each atom is set at most to 0.06 eV/Å.

3.3 Results and Discussion

Cross-sectional TEM studies on the c-BN thin films indicated that the c-BN phase always formed above an h-BN layer where the basal planes of h-BN grow perpendicular to the substrate surface. The nanoarch model suggests arches (i.e. curved structures) to be a transient structure on the h-BN layer triggered by intense ballistic displacements due to bombardment of the growing h-BN film [51]. However, observed atomic configurations of nanoarches are likely to be different than semi-circular arrangement. Figure 3.1 shows TEM micrograph of growing h-BN film and a basic atomic model of a 2-layer nanoarch [41]. The sharp corners on Figure 3.1(a) indicate the defect formation on h-BN layer. The bending angles are given as 102° and 104°, corresponding to labeled defects in Fig. 3.1, respectively.

There have been a number of theoretical studies of the energetics of zero-dimensional defects (i.e. vacancies, anti-site defects) for BN monolayers [53], while direct observation of such atomic level defects has been limited for BN nano-structures [52, 54]. In this study, we have investigated the energetic stability and structural properties of various proposed defects on boron nitride monolayer cluster. The stability of various candidate defective structures with respect to each other was investigated in N-rich and B-rich mediums. The candidate defects are boron and nitrogen vacancies (V_B and V_N), double vacancy (V_{BN}) boron antisite (N_B) i.e. the presence of a nitrogen atom of a boron one, nitrogen

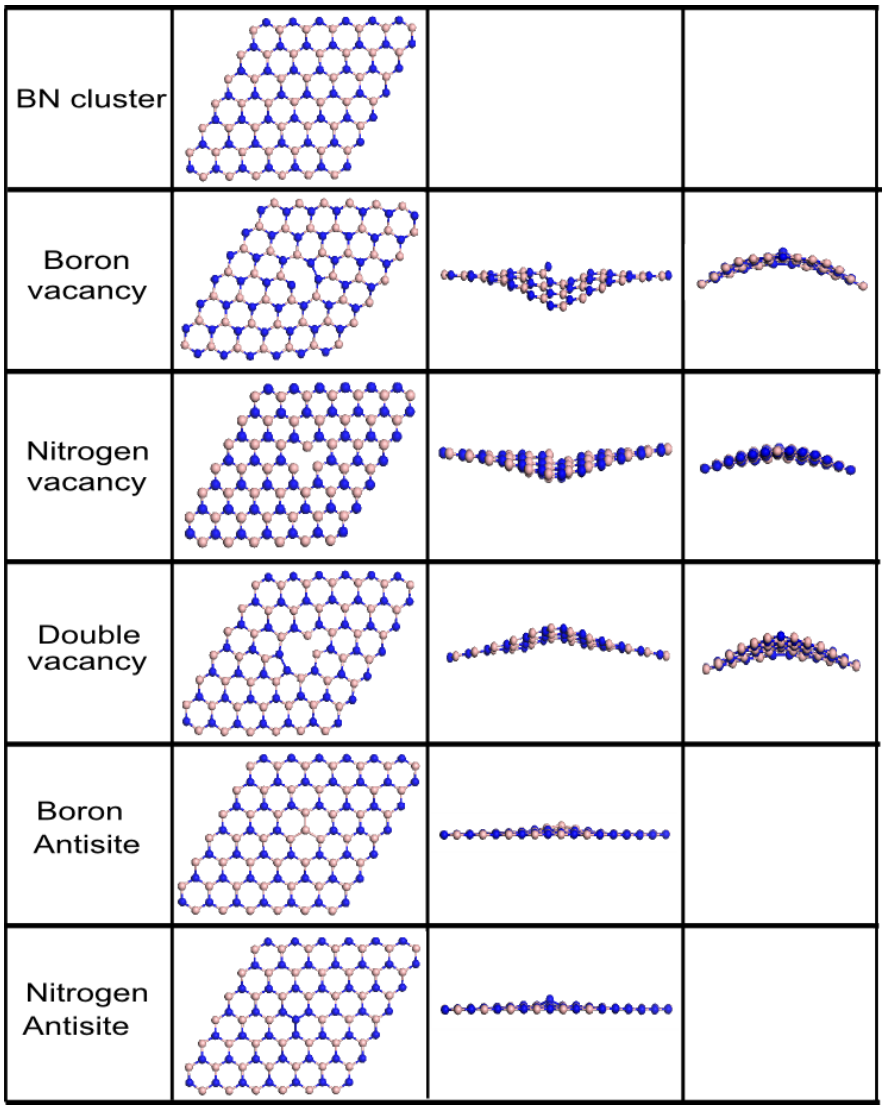

Figure 3.2: Optimized geometries of various point defects including single and double vacancies and antisites on BN monolayer. While, top views are shown on second column, side views are presented on third and fourth columns.

antisite (B_N), 4-fold ring, 5-fold boron pair and nitrogen pair. Figure 3.2 shows the final geometries of BN pristine and point defect structures on h-BN. Both top views and side views are shown in the figure. Boron and nitrogen vacancies make pentagonal rings (B-B pair or N-N pair), while for the double vacancy, we have observed a 8-fold ring and a pentagonal ring. These vacancy structures exhibits both positive and/or negative curvatures along different directions, but the corresponding bending angles in these structures do not match with the measured angles from the observed structures in the experiment [41]. Anti-site defects stays almost planar, only deformation is at the defect region.

Figure 3.3 shows the final geometries of 5-fold boron and nitrogen pair as well as 4-fold and 8-fold ring formations. 4-fold and 5-fold defects make positive curvature and the bending angles are measured as 102° for 4-fold ring and 5-fold nitrogen pair along pair direction. These angles match with the observed defect formation which is labeled with '1' in Fig. 3.1. For detailed analysis, we have calculated the formation energies of these structures for the N-rich and B-rich environments.

Formation energy of a BN structure is defined as;

$$E_{form} = E_{tot} - n_N\mu_N - n_B\mu_B - n_H\mu_H, \tag{3.1}$$

where n's are the number of atoms and μ's are the chemical potentials of each atom. Formation energies can be defined in nitrogen rich and boron rich environments by imposing the following constraint:

$$\mu_N + \mu_B = \mu_{BN}^{layer}. \tag{3.2}$$

Under this constraint, the formation energies in N-rich and B-rich environments will be

$$E_{form}^{N-rich} = E_{tot} - n_N\mu_N - n_B(\mu_{BN}^{layer} - \mu_N) - n_H\mu_H, \tag{3.3}$$

$$E_{form}^{B-rich} = E_{tot} - n_N(\mu_{BN}^{layer} - \mu_B) - n_B\mu_B - n_H\mu_H. \tag{3.4}$$

The chemical potentials of constituent atoms are calculated from the gas phase for nitrogen and hydrogen and from metallic alpha phase for boron. These are summarized in Table 3.1.

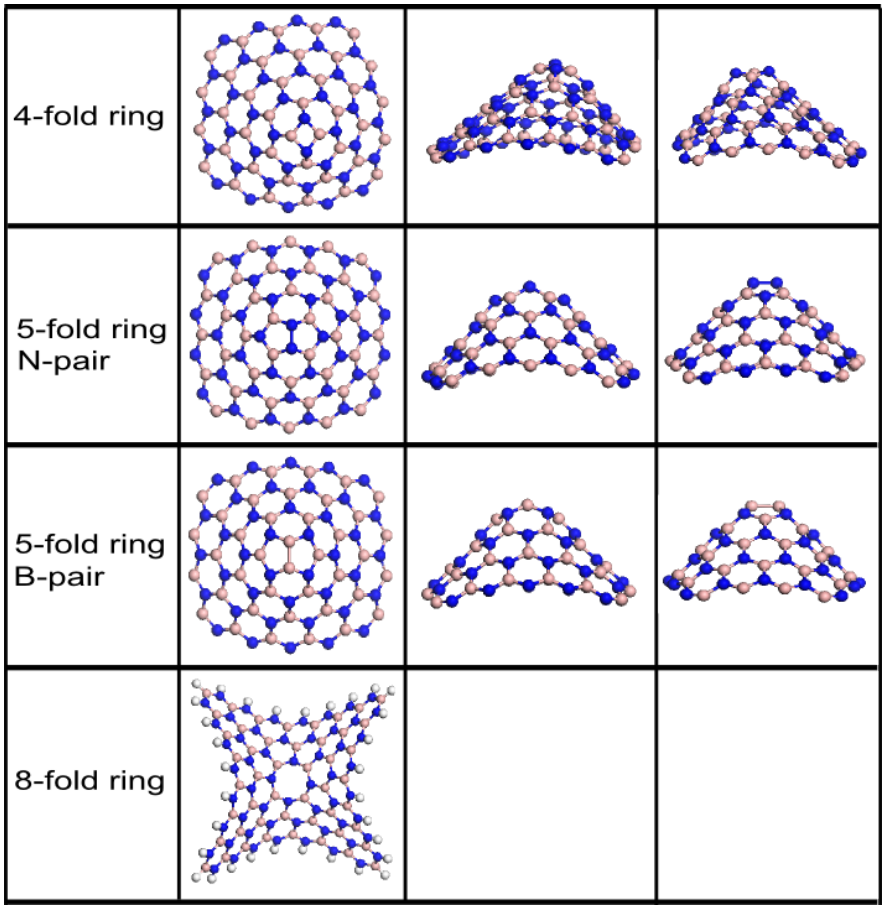

Figure 3.3: Top (second column) and side (third and fourth columns) views of optimized geometries of 4-fold, 5-fold (N-pair and B-Pair) and 8-fold ring formations on BN monolayer. Side views show that 4-fold and 5-fold rings make positive curvature whereas 8-fold ring formation exhibits both positive and negative curvatures along different directions as seen from its top view.

Structure	E_{tot}	N_A/cell	Chem. Pot.	a	c	Bond length
α-boron	-80.22	12	-6.68	2.83	4.18	-
α-N_2 (GGA)	-66.91	8	-8.36	6.21		-
α-N_2 (LDA)	-70.49	8	-8.81	5.23		1.0990
N_2 (gas)	-16.67	2	-8.33			1.1097
H_2 (gas)	-6.80	2	-3.40			0.7491
BN	-35.33	4	-17.67	2.51	3.57	-
BN monolayer	-17.68	2	-17.67	2.51		-
Graphite	-36.93	4	-9.23	2.47	3.69	-
Graphene	-18.48	2	-9.24	2.47		-

Table 3.1: Chemical potential of various elements used in the formation energy calculations. All energies are in eV and all lengths are in Å.

The formation energies calculated using this formulation in N-rich and B-rich mediums for various defects structures under consideration are shown in Table 3.2. Corresponding numbers of atoms in each of the structure are also included in this table. Since the number of the atoms for each species are equal for 4-fold ring and 5-fold pairs, we denote the total energy of 4-fold ring as reference to others. As clearly seen from the Table 3.2, the 4-fold ring is energetically more stable than other structures. Similar argument holds in N-rich and B-rich synthesis environments. The vacancy defects have slightly higher formation energies than other defects in both mediums. For N-rich case, the minimum formation energy occur for the nitrogen antisite and similarly boron antisite defect formation seems to be the most favorable defect structure. From Table 3.2, it is seen that the formation energies are closely related with the number of atoms. For instance, there is an excess number of nitrogen atoms in N-antisite case, therefore the chance of formation of this defect in nitrogen rich environment is higher. Although, antisite defects are the most reasonable defects in synthesis environments, structural analysis shows that 4-fold ring is the best candidate for describing the defect formations during c-BN thin film synthesis.

It is possible to extent the discussion of relative stabilities of different defect

Defect Type	Number of Atoms (N B H)	E_{rel} (eV)	E_{form}^{N-rich}/n_B (eV)	E_{form}^{B-rich}/n_N (eV)
4-fold ring	24 24 14	-0-	0.391	0.391
5-fold boron pair	24 24 14	0.6	0.416	0.416
5-fold nitrogen pair	24 24 14	1.18	0.440	0.440
N vacancy	23 24 18		0.502	0.408
B vacancy	24 23 18		0.482	0.573
NB vacancy	23 23 18		0.487	0.487
B antisite	23 25 18		0.563	0.381
N antisite	25 23 18		0.367	0.550
8-fold ring	24 20 20			0.406
4-fold ring	40 40 18	-0-	0.282	0.282
5-fold boron pair	40 40 18	0.55	0.295	0.295
5-fold nitrogen pair	40 40 18	1.16	0.311	0.311
5-fold nitrogen pair	60 60 22		0.236	0.236
N vacancy	47 48 26		0.302	0.252
B vacancy	48 47 26		0.297	0.346
NB vacancy	47 47 26		0.305	0.305
B antisite	47 49 26		0.334	0.236
N antisite	49 47 26		0.229	0.328
8-fold ring	56 48 32			0.286

Table 3.2: Formation energies of defect structures on BN monolayer at N-rich and B-rich environments. Third column indicates the relative energy with respect to 4-fold ring defect. Table contains two sets of data corresponding to same defect but within a larger BN structure, so the numbers of atoms are different.

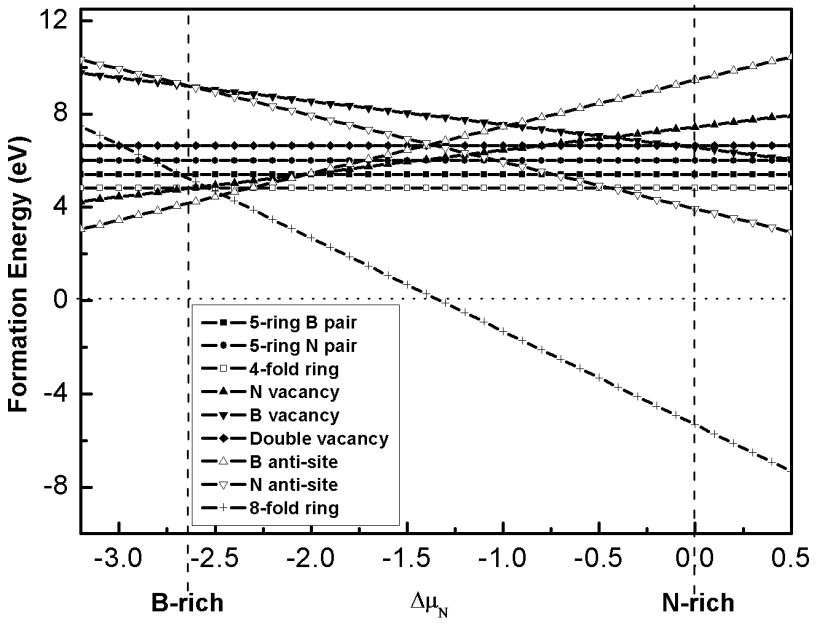

Figure 3.4: Formation energies of defect structures on BN monolayer as a function nitrogen chemical potential. Defect structures imposed on smaller BN structure.

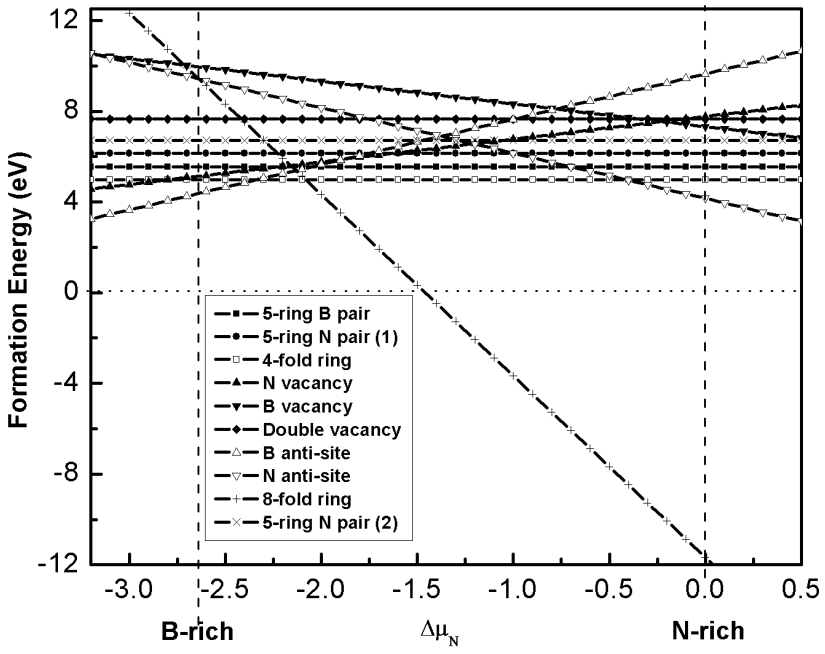

Figure 3.5: Formation energies of defect structures on BN monolayer as a function nitrogen chemical potential. Defect structures imposed on larger BN structure.

structures under different experimental environments starting from the free energy and by incorporating the appropriate chemical potentials for each of the atom. Since the stoichiometry is not same for all the configurations for defect structures considered here, the relative formation energies should be described in terms of the chemical potential of the excess atomic species as:

$$E_{form} = E_{tot} - E_{tot}^{ref} - n_N\mu_N - n_B\mu_B - n_H\mu_H, \tag{3.5}$$

where E_{tot} is the total energy of the system under consideration while E_{tot}^{ref} is the total energy of the reference system, in this case we considered h-BN monolayer as the reference. n's are the number of the excess atoms with respect to the reference system. Let's assume that all the defect structures are in equilibrium with the bulk BN, then we have

$$\mu_N + \mu_B \approx \mu_{BN}^{layer}. \tag{3.6}$$

In principle, the chemical potential of individual species might take any value in gas phase depending on the environmental conditions, however, there are some limits on the allowable range in equilibrium with all possible phases. For example, the chemical potential of each element cannot be larger than the one of bulk elemental phase, since as the μ increases the gas phase condenses to the bulk phase. Therefore, we have

$$\mu_N \leq \mu_N(bulk) \tag{3.7}$$

for nitrogen. $\mu_N(bulk)$ is modeled by the total energy of α-N_2 which is the ground state of bulk nitrogen. Similarly,

$$\mu_B \leq \mu_B(bulk) \tag{3.8}$$

for boron with approximating $\mu_B(bulk)$ by the total energy of α-boron. Furthermore, the heat of formation is

$$H_f = E_N(bulk) + E_B(bulk) - E_{BN}(bulk) \tag{3.9}$$

which is calculated as 2.64 eV. Combining these will lead following lower and upper limits for the chemical potentials:

$$\mu_N(bulk) - H_f \leq \mu_N \leq \mu_N(bulk) \tag{3.10}$$

for nitrogen, and

$$\mu_B(bulk) - H_f \leq \mu_B \leq \mu_B(bulk) \tag{3.11}$$

for boron. Putting all these together, the formation energy can be calculated as:

$$\begin{aligned} E_{form} = \quad & E_{tot}(N_B, N_N) - E_{tot}^{ref}(N_B^0, N_N^0) - n_H\mu_H \\ - \quad & n_B\mu_{BN} - \mu_N(bulk)(n_N - n_B) - \Delta\mu_N(n_N - n_B) \end{aligned} \tag{3.12}$$

as a function of nitrogen chemical potential, and as

$$\begin{aligned} E_{form} = \quad & E_{tot}(N_B, N_N) - E_{tot}^{ref}(N_B^0, N_N^0) - n_H\mu_H \\ - \quad & n_N\mu_{BN} - \mu_B(bulk)(n_B - n_N) - \Delta\mu_B(n_B - n_N) \end{aligned} \tag{3.13}$$

as a function of boron chemical potential. Here, N_N and N_B are the number of nitrogen and boron atoms in defected structure respectively, while N_N^0 and N_B^0 are the ones in the reference system. Hence, $n_N = N_N - N_N^0$ and $n_B = N_B - N_B^0$ are the excess atom numbers. $\Delta\mu_N = \mu_N - \mu_N(bulk)$ and $\Delta\mu_B = \mu_B - \mu_B(bulk)$ are the chemical potentials for nitrogen and boron measured from bulk energy respectively.

The calculated formation energies by using the outlined thermodynamical analysis of considered defect structures on BN monolayer as a function of nitrogen chemical potential is presented in Fig. 3.4 and Fig. 3.5 for smaller and larger BN structure, respectively. Essentially, both of the systems, small and large, show similar behavior for the formation energy of defected structures as a function of chemical potential, there are only small differences in detail, hence one can say that the possible size effects are small. At extreme conditions, i.e. N-rich and B-rich environments, the relative stabilities of different BN defected structures are same as the one reported in Table 3.2. When one examined the rest of the phase diagram, it is clear that the *8-fold ring* defect structure exhibits the largest slope line with negative formation energies when approaching N-rich environments. However, we have to note two points about this system. First of all, this is the system with largest unpaired B and N number as well as largest $(n_N - n_B)$ within the considered structures. Second of all, this structure has the most different N_N and N_B compared to the reference system. Because of these facts, let's put the *8-fold ring* defect structure aside by noting that it might be a metastable

structure. Then, both Fig. 3.4 and 3.5 show that while N anti-site defect structure around N-rich environment has the lowest formation energy, B anti-site structure is the energetically most favorable defect structure around B-rich environment. Between these, 4-fold ring defect structure is the one with least defect energy. More precisely, we can describe transition of defect phases in terms of chemical potential as:

B anti-site	$\mu_N \leq \mu_N(bulk) - 2.4$ eV
4-fold ring	$\mu_N(bulk) - 2.4$ eV $\leq \mu_N \leq \mu_N(bulk) - 0.4$ eV
N anti-site	$\mu_N(bulk) - 0.4$ eV $\leq \mu_N \leq \mu_N(bulk)$

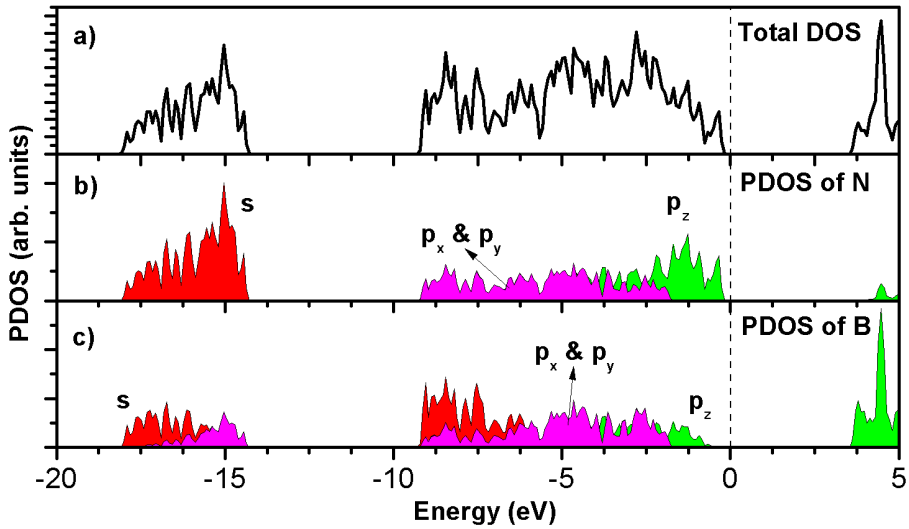

Figure 3.6: Density of states of h-BN monolayer. a) is total DOS, b) is the PDOS on nitrogen atom and c) is the PDOS of boron atom. Projection over different orbital are shown by different colors, s is red, p_x and p_y is violet and p_z is green. The zero of the energy is set to the Fermi energy, E_f, shown by vertical dashed line.

In order to investigate the effect of these defect structures on the bonding and the electronic structure, total density of states (DOS) as well as partial density of states (PDOS) projected on specific atoms and orbital and charge densities of all optimized defect structures are presented in the following figures, and these are compared with the DOS of BN pristine. In all DOS figures, energy axis is shifted so the fermi level, E_f, is set to zero in order to make an immediate

comparison of different systems. Let's start the discussion of electronic structure with the BN pristine. Total DOS as well as PDOS on nitrogen and boron atoms of BN pristine is presented in Fig. 3.6. As seen from Fig. 3.6a, BN is *wide* band gap semiconductor, the valance band and the conduction band is separated by a band gap, E_g, of $\sim$3.62 eV compared to calculated band gap of h-BN monolayer as 4.09 eV, and the experimental value of band gap of h-BN, 5.2 eV. This is a well known shortcoming of DFT, underestimation of E_g. There is another band between -15 eV to -18 eV due to s orbital of N atoms with some contribution from s and $p_x\&p_y$ orbital B atoms. The valance band has mainly $p_x\&p_y$ character coming from both N and B atoms, and at the bottom of valance band there is some B-s contribution. The edges of both valance and conduction bands have p_z character both from N and B atoms, but edge of valance band is mostly from N while the conduction band edge is from B.

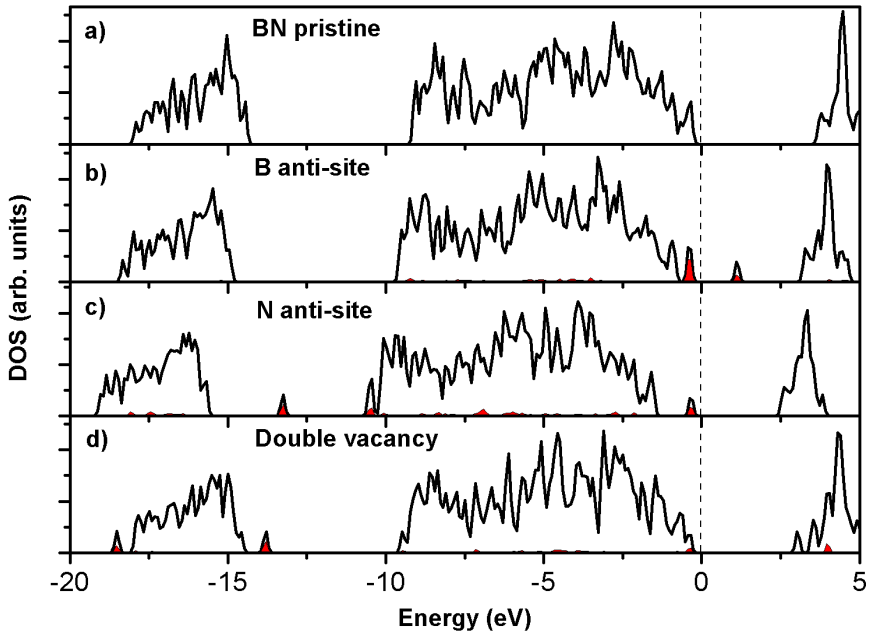

Figure 3.7: Density of states of BN pristine, anti-sites and double vacancy defect structures on BN monolayer. PDOS projected only on the atom of defect are presented by red filled curves. Fermi energy shown by dotted line is shifted to the zero of energy.

Density of states of BN pristine, B anti-site, N anti-site and double vacancy defect structures on BN monolayer are presented in Fig. 3.7. Basically, main features of the BN pristine DOS, so the basic electronic structure, are preserved

in the DOS of the defect structures of 2D BN pristine studied here. However, some states appeared within the band gaps as well as some resonances due to the introduced defects. For example, in the DOS of B anti-site structure, there are two additional peaks, one at top of valance band at the fermi level, and the other is almost at the mid band gap. For N anti-site structure, E_f is pinned by the band gap state due to the additional N atom, so the whole band structure is shifted downwards in energy with respect to the E_f. In this case, there is another peak in lower energy band gap region and at the bottom of valance band because of additional N atom. However, in double vacancy defect structure, major band gap region is clear because of the reconstruction of defect structure and states due to the defect appears in lower energies.

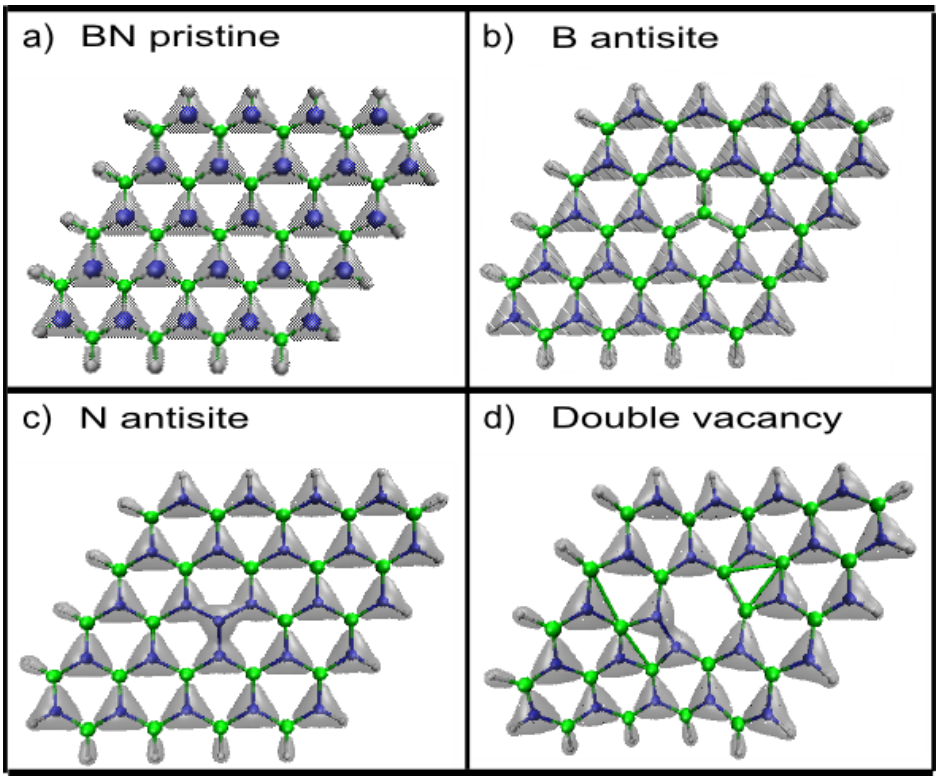

Figure 3.8: Total charge density isosurfaces of BN pristine as well as B and N anti-sites and double vacancy defect structures. Charges are congregate at nitrogen sites.

The total charge densities of BN pristine, B anti-site and N anti-site as well as double vacancy defect structures on BN monolayer are displayed in Fig. 3.8. The total charge density distribution of BN pristine is very uniform showing an accumulation of the charge over nitrogen atoms. Naturally, this is expected since

the N being a group V element has two more electrons compared to group III element B. Because of the dangling bonds, the edges of BN cluster are saturated by hydrogen atoms. This is also apparent from the charge density plot as sticking out isosurfaces towards the H atoms. Inspection of Fig. 3.8 indicates that the identification of B anti-site structure from its total charge density distribution plot is very easy: while the charge density distribution around N atom displays a triangular shape where the corners at the neighboring B atoms and N atom is located at the center of it in such a way that all three sp^2 bonds are covered uniformly, the charge density around the additional B atom elongates along the B-N bonds so makes a three tipped star shape. However, for the N anti-site case, when B atom is replaced by a N atom, the excess charge of additional N atom with a mentioned triangular shaped charge density distribution is appeared around that N atom, so the corners of this triangular charge distribution as roughly at the mid-point of N-N bonds. These general trends are usually observed within the all 2D BN nanostructures studied here. As explained before, the double vacancy structure, formed by removing one B and one N atom, is relaxed to 5-8-5 structure. On this structure, while one of the pentagons involves a N-N bond the other pentagon has a B-B bond. The examination of the charge density plot shown in Fig. 3.8d exhibits two triangular shaped charge density distribution each centered at one of these N atoms of N-N bond, however, nothing is observed around the B-B bond which can be explained by slightly larger B-B bond distance, 1.74 Å.

Eventhough, n-fold ring, namely 4-fold ring, 5-fold ring with B pair or N pair and 8-fold ring, defect structures are highly curved structures, basics features of DOS and charge density distribution are very similar to the picture described above. DOS of these defect structures are presented in Fig. 3.9 and the charge density distribution plots are displayed in Fig. 3.10.

Since the single vacancy defect structures are spin polarized, before discussing the properties of them, we have revisited the BN pristine structure and have examined it in detail in terms of spin polarization. The DOS and the charge density distribution of BN pristine structure without passivating the dangling bonds of the edge atoms with hydrogen atoms are presented in Fig. 3.11 and

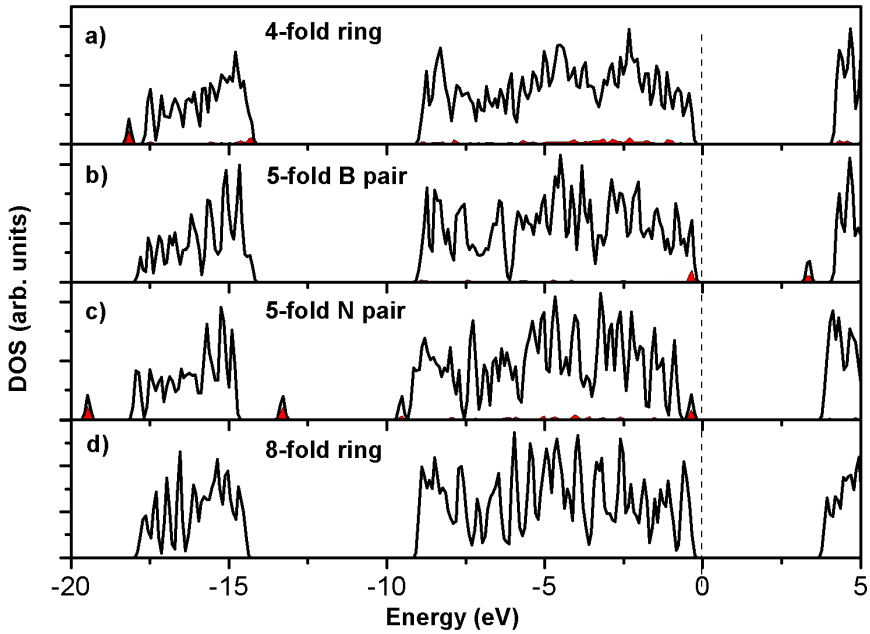

Figure 3.9: Density of states of n-fold defect structures on BN monolayer. The zero of energy is set to the Fermi energy, E_f, shown by vertical dotted line.

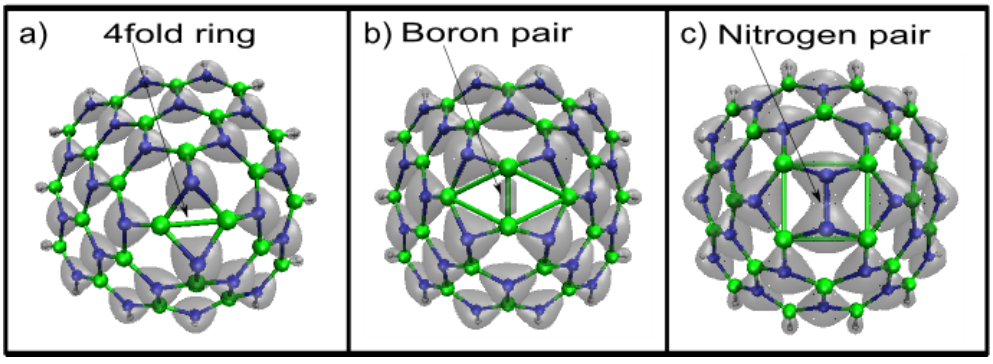

Figure 3.10: Total charge density distribution of 4-fold ring and 5-fold with B pair or N pair defect formations. The N-pair and B-pair are indicated in the figure.

Fig. 3.12, respectively. First of all, this structure is spin polarized and exhibits a half-metallic behavior. While it has semiconductor character with band gap for majority spins, it is a metal for the other spin component. Comparing this DOS with the one shown in Fig. 3.6, there are some additional bands that narrowing or closing the band gaps of BN pristine structure. The nature of these bands are evident from the projected DOS over edge N atoms and edge B atoms as shown in Fig. 3.11. These edge states are also apparent from the plot of difference of spin up and spin down charge densities displayed in Fig. 3.12.

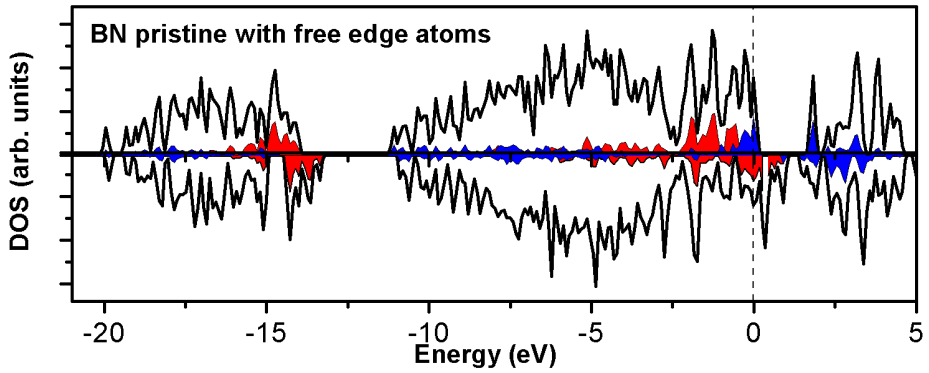

Figure 3.11: Spin density of states of relaxed BN pristine. The dangling bonds are not passivated with hydrogens. Upper panel shows the spin up DOS while the lower panel displays spin down DOS. The sum of the projected DOS over edge N atoms are shown by blue curves while over the edge B atoms by red curves. The fermi level is set to zero of the energy. The structure exhibits a half-metallic behavior.

In order to further test the nature of edge states, difference of spin up and spin down charge densities of BN pristine with various different hydrogen decorations of edge atoms are displayed in Fig. 3.13. The hydrogen decoration includes the passivation of different combinations of the edge atoms like only edge N atoms, only edge B atoms, both N and B edge atoms. The inspection of Fig. 3.13 shows that lack of H atom leads to the spin polarized edge state, and calculated magnetic moments are in accordance with number of passivating H atoms.

Finally, The DOS and the charge density distribution of B vacancy and N vacancy structures are presented in Fig. 3.14 and Fig. 3.15, respectively. All the basic features are along the same line that we discussed for the other defect structures. In summary, these vacancy structures are spin polarized which arises from

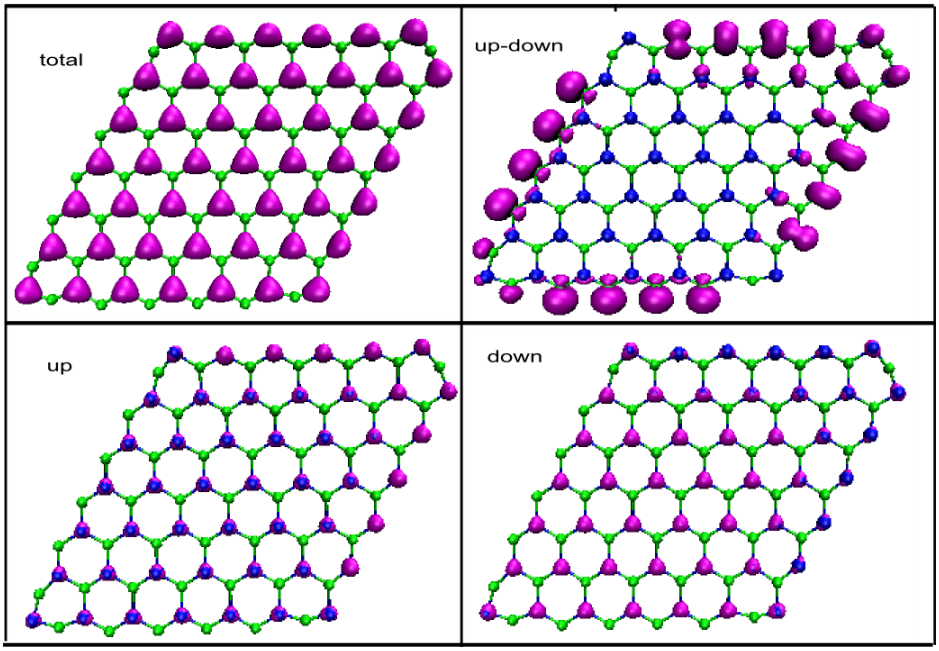

Figure 3.12: a) Total electron density of relaxed BN pristine without passivating the dangling bonds of the edge atoms by hydrogen. b) Difference of spin densities, c) spin up and d) spin down charge densities.

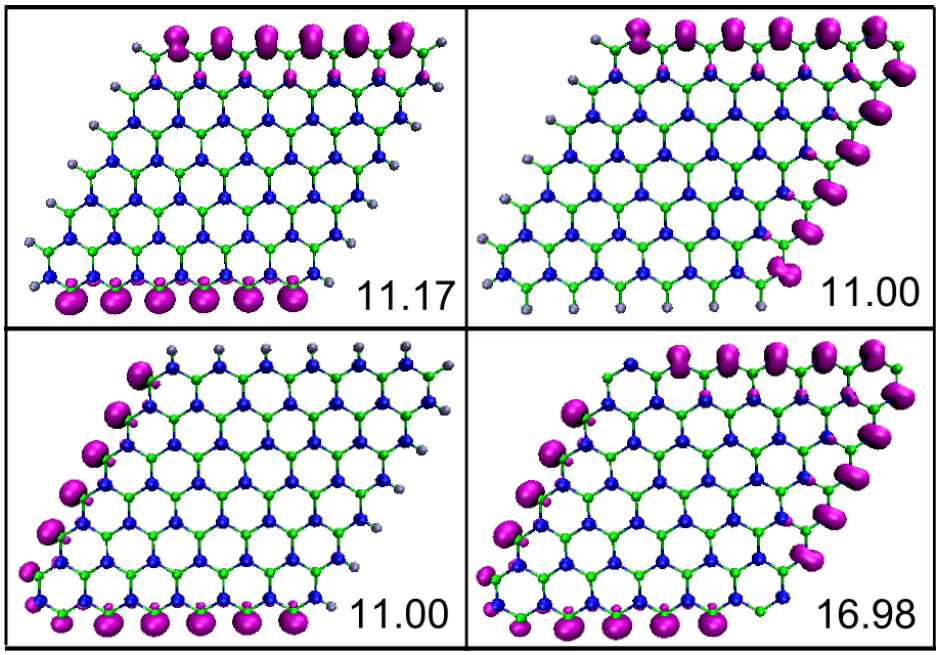

Figure 3.13: Difference spin density isosurfaces of BN cluster with different hydrogen decorations of edge atoms. Indicated numbers are the magnetic moments of the structures.

the unpaired atom in the vacancy region, hence these structures have magnetic moment of 1 μ_B.

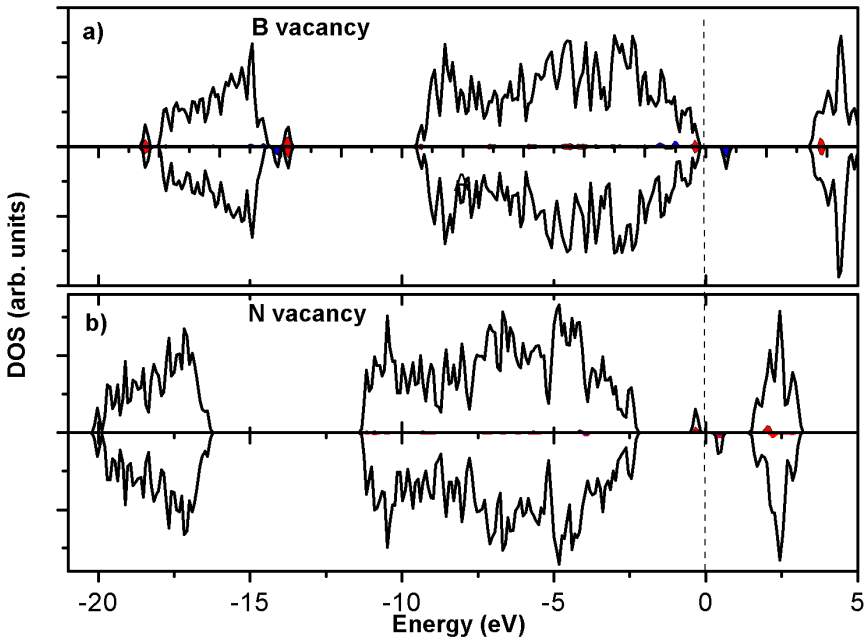

Figure 3.14: Spin density of states of boron and nitrogen vacancies. Upper panels show the majority spin states (spin-up) while lower panels show minority spin states (spin-down). The projected DOS over the atoms around the vacancy are shown by filled curves. The fermi level is set to zero of the energy.

Eventually, we tried a couple of models for the description of nano-arch structures. These are summarized in Fig. 3.16 while the energetics is presented in Table 3.3.

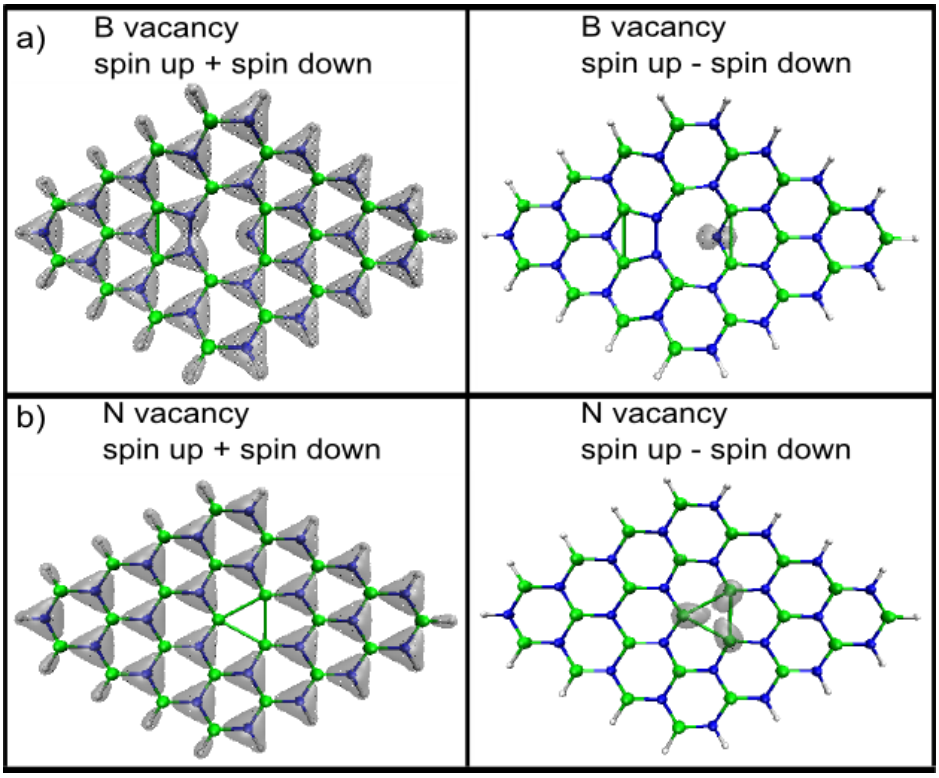

Figure 3.15: Total charge densities and difference of spin up and spin down charge densities of boron and nitrogen vacancies, respectively. These structures have magnetic moment of 1 μ_B.

Structure	Number of Atoms (N B H)	Defect energy (eV)	$E_{form}^{B(N)-rich}/n_N$ (eV)
BN small	24 24 4	4.38	0.183
1 layer zigzag	36 36 4	4.78	0.133
2 layer zigzag	80 80 8	9.72	0.122
1 layer armchair	64 64 4	3.65	0.057
2 layer armchair	136 136 8	8.34	0.061

Table 3.3: Defect energies of simulated BN nanoarch structures.

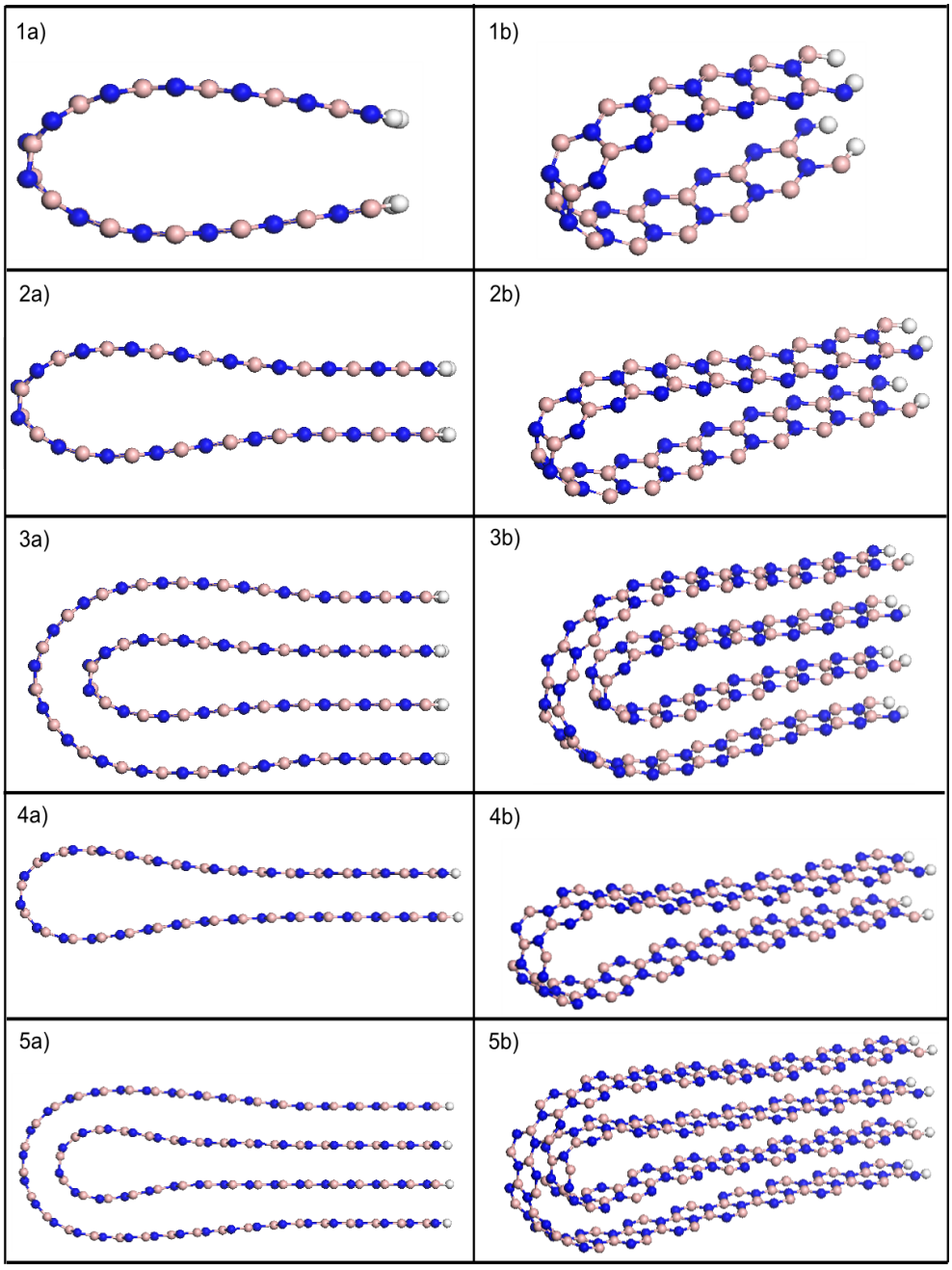

Figure 3.16: Simulated nanoarch structures. All structures are periodic along the direction perpendicular to the page. (1), (2) and (3) have zigzag orientation along the nanoarch direction whereas (4) and (5) have armchair orientation. The dangling bonds at the end are hydrogenated and the atoms are fixed except (1). The inter layer distance is 3.3 Å.

Chapter 4

Geometrical and electronic structure of B-C-N thin films

Materials composed of boron, carbon and nitrogen atoms, which can be termed as "BCN solids" have received significant attention due to their unique mechanical and electronic properties [55, 56]. Ternary phase diagram of B-C-N is an active area for researchers with the idea of synthesizing and designing new materials with unique properties. Combining the properties of pure carbon (diamond and graphite) and BN (h-BN and c-BN) solids into one structure and enabling fine tuning of the materials properties by controlling the chemistry has been the main motivation. For example, hardness of c-BC_2N solid is expected to be in the range defined by c-BN and diamond [57]. On the other hand, BCN solids assuming an hexagonal phase (h-BC_2N) is suggested to be a variable band gap semiconductor and also, expected to display intercalation behavior [55, 58]. Recently, several applications has been suggested for these fascinating materials: according to Kawaguchi *et al* [58] hexagonal BCN solids can be used as an intercalation material for Li-ion batteries, Umeda *et al* [59] and Watanabe *et al* [60] stated possible application of h-BCN films with low dielectric constant (< 2.0) as a passivation layer for high speed electronic devices.

In fact, tribological, chemical, and electronic properties of BCN thin films

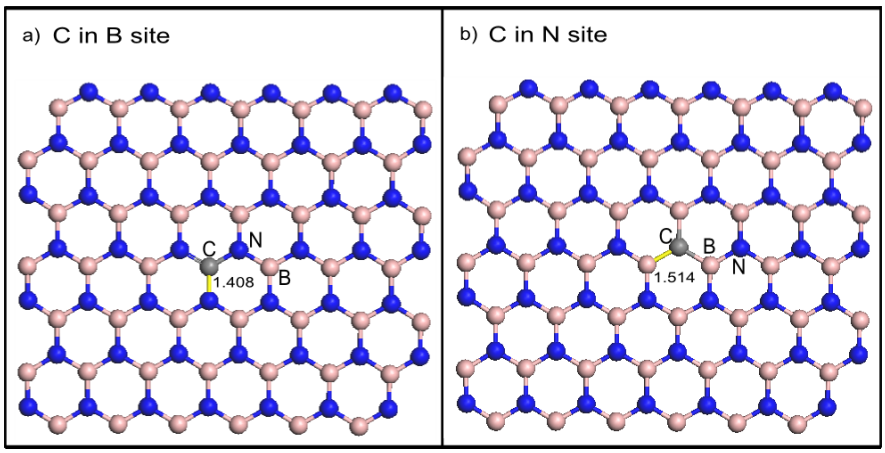

Figure 4.1: Single carbon atom substitution on a) B site and B) N site. The bond lengths are indicated in the figure. We performed calculations by starting planar and non-planar geometries. The planar final geometry is energetically most favorable.

have been studied the most. Furthermore, theoretical and experimental studies on BCN nanotubes and fullerenes exist, as well. One of the challenges regarding BCN films is the difficulty of synthesizing a real ternary compound where all constituent atoms are bonded to each other rather than a binary phase mixture. Thin films of BCN have been deposited by a variety of techniques, such as magnetron sputtering, ion-beam assisted deposition, and chemical vapor deposition. The bonding structure in BCN films has been heavily investigated using x-ray photoelectron spectroscopy (XPS) and Fourier transform-infrared spectroscopy (FTIR). However, interpretation of XPS and FTIR spectra for the identification of ternary phases or segregated phases in BCN films is not straightforward due to the convoluted nature of the resulting spectra in both cases. In some studies, electron energy loss spectroscopy (EELS) and x-ray absorption near edge spectroscopy (XANES) have been applied for ternary phase identification in BCN films through detailed examination of bonding structure and coordination.

However, there is little work in literature that investigates the energetics and atomic level mechanisms responsible for the phase segregation observed for BCN films. In this study, research on the bonding structure of BCN films, energetics of hybridization and phase segregation has been examined with the help of first-principles DFT calculations, which is also used as a tool for the better interpretation of FTIR spectra from deposited films.

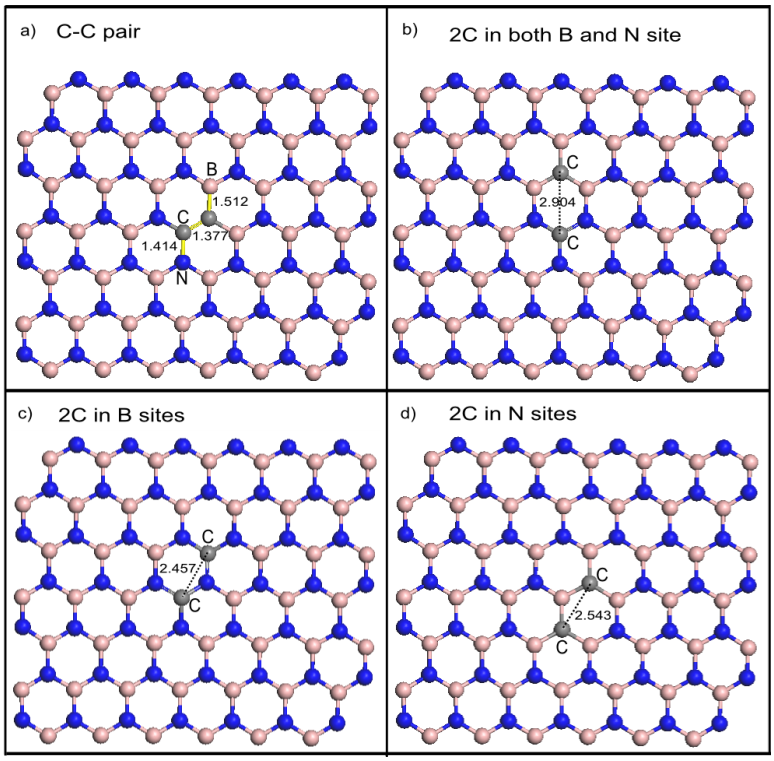

Figure 4.2: Double carbon substitution into BN layer. a) carbon atoms make C-C pair b) B and N are replaced with carbons with distance 2.904 Å c) two boron atoms are replaced with carbons d) two nitrogen atoms are replaced with carbons. The defect energies are given in table 4.2. The C-C pair has the lowest defect energy (4.68 eV).

4.1 Computational Methods

For the investigation of defects on h-BN nano-structures, we have performed the first-principles plane-wave calculations [16] within density functional theory (DFT) [12, 15] by the projector-augmented-wave (PAW) potentials [45, 46] using Vienna ab-initio simulation package (VASP) program [47, 48, 49]. The exchange-correlation potential was expressed in terms of the generalized gradient approximation (GGA) (Perdew-Wang 91 type [50]). To achieve the desired accuracy, a plane-wave cutoff energy of 500 eV was used in all calculations. A BN large supercell with 10 Angstroms of vacuum is introduced to minimize the ion-ion interaction in the non-periodic directions. Therefore, only the Γ point is used as Monkhorst-Pack [28] mesh in order to model the k-point sampling in the Brillouin zone. The partial occupancy around the Fermi level is treated by Gaussian smearing with a smearing parameter of 0.08 eV. For all calculations energy was converged to within 10^{-5} eV accuracy. In all calculations, edges of finite sized structures are saturated by H atoms and then all of the atoms are relaxed to their minimum energy configurations by using conjugate gradient method where total energy and atomic forces are minimized. Maximum force magnitude remained on each atom is set at most to 0.06 eV/$\mathring{A}$.

4.2 Results and Discussion

In this chapter, we will investigate the carbon impurities in boron nitride monolayer. Total energy calculations were performed for various structures, especially the carbon substitution, using density functional theory. We compare the structures in terms of defect energy which is defined as

$$E_{def}[BN-C] = E_{tot}[BN-C] - E_{tot}[BN] - n_C\mu_C + n_B\mu_B + n_N\mu_N \qquad (4.1)$$

where $E_{tot}[BN-C]$ is the total energy of BN-C structure, $E_{tot}[BN]$ is the total energy of planar BN structure without carbon impurity and μ_C, μ_B and μ_N are the chemical potentials of carbon, boron and nitrogen. The total chemical

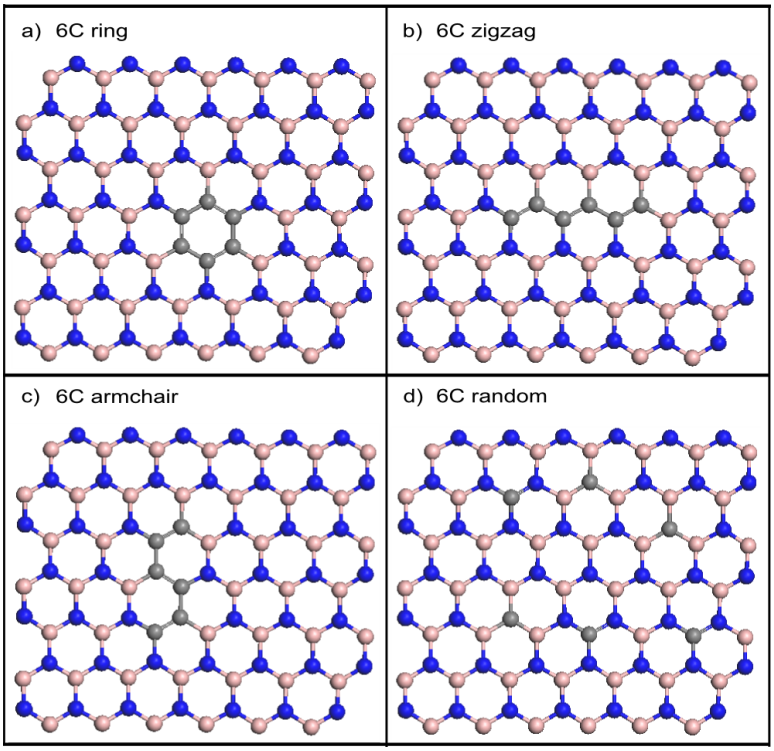

Figure 4.3: Six carbon absorbtion of BN layer such as a) carbon atoms make complete hexagonal ring, b) carbon atoms make zigzag structure, c) carbon atoms make armchair structure and d) carbons are randomly distributed. Defect energies are given in table 4.3. The structures are non-magnetic for 6C case.

Structure	Number of C-C bonds	Number of C-B bonds	Number of C-N bonds	Magnetic mom. μ	E_{def} (eV)
C in B site	0	0	3	1.0	4.38
C in N site	0	3	0	1.0	4.27

Table 4.1: Defect energies and magnetic moments for single carbon substitution into BN layer. The structures are shown in Fig. 4.1. The defect energies are calculated using Eq. 4.1. According to the data carbon atom prefers nitrogen site.

potential of substituted carbon atoms was subtracted and total chemical potentials of missing boron and nitrogen atoms were added in Eq. 4.1. In order to calculate the chemical potentials we used alpha-boron phase for boron, graphite phase for carbon and gas phase for nitrogen. The results are tabulated in Tables 4.1, 4.2 and 4.3. Also, we extent the discussion of defect energies by using the thermodynamical analysis presented on previous chapter, and we have calculated formation energies of carbon substitutions as a function of N chemical potential, and have presented these in Fig. 4.4.

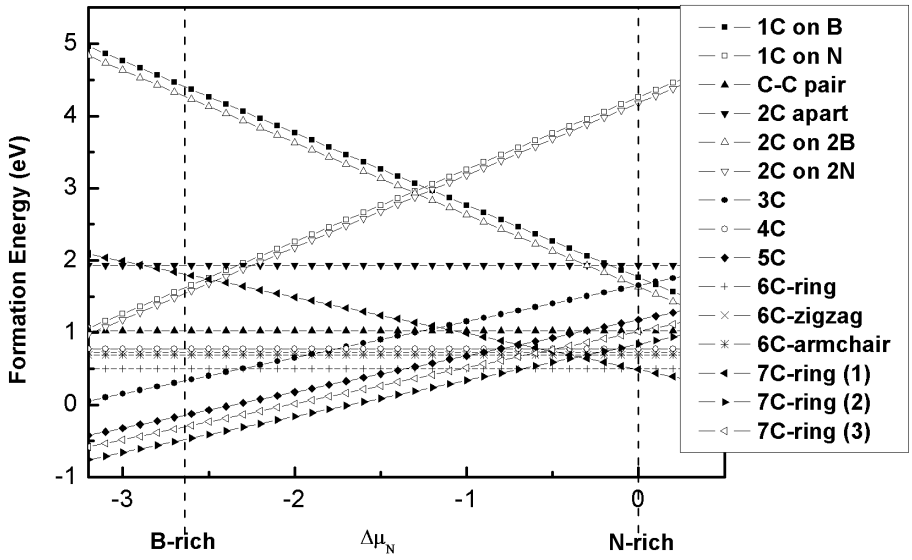

Figure 4.4: Formation energies of carbon substitution structures on BN monolayer as a function nitrogen chemical potential.

For single carbon substitution the foreign carbon atom is placed on boron site and nitrogen site, respectively as in Fig. 4.1. The defect energies are 4.27 eV and

4.38 eV for N site and B site, which suggest that carbon atom initially prefers the position of nitrogen.

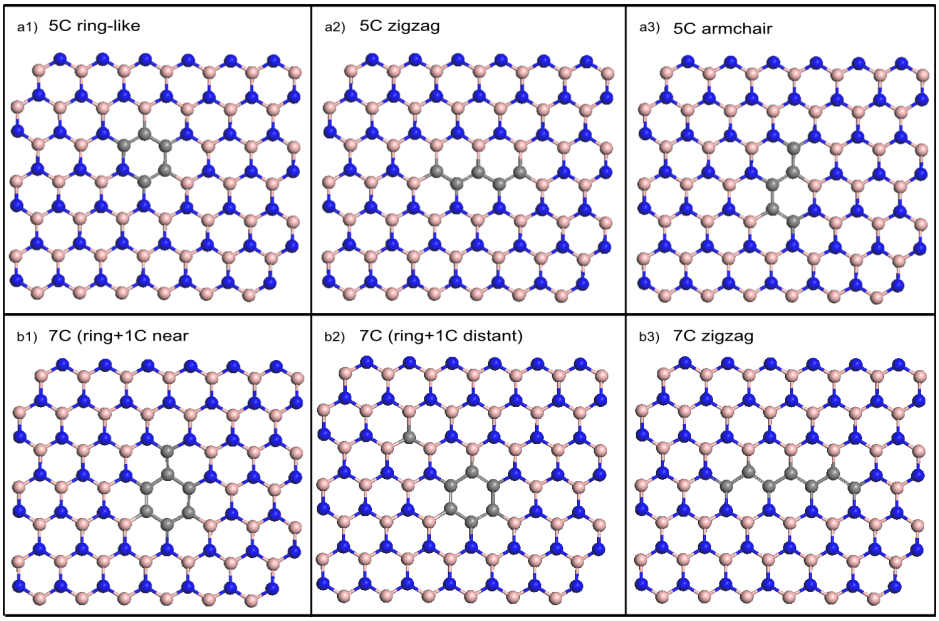

Figure 4.5: Five and seven carbon substitution into BN layer. a1 shows incomplete C ring, a2 and a3 are 5C zigzag and armchair formations, b1 shows hexagonal ring and a carbon in its neighborhood, b2 shows ring structure and a carbon apart, b3 is the 7C zigzag formation.

We tabulate the results for double carbon substitution in Table 4.2. First two lines represents the substitutions for both N and B sites in which the previous one makes C-C pair but at the latter one the C-C distance is 2.904 Å. For the C-C pair case the defect energy is 4.68 eV which shows that this structure is energetically favorable than others. Thus carbon atoms tend to congregate in BN monolayer. Last two lines of Table 4.2 refers to structures for carbon substitution in boron sites or nitrogen sites. We repeated same calculations for various C-C distances and the defect energies are around 8.4-8.5 eV. This result is in good agreement with the one carbon substitution case that the defect energies will be approximately doubled. Thus the structures behave like two separate defects. Figure 4.2 shows the structures for these cases.

For 5, 6 and 7 carbon cases we performed calculations for ring-shape, zigzag, armchair and randomly distributed structures. The results are tabulated at Table 4.4. The carbon aggregation results are more clear by these data. The defect

Structure	Number of C-C bonds	Number of C-B bonds	Number of C-N bonds	Magnetic mom. μ	E_{def} (eV)
C-C pair	1	2	2	~ 0	4.68
C-C apart	0	3	3	~ 0	6.49
2C in 2B sites	0	0	6	~ 0	8.49
2C in 2N sites	0	6	0	~ 0	8.39

Table 4.2: Defect energies for double carbon substitution into BN layer. Magnetic moments and number of bonds are indicated. The structures are shown in Fig. 4.2. The C-C pair case is the lowest defect energy therefore carbons tends to congregate in BN layer.

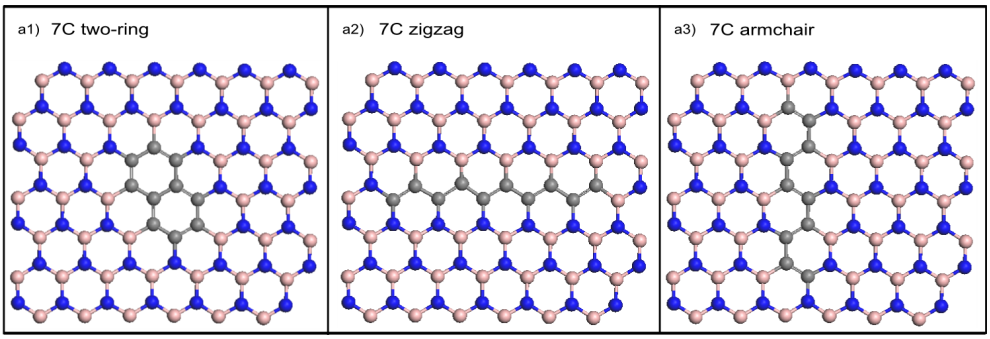

Figure 4.6: The two-ring, zigzag and armchair formations of 10 carbon atoms in BN layer.

Structure	Number of C-C bonds	Number of C-B bonds	Number of C-N bonds	Magnetic mom. μ	E_{def} (eV)
3C	2	4	1	1.0	7.60
3C	1	2	5	1.0	8.88
3C	0	9	0	1.0	12.47
4C	3	3	3	~ 0	8.34
4C	2	4	4	~ 0	9.31

Table 4.3: Defect energies for 3 and 4 carbon substitution into BN layer. When the carbon number is odd the magnetic moment will be 1.0 bohr magneton. For increasing number of C-C bonds the defect energies will be reduced.

Structure	Number of C-C bonds	Number of C-B bonds	Number of C-N bonds	Magnetic mom. μ	E_{def} (eV)
5C ring-like	4	5	2	1.0	11.16
5C along zigzag	4	2	5	1.0	11.43
5C along armchair	4	2	5	1.0	11.16
6C ring	6	3	3	~ 0	10.86
6C along zigzag	5	4	4	~ 0	12.25
6C along armchair	5	4	4	~ 0	12.03
6C all apart	0	9	9	~ 0	19.34
7C ring	7	5	2	1.0	13.78
7C ring + 1C apart	6	6	3	1.0	15.01
7C chain	6	6	3	1.0	14.82

Table 4.4: 5, 6 and 7 carbon substitution into BN layer. The structures are shown in Fig. 4.3 and 4.5. For 5C case the number of C-C bonds are equal and hence the defect energies are similar. The ring structure of 6C is the most energetic one and the defect energy is even lower than 5C defect energies due to hexagonal symmetry.

Structure	Number of C-C bonds	Number of C-B bonds	Number of C-N bonds	Magnetic mom. μ	E_{def} (eV)
10C two ring	11	4	4	0	17.23
10C zigzag	9	6	6	~ 0	19.72
10C armchair	9	6	6	0	19.11

Table 4.5: Data for the two-ring, zigzag and armchair formations of 10 carbon atoms in BN layer. We demonstrate the structures at Fig. 4.6.

energy reduces with the increasing number of C-C bonds that is carbon atoms prefer sites which increases the C-C bond. For instance, for 6 carbon case the complete hexagonal ring of C atoms make 6 C-C pairs and defect energy is the lower then other 6 carbon structures. Furthermore, defect energy of 6 carbon ring 0.36 eV lower than the defect energy of incomplete 5 carbon ring which suggest that the sixth atom completes the hexagonal symmetry. Comparison with chain structures and ring structures shows the similar result that complete ring is energetically favorable by 1.2-1.4 eV. Random distributions of C atoms in BN monolayer have always higher defect energy.

We figured out the charge density differences of single carbon substitution in Fig. 4.11. The reference structure is the BN layer. The charges are congregate on nitrogen sites in the reference structure. Boron, carbon and nitrogen have 3, 4 and 5 valance electrons, respectively. For carbon substitution into boron site the excess charge remains on carbon.

Furthermore we made calculations for carbon adsorption on BN layer. The

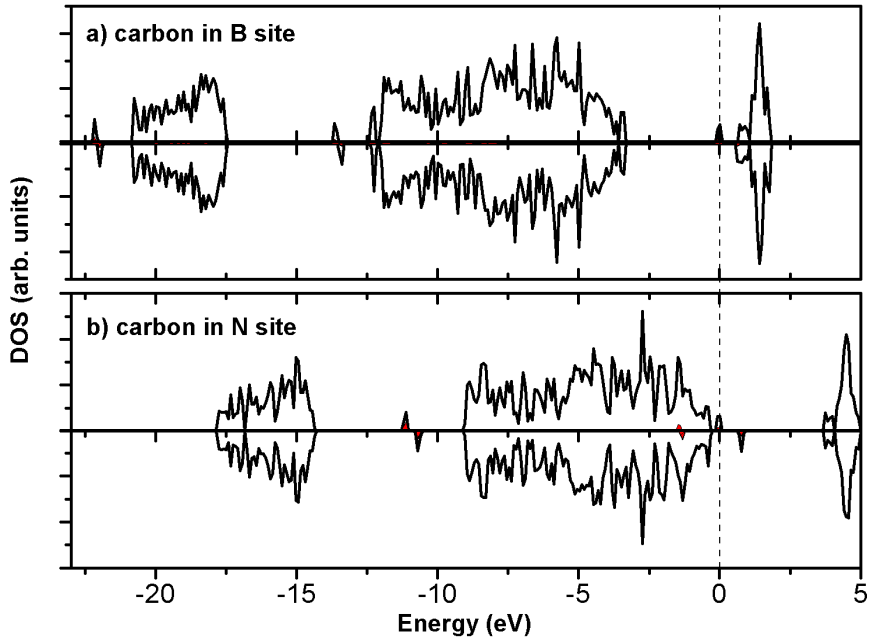

Figure 4.7: Spin density of states for single carbon absorption. Upper panels represent the majority spin (spin-up) states and lower ones represent minority spin (spin down) states. Both structures show metallic character as majority spin states pin up the Fermi level.

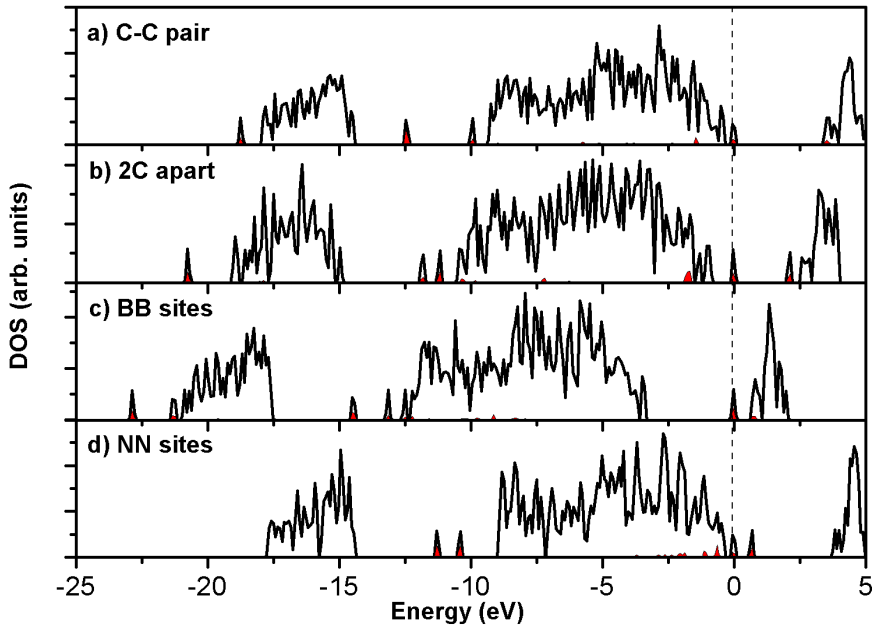

Figure 4.8: Density of states for various double carbon substitutions.

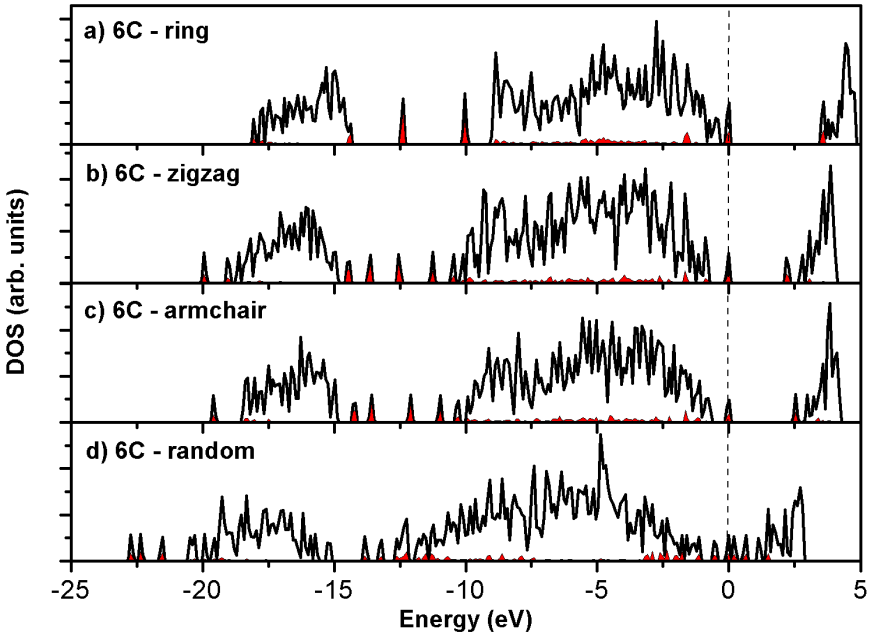

Figure 4.9: Density of states for six (ring, zigzag, armchair and random) carbon substitutions.

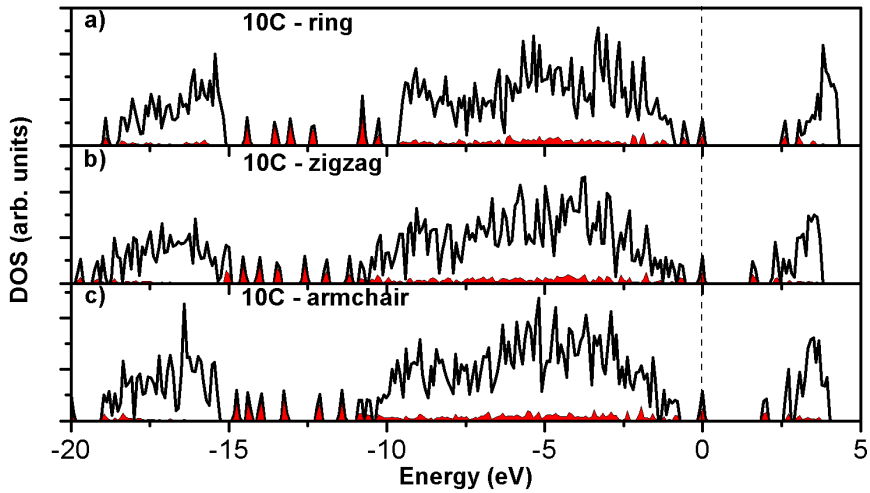

Figure 4.10: Density of states for ten (ring, zigzag, armchair) carbon substitutions.

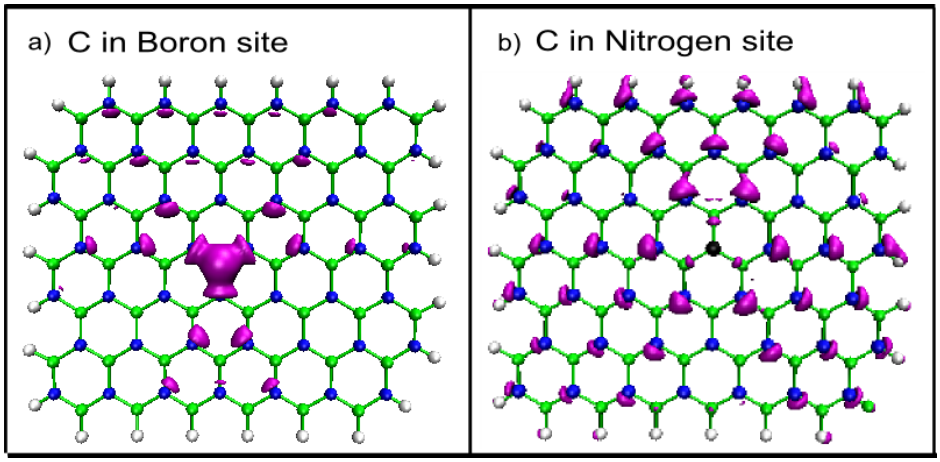

Figure 4.11: Electron density difference for single carbon substitution with respect to BN layer. Since in BN layer the charges are congregate in N sites, we have excess charge on carbon for boron replacement.

Structure	Defect en. (eV)	Magnetic mom. (μ)	C-N	C-B
C on B planar start	6.89	0.0673	1.573	1.576
C on B	6.83	0.0702	1.567	1.605
C on N planar start	6.81	2.0	1.633	2.149
C on N	6.86	2.0	1.635	2.135
C on BN bond pl.	6.77	2.0	1.595	1.775
C on BN bond	6.82	2.0	1.603	1.797
C on top of hex. pl.	6.81	2.0	1.637	2.167
C on top of hexagon	6.85	-0.0305	1.525	1.647 - 1.646

Table 4.6: Defect energies, magnetic moments and C-B/C-N bond lengths for carbon adsorption into BN layer. Data includes both planar and non-planar cases.

final geometries are shown in Fig. 4.15. The names in the figure refers to initial geometries such that carbon is initially placed on top of boron, nitrogen, BN bond or center of hexagonal ring. When the initial position of carbon is on boron atom or on top of BN bond it moves toward the nitrogen atom slightly and makes bonding with both boron and nitrogen. But, when starting on nitrogen atom carbon do not move appreciably and makes bonding with nitrogen only. Table 4.15 tabulates the defect energies, magnetic moments and C-N/C-B bond lengths for the final geometries of carbon adsorption.

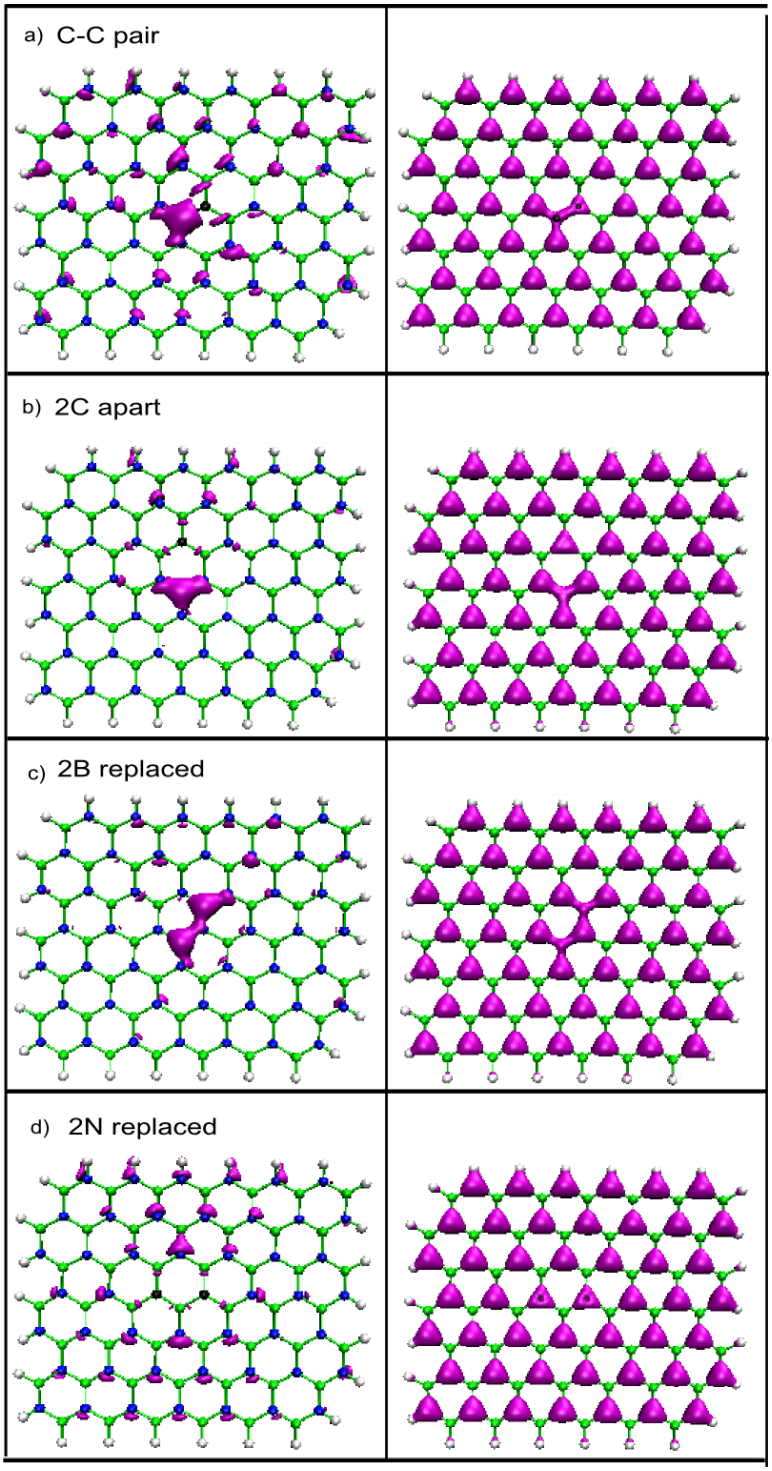

Figure 4.12: Electron density difference with respect to BN layer and total charge distribution for double carbon substitution.

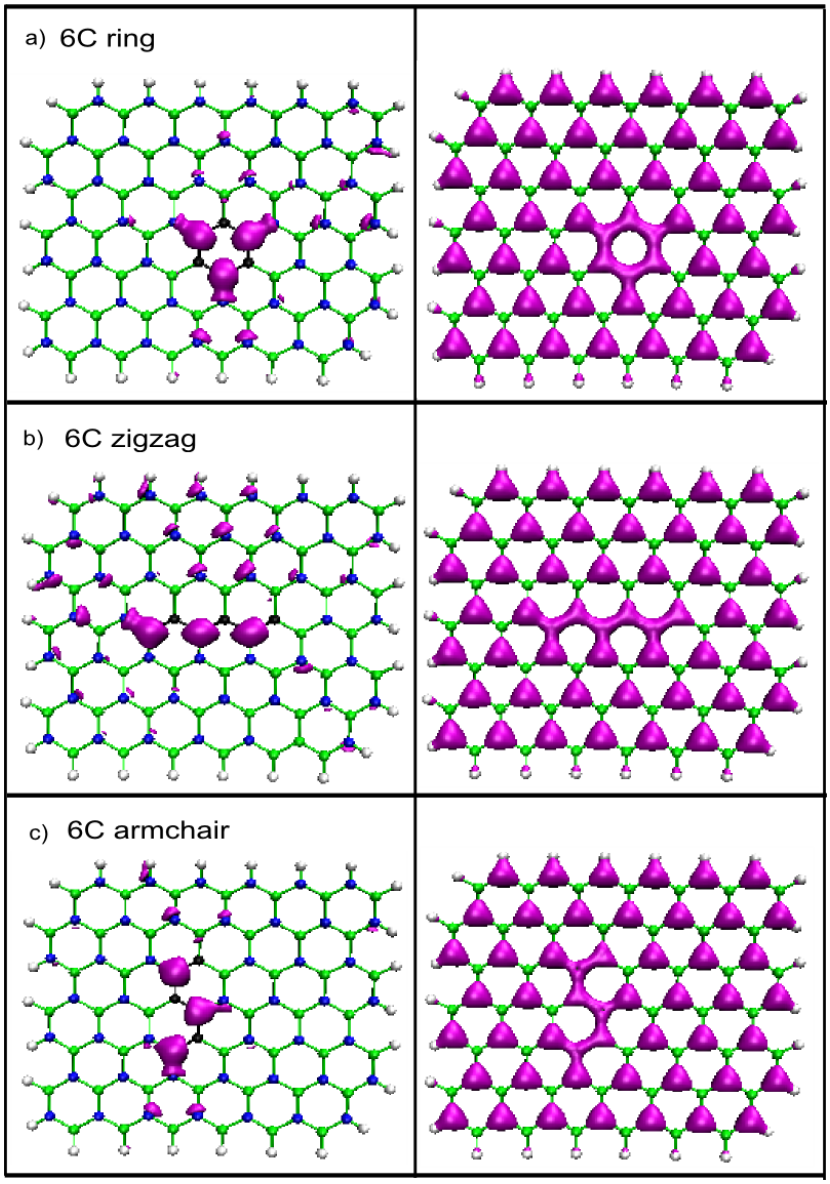

Figure 4.13: Electron density difference with respect to BN layer and total charge distribution for six carbon substitution.

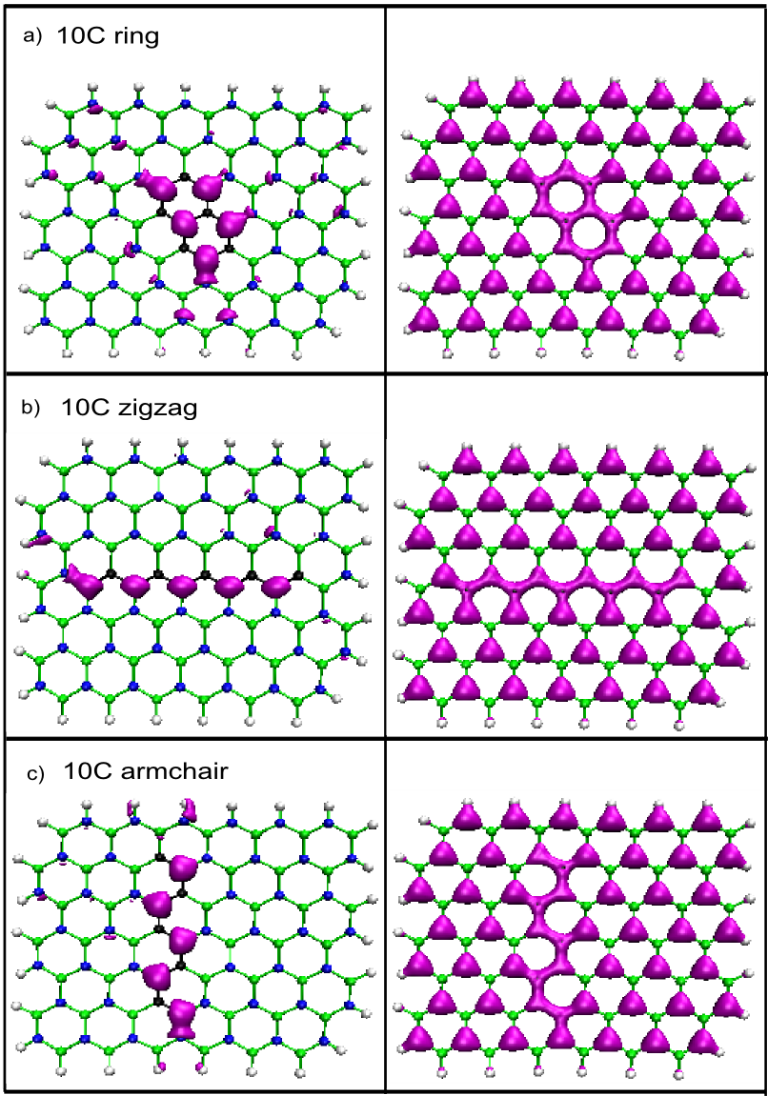

Figure 4.14: Electron density difference with respect to BN layer and total charge distribution for ten carbon substitution.

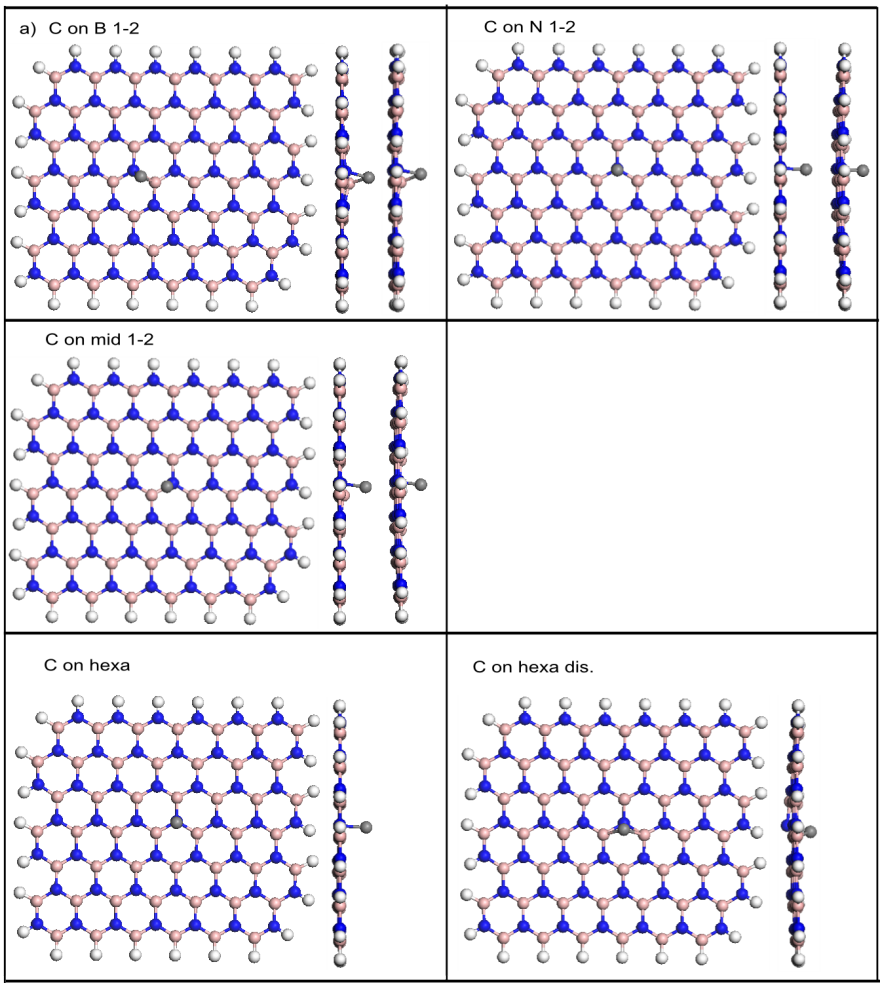

Figure 4.15: Single carbon adsorption into BN layer. When the initial position of carbon atom is on boron atom or on the top of B-N bond, carbon prefers to make bonding with both B and N. But for initial geometries such as carbon is on nitrogen or is on hexagonal ring, carbon makes bonding with nitrogen only.

4.3 Vibrational spectroscopy of B-C-N films

In order to calculate the phonon density of states and the vibrational modes of BNC ternary structures, we used the frozen-phonon formalism. The classical equations of motion for the nuclear positions are

$$M_I \frac{\partial^2 \mathbf{R}_I}{\partial t^2} = \mathbf{F}_I(\mathbf{R}), \tag{4.2}$$

where $\mathbf{R}_I$ is the set of nuclear coordinates for each atom. The forces in Eq. 4.2 can be determined by Hellmann-Fenyman theorem as

$$\mathbf{F}_I(\mathbf{R}) = -\frac{\partial}{\partial \mathbf{R}_I} E(\mathbf{R}). \tag{4.3}$$

In terms of harmonic approximation, the vibrational modes can be defined as

$$\mathbf{u}_I(t) = \mathbf{R}_I(t) - \mathbf{R}_I^0 = \mathbf{u}_I e^{i\omega t} \tag{4.4}$$

where $\mathbf{R}_I^0$ is the equilibrium position of atom I at where the total force acting on that atom is zero.

In quantum mechanics, most of the properties can be determined by the variations of total energy. The small changes around equilibrium positions treated as perturbations and the derivatives of total energy with respect to these perturbations gives quantitative information about the mechanical, electrostatic, magnetic and thermal properties of the system. By this scope, the force coefficients are defined as

$$C_{I,\alpha;J,\beta} = \frac{\partial^2 E(\mathbf{R})}{\partial \mathbf{R}_{I,\alpha} \partial \mathbf{R}_{J,\beta}}. \tag{4.5}$$

Combining Eq. 4.5 and Eq. 4.4 with Eq. 4.3 gives

$$-\omega^2 M_I u_{I\alpha} = -\sum_{J\beta} C_{I,\alpha;J,\beta} u_{J\beta}. \tag{4.6}$$

Then the full set of solution can be determined by solving the dynamical matrix as

$$\left| \frac{1}{\sqrt{M_I M_J}} C_{I,\alpha;J,\beta} - \omega^2 \right| = 0. \tag{4.7}$$

The eigenvalues of the above equation is the independent phonon frequencies of the structure. Considering the lattice symmetry, i.e. the Bloch theorem and the translation periodicity, the eigenvectors can be written as

$$\mathbf{u}_{s,\mathbf{T_n}} = e^{i\mathbf{k}.\mathbf{T_n}} \mathbf{u}_s(\mathbf{k}) \tag{4.8}$$

where s denotes the atom in the cell $\mathbf{T_n}$. With the help of Eq. 4.8 the dynamical matrix and force coefficients will be

$$\left| \frac{1}{\sqrt{M_s M_{s'}}} C_{s,\alpha;s',\beta}(\mathbf{k}) - \omega^2_{i\mathbf{k}} \right| = 0 \tag{4.9}$$

and

$$C_{s,\alpha;s',\beta}(\mathbf{k}) = \frac{\partial^2 E(\mathbf{R})}{\partial \mathbf{u}_{s,\alpha}(\mathbf{k}) \partial \mathbf{u}_{s',\alpha'}(\mathbf{k})}. \tag{4.10}$$

Initially, one has to perform accurate structural minimization in order to find the equilibrium position of the structure. Then finite displacements should be applied to atoms for all degrees of freedom and with self-consistent calculations the forces on individual atoms should be calculated. The force constants can be calculated via Eq. 4.9 and the dynamical matrix can be produced by Eq. 4.8. The required number of displacements are strongly related by the symmetry of the structure, i.e. the symmetry operations can be applied to the system and the symmetric elements of dynamical matrix can be calculated without calculation. For small primitive cells one has to use supercell approximation in order to avoid self-interaction. For instance, if the cell has a few angstrom lattice constant the displaced atom acts force on the neighbor cell and hence on itself which causes an error in the calculation. Therefore, one has to perform test calculations to

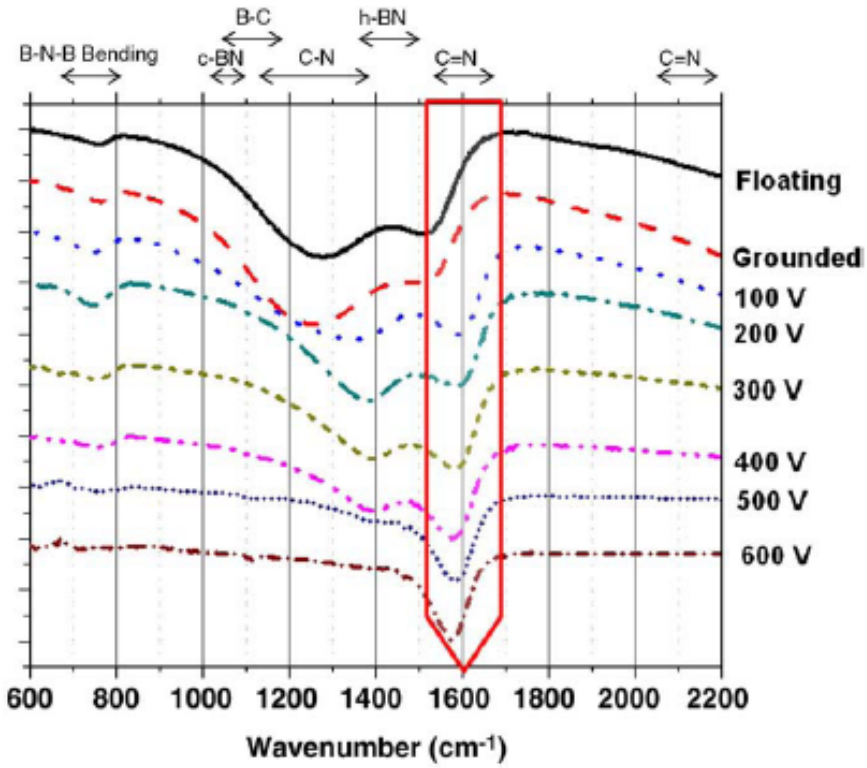

Figure 4.16: GIR-FTIR spectrum of BNC ternary structures for different substrate bias voltages [61]. The oscillation frequencies of some bonds are indicated in the figure and there is an unidentified band between 1500 and 1580 cm^{-1} above -100 V bias. Reproduced from Reference [61].

determine the appropriate supercell dimension, that is the self acting force should be lower than force criteria. Another important parameter is the displacement distance. If the parameter is too large it will be out of harmonic region and anharmonic terms will not be negligible. If the parameter is too small, then one can not get applicable forces.

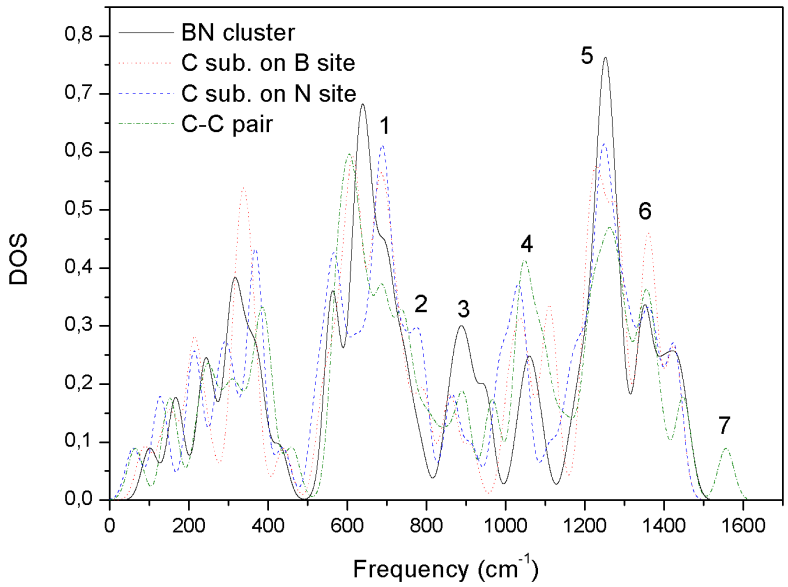

Figure 4.17: Phonon density of states in terms of phonon frequencies for BN pristine, single carbon substitution into boron site and nitrogen site and double carbon substitution which makes C-C pair. These structures are also given in Fig. 4.1 and 4.2.

In our calculations, the structures are already in supercells, for instance, we leave 10 $\AA$ vacuum at least for all directions. We have 122 atoms in each of the supercells, therefore 366 calculations are required for each system. Considering the computational opportunities, we fixed some of the surrounding atoms to decrease such a massive computational effort. 24 atoms (or 26 atoms depending on the structure), especially carbon atoms and first and second neighbors, are free to move which results in total of 72 (or 78) displacements were performed for each system. We used 0.02 $\AA$ displacements for all the calculations.

Recently Bengü group synthesized boron, nitrogen and carbon films using RF deposition technique [61]. Moreover they published the grazing incidence

reflection-Fourier transform infrared (GIR-FTIR) data of BNC films. The obtained data is shown in Fig. 4.16 in which the GIR-FTIR spectra of various substrate bias settings is also given. Moreover, they indicate that there is an unidentified band between 1500 and 1580 cm^{-1}. In this section we show the phonon spectrum of BNC clusters. The phonon density of states for boron nitride pristine, single carbon substitution on B site and N site and C-C pair are shown in Fig. 4.17.

The unique peak, labeled by 7 in Fig. 4.17, appears only in C-C pair structure which suggest that this peak is the consequence of the C-C bond oscillation. The oscillation of the atoms of the mode with frequency 1556 cm^{-1} is drawn in Fig. 4.18. The length of the arrows are proportional with oscillation amplitudes and the colors indicate the amplitudes also (red to green). From the figure, it is clear that this mode is dominated by C-C bond oscillation and unidentified band at Bengü groups paper [61] is now clear. Moreover, this result indicates that carbon atoms tends to aggregate in BN films.

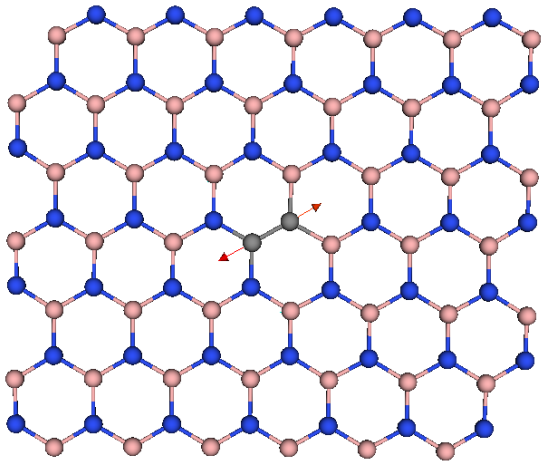

Figure 4.18: The displacement directions of atoms for C-C pair formation at 1556 cm^{-1}. The length of the arrows are proportional with the amplitudes. The phonon band at labeled by 7 in Fig. 4.17 is the consequence of C-C pair oscillation. That is the unidentified band at Reference [61] is due to C-C interaction.

The same argument is much more clear when we examine the phonon spectrum of ring, zigzag and armchair formations of carbon atoms in BN films. The phonon density of states for these structures is given in Fig. 4.19. Similarly, there are band formations between frequencies 1500 and 1600 cm^{-1} which are due to

C-C oscillations. We figured out the modes of these structures at high frequency regime in Fig. 4.20. For the ring structure, the carbon atoms with nitrogen neighbor oscillates in phase and the other carbons oscillate out of the phase. The two carbon atoms at the middle oscillates like C-C pair and gives the highest amplitude for the zigzag structure. Finally, for armchair the carbons atoms oscillates in pairs too. For this system, we also have a mode with frequency 1565 cm^{-1} which has the same vibrational character.

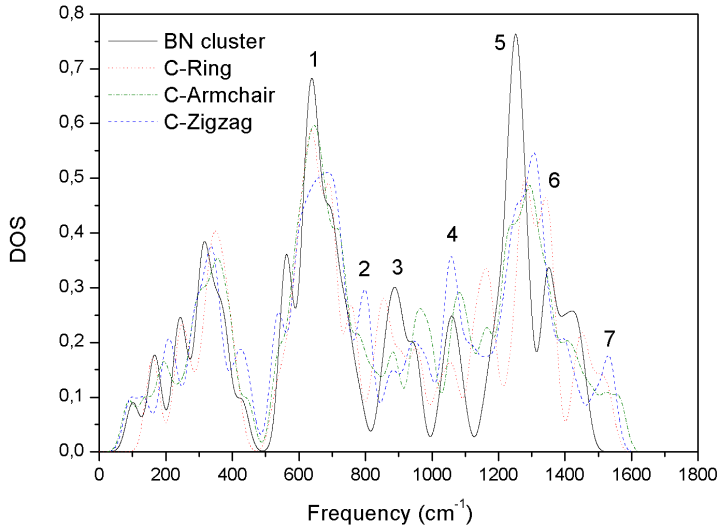

Figure 4.19: The phonon density of states for ring, armchair and zigzag formations of carbon atoms in BN pristine. Solid line represents the BN structure as a reference. These structures are also given in Fig. 4.3.

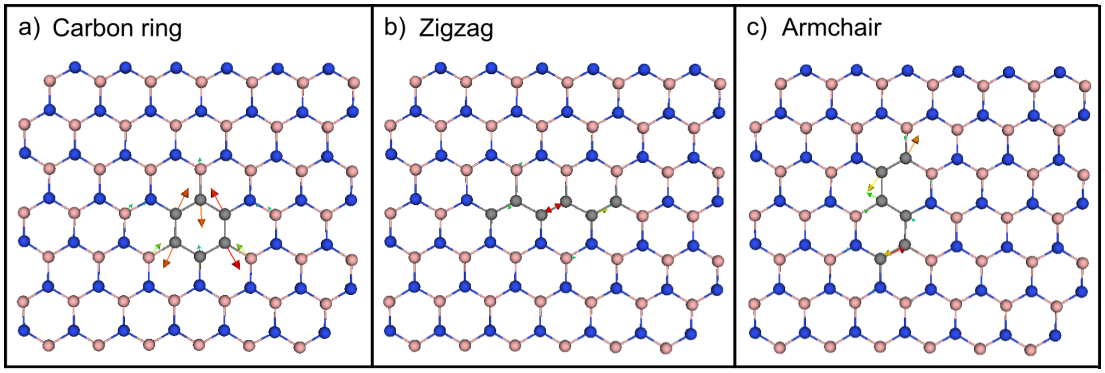

Figure 4.20: The displacement directions for carbon ring, zigzag and armchair structures embedded in BN pristine. The frequencies correspond to these oscillations are; a) 1501 cm^{-1} for ring b) 1536 cm^{-1} for zigzag and c) 1523 cm^{-1} for armchair structures. The length of the arrows (and the colors) indicates the oscillation amplitudes.

Chapter 5

Effect of graphene defects and sulphur adsorption on carbon nanotube growth

5.1 Introduction

Carbon, having flexibility in bonding like sp, sp^2 or sp^3, may be included in many compounds with very different geometrical structures and exhibit various electronic and mechanical properties. With the same flexibility, it can be found in 0D (Fullerenes), 1D (CNTs)[62], 2D (Graphene)[63, 64], and 3D (Diamond, Graphite) forms. In CNTs and graphene, carbons make sp^2 bonding leaving one of their electrons, namely p_z electron unbounded.

Graphene, a single layer of graphite, is a two dimensional material having zero band gap. Although, it was believed that it could not be stable and cannot exist, in 2004 Novoselov et. al made a breakthrough for graphene and they managed to synthesize graphene in laboratory environment[65]. Later on, experiments related with graphene were able to fulfill many theoretical expectations such that graphene has such a band structure that charge carriers are indeed massless Dirac fermions and go ballistic as it was expected[66, 67]. The ballistic

transport property, as well as many other properties made graphene a popular material to work on. Researches on transport properties under the exposure of gaseous molecules [68, 69] show that graphene can be used as a sensor with high sensitivity and response time [70]. Also, it is shown that electronic and magnetic properties can be modulated by doping with boron, nitrogen, phosphorus, sulphur etc [71, 72, 73, 74]. Many researches were made to open a tunable band gap on graphene with using various methods such as doping [70, 75, 110, 111, 114], chemical functionalization[76, 77, 78], using electric fields[79]. A recent work showed that it is possible to open a band gap in the band structure of graphene by doping with sulphur atoms[75]. Graphene nano-ribbons are graphene with finite size which makes them one or zero dimensional materials. They can have band gaps depending on their shapes and sizes. It is a huge research area by itself. Energy band gap engineering [80, 81, 82], transport properties [83, 84, 85, 86], impurities [87], effect of electric field [88, 89, 90], edge effects [91, 92] are some examples. There are even some works to use them as a molecular switch [93].

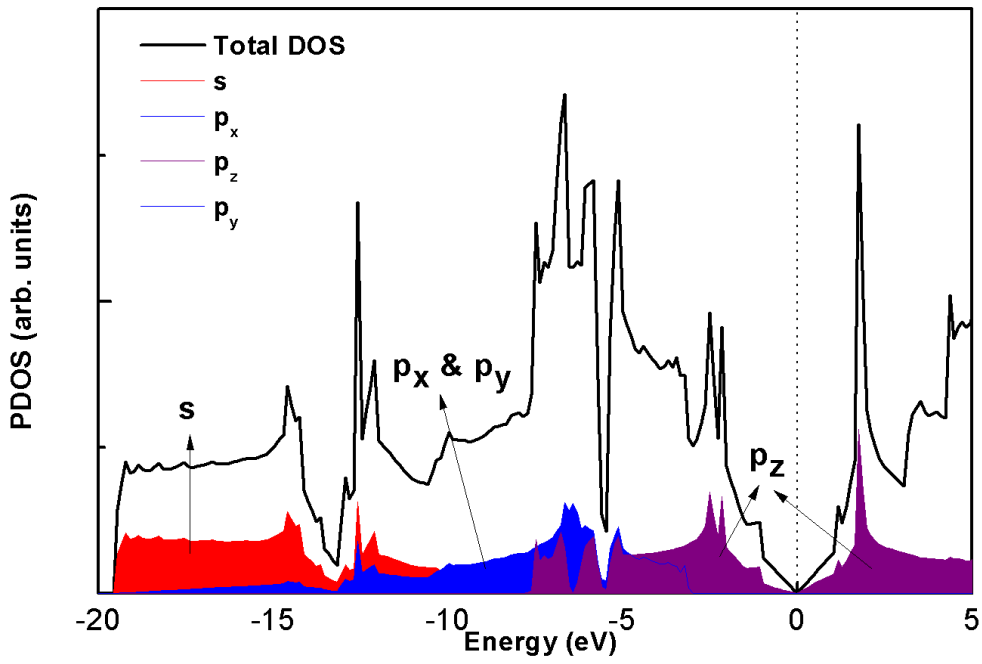

Figure 5.1: Density of states of graphene as well as PDOS over different orbital. Fermi energies are set to zero.

Carbon Nanotubes are rolled up versions of graphene. After the discovery

of CNTs by Iijima in 1991, the number of researches on CNTs grow enormously [95]. They are one dimensional materials showing different band gaps depending on their chirality and radii [94]. Also, mechanical properties of CNTs are very unique. Although, they are very soft in radial direction and can change their shape elastically, they are very stiff in axial direction [94]. There are many applications foreseen for CNTs such as nanosized electronics [96, 97, 98], Li ion batteries [99], hydrogen storage devices [100, 101], molecular sensors [102, 103], field emission sources [104], scanning probe microscope tips [105]. Up to date, junctions consisting of two crossed nanotubes have been produced [98].

As another interesting feature, CNTs is can make 2D and 3D networks such as junctions or kinks during the synthesis [120, 107, 108]. The stability of the networks require strong bonding of CNTs with each other at junction regions. Due to their electronic and mechanical properties, these networks can be used as device fabrication [116, 117, 118, 119]. Recent study suggest that non-hexagonal rings produce curved defects on carbon sheet thus these defects may lead junction formation [120]. The fabrication of these networks is a great challenge because the reasoning behind the formation of such structures is not yet known. It is reported that sulphur has a key role in the formation of CNT networks but in these studies the sulphur atoms are not observed at the sidewalls of CNTs or at the junction regions [107, 109, 112, 113]. Only at recent study small concentration of sulphur atoms observed with electron microscopy [106]. DFT calculations can provide eligible information related with interaction between carbon structures and sulphur atoms.

In this section, we first introduce the defect formations such as point defects and kink-like defects on graphene pristine. Then, we present the binding chemistry of sulphur atoms on graphene with and without defects using first principle calculations. Binding energies and formation energies are presented in the text. Moreover, density of states diagrams for these structures are included for the discussion of electronic structures.

5.2 Computational Methods

In this work, we have performed first principle plan-wave calculations [16] within density functional theory (DFT) [15, 12] by the projector-augmented-wave (PAW) potentials [45, 46]. For this purpose, we have used Vienna ab-initio simulation package program (VASP) [47, 48, 49]. The exchange-correlation potential was expressed in terms of generalized gradient approximation (GGA) (Perdew-Wang 91 type) [50]. In order to achieve desired accuracy in calculations, plane-wave cutoff energy is set to 500 eV. In order not to put a boundary condition and see the geometrical changes in the calculations, we have used supercells and introduce 10 Angstroms of vacuum so as to minimize ion-ion interactions. Therefore, we didn't have a periodic system and we only used Γ point as a Monkhorst-Pack [28] mesh in order to model k-point sampling in the Brillouin zone. The partial occupancy around fermi level is treated by Gaussian smearing with a smearing parameter of 0.08 eV. For all calculations energy convergence was within 10^{-5} eV accuracy. In all calculations edges of finite sized structures were saturated by H atoms and then all of the atoms are relaxed to their minimum energy configurations by using conjugate gradient method where total energy and atomic forces are minimized.

5.3 Defects on graphene

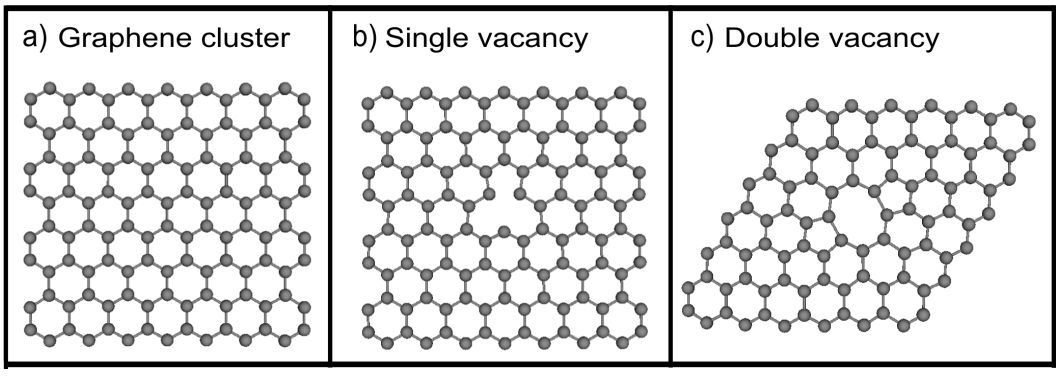

Figure 5.2: Graphene pristine, single vacancy and double vacancy structures. Pentagonal ring is formed near vacancy site at single vacancy and two 5-fold ring and a 8-fold ring are formed at double vacancy.

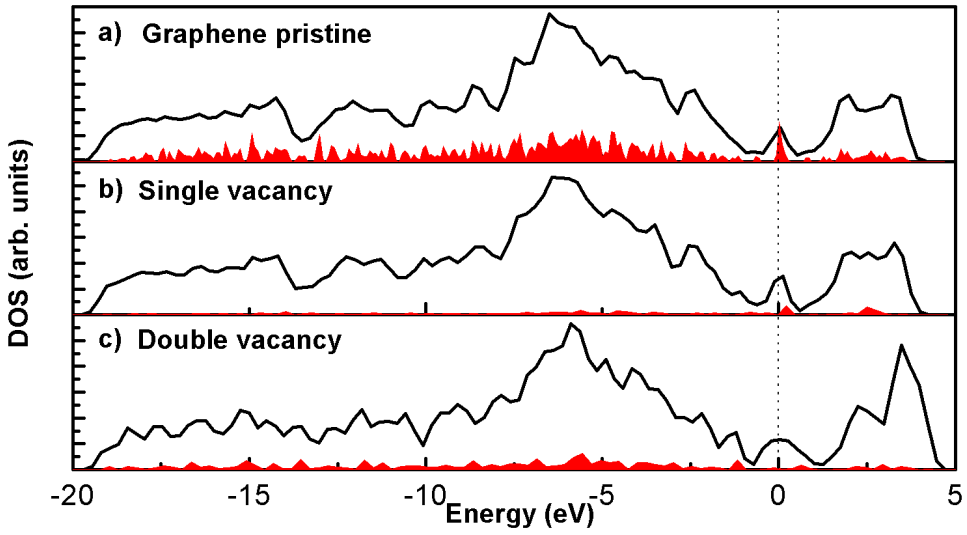

Figure 5.3: Density of states for graphene pristine, single vacancy and double vacancy structures. Fermi energies are set to zero.

Since Y-junction and kink formation play an important role in electronic properties of CNTs, we first tried to determine the defect types which can initiate such formations. The walls of CNTs with large radii can be visualized as graphene monolayer and handling the graphene is much easier than CNTs. Therefore, we performed calculations with graphene. The investigated defects are point defects such as vacancies and n-fold ring defects. The point defect structures such as single and double vacancy and perfect graphene is shown in Fig. 5.2. The single vacancy structure makes pentagonal ring and an octagonal ring near the vacancy site. 5-fold ring makes positive curvature and 8-fold ring negative curvature thus the structure remains almost planar. The distortion is local near vacancy site. We performed spin polarized density functional theory calculation for single vacancy case and get 4 μ_B. For the double vacancy case, we got two pentagonal rings and an octagonal ring.

$$E_{form} = E_{total} - n_C\mu_C - n_H\mu_H. \tag{5.1}$$

where E_{total} is the total energy of the system, μ_C is the chemical potential of carbon taken from graphitic carbon, μ_H is the chemical potential of hydrogen

taken from hydrogen gas and n_C and n_H are the number of C and H atoms in the system, respectively. The calculated formation energies are given in table 5.1. As our aim is to investigate Y-junction and kink formation in CNTs, we worked

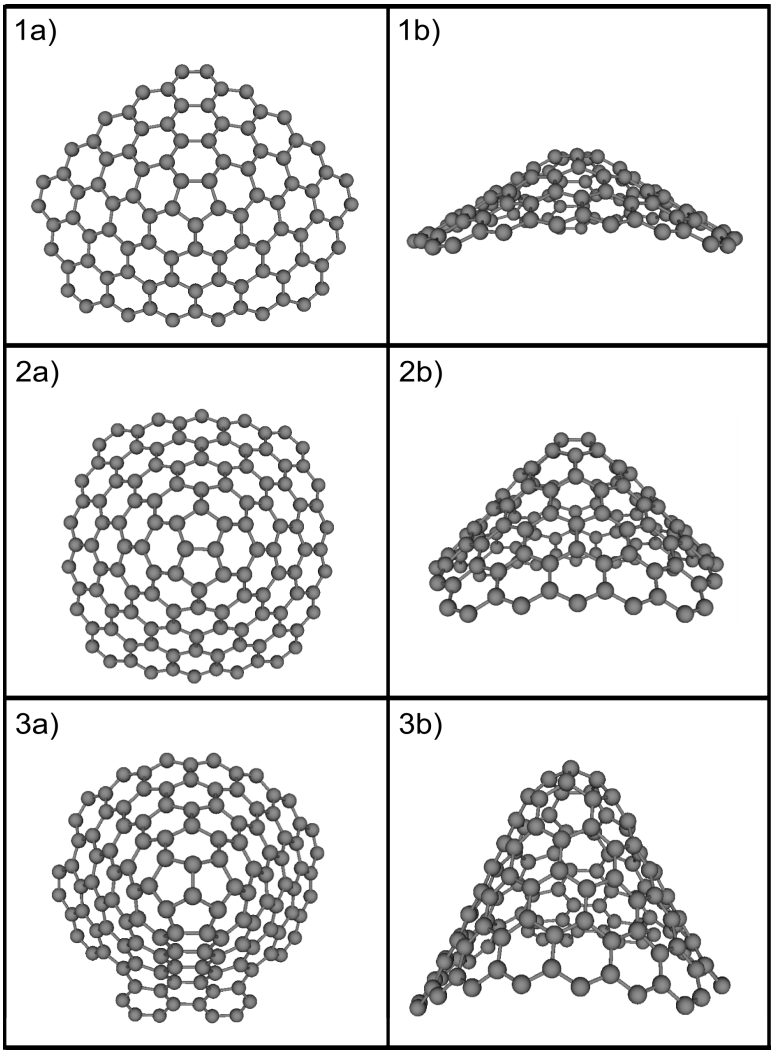

Figure 5.4: 5-fold ring formations on graphene layer. a) Single pentagonal ring, b) Double pentagonal ring, c) Triple pentagonal ring. The curvature increases with the number of pentagons.

on defects with high positive curvature. 5-fold ring defects are good candidates of this type as shown in Fig. 5.4. The three defects in this figure are single pentagonal defect, conjoint double pentagonal defect and conjoint triple pentagonal defect. As it is clear from the figure the curvature increases with the increasing number of pentagons. Similarly the formation energies increases almost linearly

with pentagon number and the most energetic one is the single pentagonal defect with formation energy 5.89 eV. The charge densities of pentagonal defects are illustrated in Fig. 5.5. There was no charge localization observed near pentagonal rings. We made calculations with various other defect types. The final

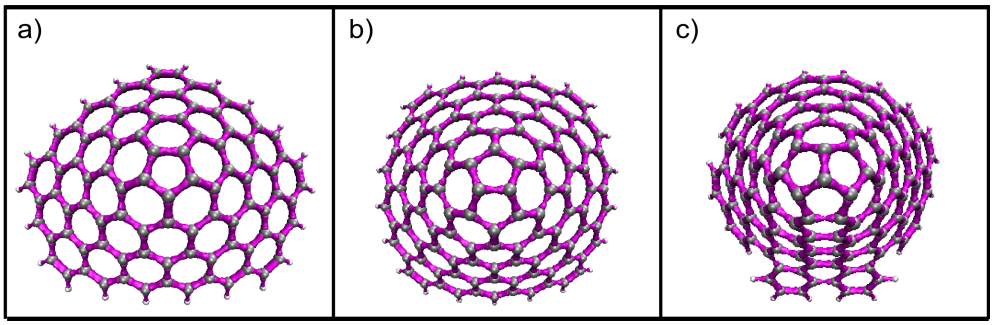

Figure 5.5: Valance charge densities of 5-fold ring formations on graphene layer. The charges are distributed on C-C bonds. There is no excess charge observed on the tip, i.e on pentagon rings.

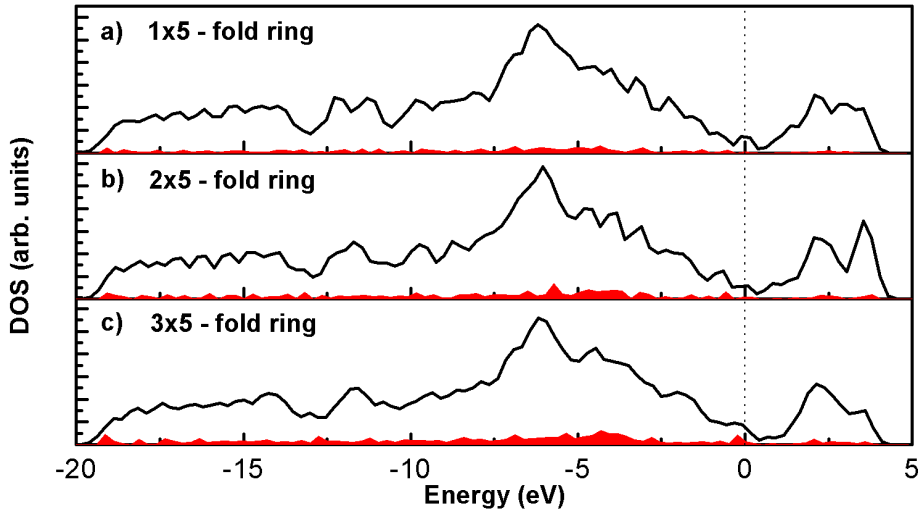

Figure 5.6: Density of states of 5-fold ring formations on graphene layer.

geometries of these defects are shown in Fig. 5.7. 4-fold ring defect made positive curvature similar to 5-fold defects but the corresponding formation energy is higher than single 5-fold defect. Therefore 5-fold ring is a better candidate for 2D network formation. Both 7-fold and 8-fold rings made positive curvature on one direction and negative curvature on another direction. Stone-Wales defect is

Defect Type	Number of Atoms (C H)	Formation Energy (eV)
5-fold ring (1)	94 22	5.89
5-fold ring (2)	120 22	11.06
5-fold ring (3)	124 22	16.37
Single vacancy	119 30	10.65
Double vacancy	94 26	8.98
4-fold ring	80 18	11.18
8-fold ring	104 32	11.73
7-fold ring	66 22	3.70
Stone-Wales defect	76 22	5.10

Table 5.1: Formation energies of defect types on graphene. Point defects such as single, double vacancy and Stones-Wales defect and curved defects such as 5-fold rings, 4-fold, 7-fold and 8-fold rings are investigated. The number of atoms of each structure are also included. The structures are also illustrated in Figs. 5.2, 5.4 and 5.7.

the consequence of 90 degrees rotation of C-C bond which produce 5-7-7-5 rings. The positive curvature of 5-rings and negative curvature of 7-rings cancel each other and the final geometry is almost planar.

5.3.1 Interaction of sulphur with graphene structures

Recent study on synthesis of multi walled carbon nanotubes based on pyrolysis method of sulfuric acid carbonized byproduct of sucrose shows that the sulphur atoms are located around Fe and Ni metal mix [109]. Same study states that sulphur atoms do not exist at sidewalls or junction region based on energy dispersive spectroscopy (EDS) data which is shown in Fig. 5.10. Motivated with this, we performed DFT calculations related with interaction between graphene and sulphur in order to understand the effect of sulphur atom on Y-junction and kink formation of CNTs.

For CNTs with large radii the sidewalls behave like a graphene. First of all, we present the calculations of sulfur atoms on a non-defected graphene-based sheet. Second of all, we introduce the interaction of sulphur atoms on single and double

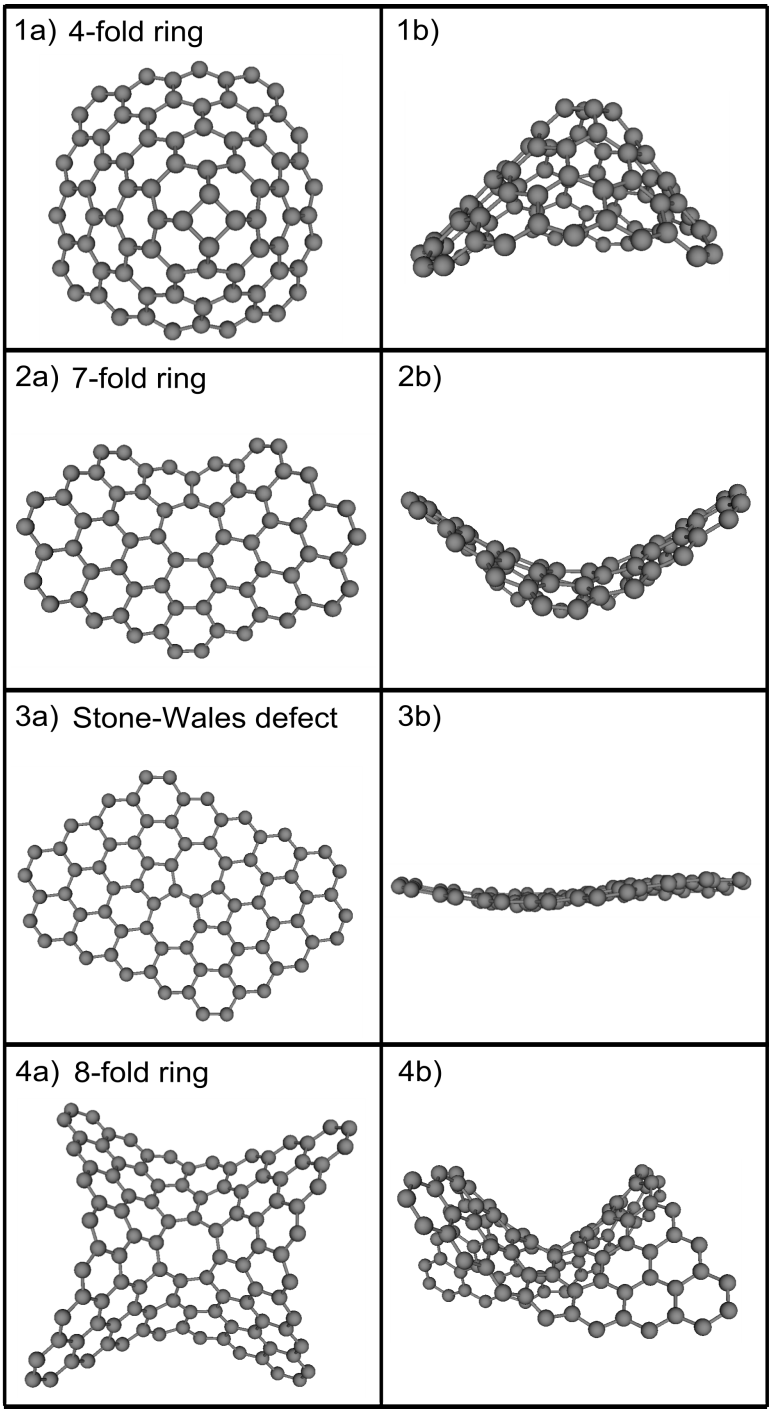

Figure 5.7: 4-fold, 7-fold, 8-fold and Stone-Wales defects on graphene layer. 4-fold ring formation makes positive curvature like 5-fold ring formations. Other structures makes both positive and negative curvature. There are 2 pentagons and 2 heptagons in Stone-Wales defect.

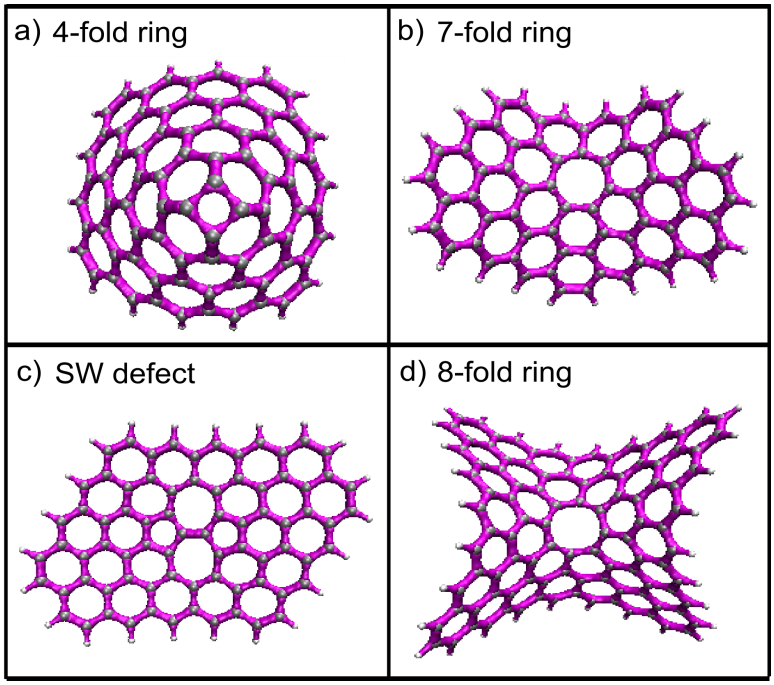

Figure 5.8: Valence charge densities of 4-fold, 7-fold, 8-fold and Stone-Wales defects on graphene layer.

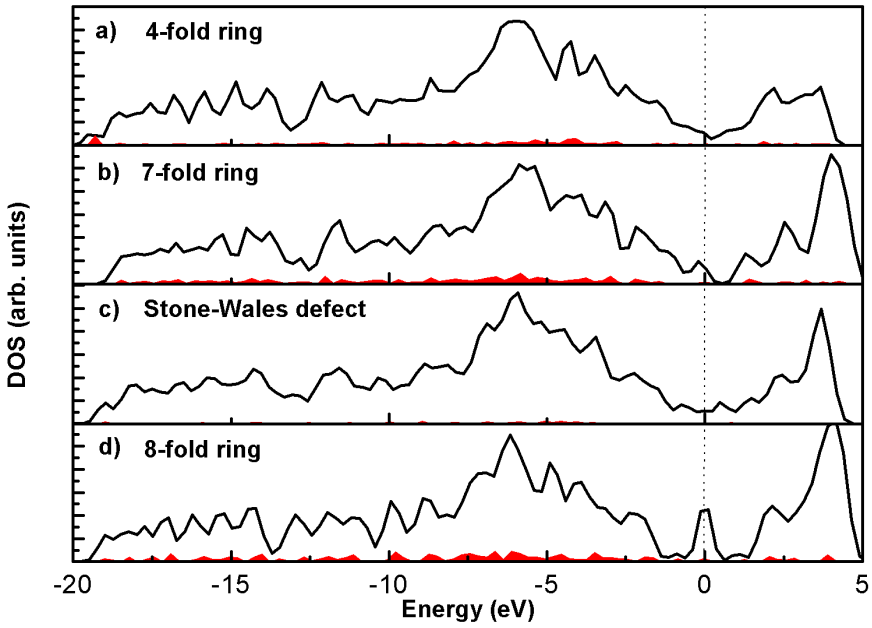

Figure 5.9: Density of states of 4-fold, 7-fold, 8-fold and Stone-Wales defects on graphene layer.

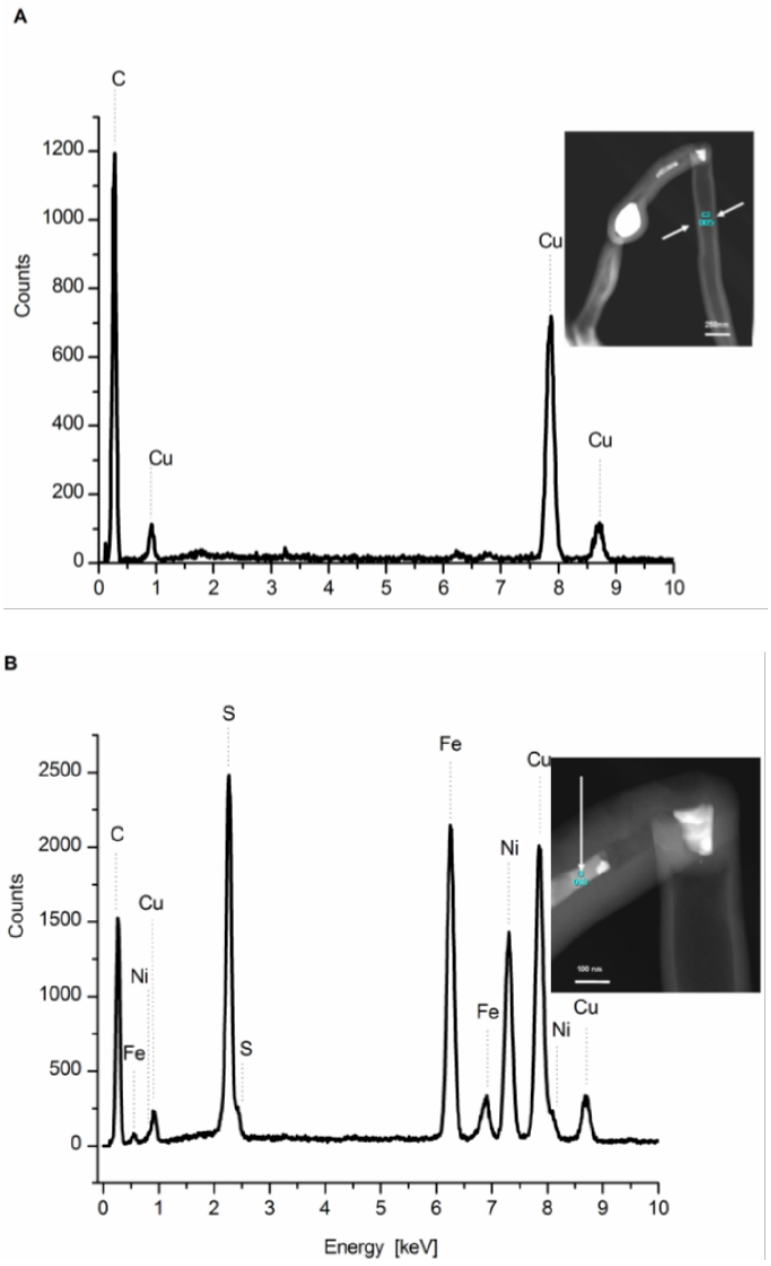

Figure 5.10: Energy dispersive spectroscopy (EDS) analysis of synthesized multi walled carbon nanotubes [109]. a) EDS analysis on sidewalls of CNT shows that there is no peak indicating sulphur existence. b) EDS analysis on Fe and Ni mix showing presence of sulphur.Insets indicate locations for EDS data collection. Reproduced from Reference [109].

vacancy defects of graphene. Finally, we publish the results of calculations with sulphur atoms and 5-fold pentagonal defect. The binding energies (or in some cases the formation energies) and density of states diagrams of these systems are also included. By doing so we can understand the binding mechanisms and chemistries of S atoms on the sides, on the vacancies, on the kinks and on the junctions of CNTs.

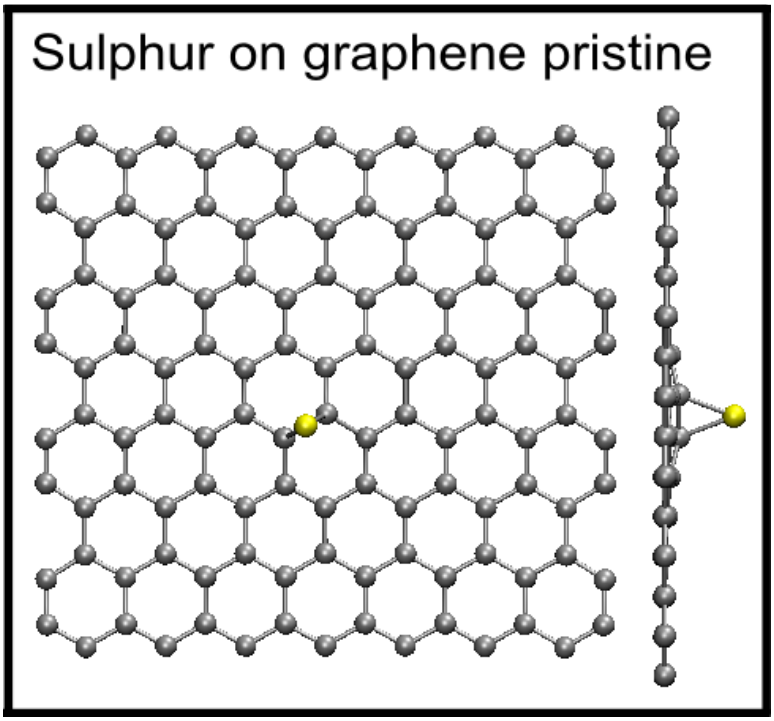

Figure 5.11: Sulphur adsorption on graphene layer both from top view and side view. Sulphur atom sits on top of C-C bond and make bonding with two carbon atoms.

The final geometry of single sulphur adsorption on graphene is given in Fig. 5.11. All starting geometries ends with same final geometry that sulphur adatom situated itself at a valley between two adjacent carbon atoms, effectively chemically bonding to both carbon atoms with a sulfur-carbon bond length of 1.85 Å.

The binding energies of structures under examinations are calculated by the equation

Defect Type	Number of Atoms (C S H)	Binding Energy (eV)
1S	120 1 30	-1.69
2S individual bonding	120 2 30	-3.61
2S - Dimer	120 2 30	-6.49
3S - individual bonding	120 3 30	-5.51
3S - Trimer	120 3 30	-10.53
1S in vacancy - in plane	119 1 30	-7.59
1S in vacancy - out of plane	119 1 30	-4.40
1S in double vacancy	94 1 26	-5.25
2S in double vacancy - same side	94 2 26	-7.62
2S in double vacancy - opposite sides	94 2 26	-9.71

Table 5.2: Binding energies of sulphur adsorption in graphene. The physisorption occurs for dimer and trimer case, thus formation energy of such structures are also given. The chemisorption occurs for other structures. The relaxed structures are given in Figures 5.11, 5.12, 5.13 and 5.14.

$$E_{binding} = E_{total} - E_{ref} - n_S \mu_S. \tag{5.2}$$

where E_{total} is the total energy of the structure, E_{ref} is the total energy of the structure without sulphur, n_S is the number of S atoms and μ_S is the chemical potential of S atom. In order to calculate the corresponding chemical potentials we use the default energy used in calculations in VASP for single S atom.

Table 5.2 shows the binding energies for sulphur adsorption of graphene, single vacancy graphene and double vacancy graphene structures. As seen from the table the binding energy of single sulphur adsorption on graphene is -1.69 eV.

When second sulphur is introduced to the system there will be two different final configuration depending on the starting positions of sulphur atoms. When the distance between the sulphur atoms are large enough to prevent interaction, sulphur atoms are individually bonded to carbon network similar to single sulphur case. The sulphur atoms again make bonding with 2 carbon atoms and the binding energy will be -3.61 eV (or per atom 1.81 eV). When the distance is short enough between sulphur atoms energetically most favorable condition formed by

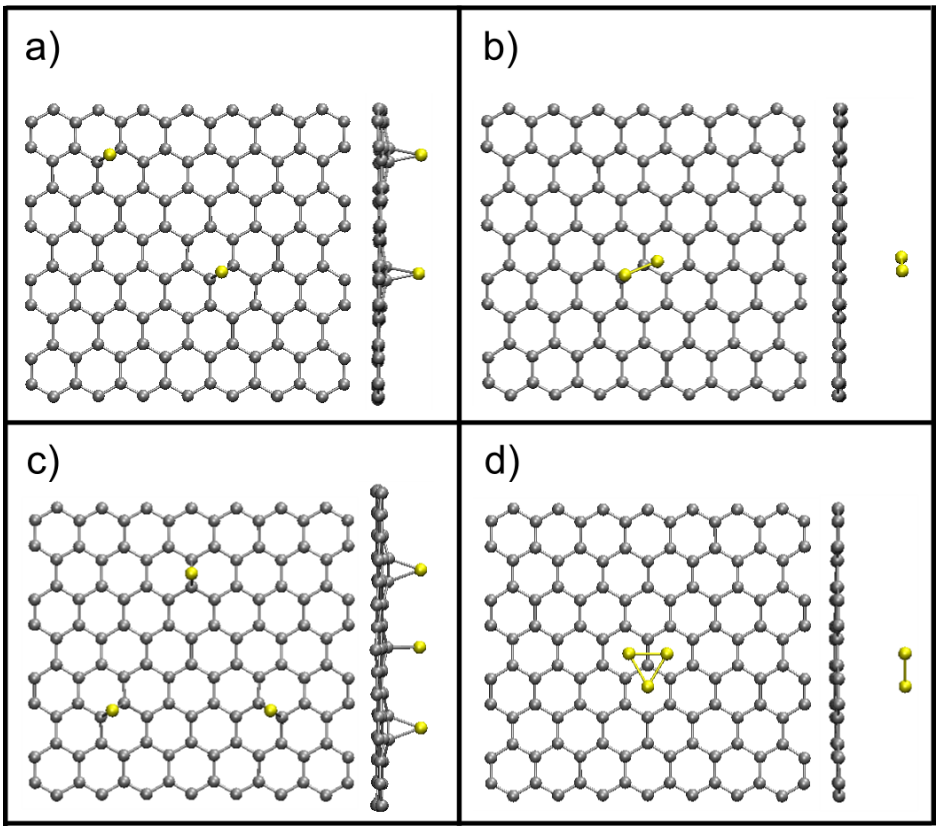

Figure 5.12: Double and triple sulphur adsorption on graphene pristine. If the starting configuration is short enough for sulphur atoms to interact with each other they make dimer (or trimer) and leaves the graphene layer. If the distance is large sulphur atoms are individually bonded.

the dimerization of the two sulfur atoms. These two cases are figured out at Fig. 5.12a and 5.12b. An unexpected outcome of this was the fact that the distance between the sulphur dimer and the underlying carbon network significantly increased with respect to single sulphur adatom case, pointing a weaker interaction between the sulphur and carbon atoms: sulphur-carbon bond length increased to 3.57 Å, while the sulphur-sulphur interaction got stronger. The corresponding binding energy is -6.49 eV, but this energy is the S-S bond energy due to Eq. 5.2. May be the more meaningful result is the formation energy which is defined as

$$E_{form} = E_{total} - E_{ref} - E_{S-dimer}. \tag{5.3}$$

where $E_{S-dimer}$ is the energy of sulphur dimer.

Upon introducing more sulphur atoms to the system leads similar results. Fig. 5.12c and 5.12d shows two different final configuration of three sulphur case. A dimer and a single sulphur atom is also another final configuration. For individual bonding the binding energy is -5.51 eV (or per atom -1.84 eV). Sulphur atoms can make trimer as in Fig. 5.12d.

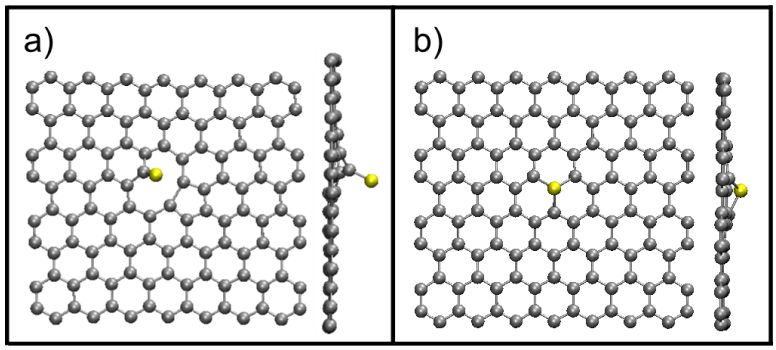

Figure 5.13: Single sulphur absorption on single vacancy defect. Depending on starting configuration sulphur a) can functionalize the dangling bond of carbon atom or b) fills the vacancy site.

We also check the sulphur absorption on single and double vacancy defects of graphene pristine. We started from various initial geometries and the final states for the absorption on single vacancy is given in Fig. 5.13. Sulphur atom can fill the vacancy site as in Fig. 5.13b or can functionalize the dangling bond of carbon

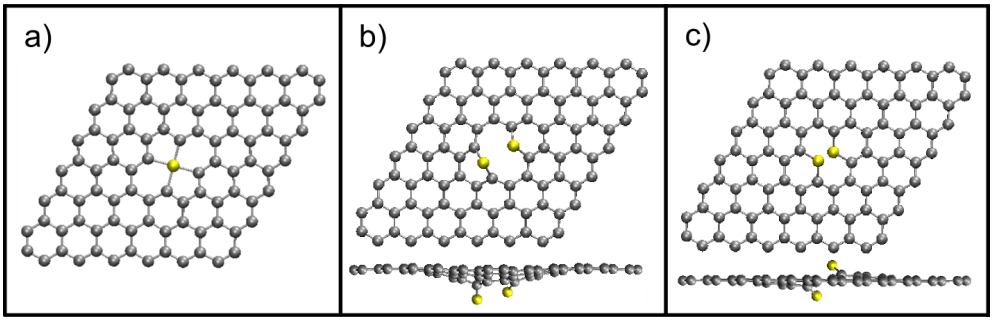

Figure 5.14: Sulphur absorption on double vacancy defect. a) Single sulphur absorption, which fills the vacancy region and structure remains planar. Sulphur atoms make bonding with 2 carbon atoms b) on same side c) on opposite sides.

atom as in 5.13a. For the latter case, the carbon atoms make pentagonal ring on carbon network. The binding energies are -4.91 eV for single bonding and -8.09 eV for triple bonding. The difference of these energies can be attributed to both number of bonds and structural reconstruction. For both cases the deformations are local and we did not observe any curvature which can be basis for Y-junction or kink formation.

The single sulphur absorption on double vacancy defect lead exactly planar structure as in 5.14a. Sulphur atom fills the vacancy site and makes covalent bonding with 4 carbon atoms. Double substitution of sulphur atoms on double vacancy resulted in two different ways. The sulphur atoms may take position on the same side or opposite sides of graphene layer, make bonding with 2 carbon atoms separately and complete their valance shell. When they are at the same side the repulsion due to filled outer shell makes separation between sulphur atoms and hence there carbon network is distorted. When they are at opposite sides they are closer to graphene layer with less structural deformation.

So far we examined the sulphur interaction both with planar graphene and point defect structures like single or double vacancy. For all the systems presence of the sulfur adatoms did not induce a change in the planarity of the carbon network, hence sulfur adsorption by itself may not lead to structural deformations in the CNT side-wall network. Presence of the sulfur substitutional induced some strain locally as shown previous figures, yet this was far from providing a lead toward explaining initial junction geometry due to sulfur presence in the CNT

sidewalls, such as one shown in the 'opening branch' locations by Romo-Herrera et al. [120].

It is well known that capping of CNTs require the presence of non-hexagonal carbon rings following Euler's Law, especially pentagonal ones. In previous chapters dealing with the nano-arch geometry in BN structures, we found that nucleation of non-hexagonal rings lead to the formation of highly strained non-planar geometries. Motivated with this, we have investigated several non-hexagonal defect structures introduced to the planar graphene layer, and in this part we discuss the most energetic cases; a single pentagonal defects as shown in Fig 5.4.1 and Fig 5.4.2, respectively. The curvature induced to the graphene sheet increases with the number of pentagonal defects which implies that this may serve as an initiator for the Y-branching observed for CNTs.

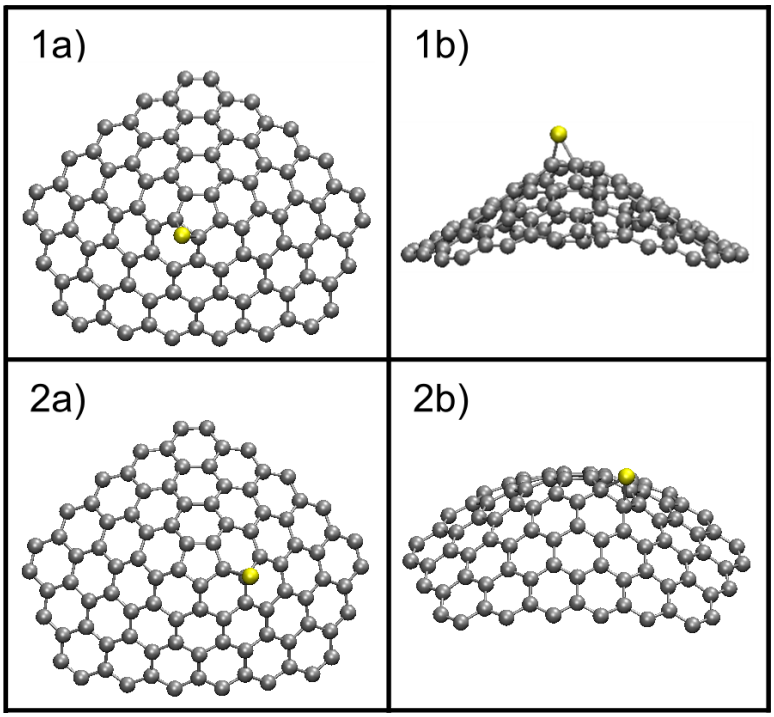

Figure 5.15: Single sulphur adsorption on 5-fold ring defect formation. 1) Similar to the graphene case, sulphur atom make bonding with two carbon atoms. 2) sp^3 type of bonding of carbon at the tip.

Single sulphur adsorption on pentagonal ring is shown in Fig. 5.15. We demonstrate the result for two cases such that sulphur atom make bond with

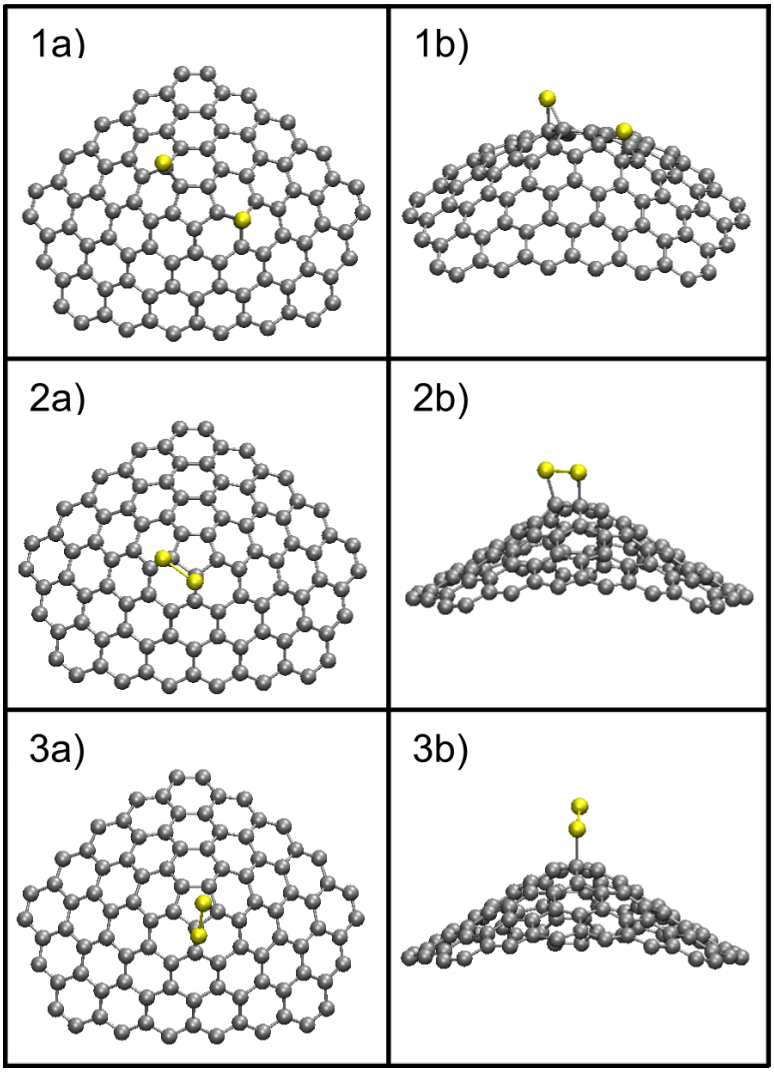

Figure 5.16: Double sulphur adsorption on 5-fold ring defect formation. 1) Sulphur atoms are individually bonded, 2) bridge formation on the tip and 3) dimer formation. The dimer formation is not separated from defect structure (chemisorption to physisorption).

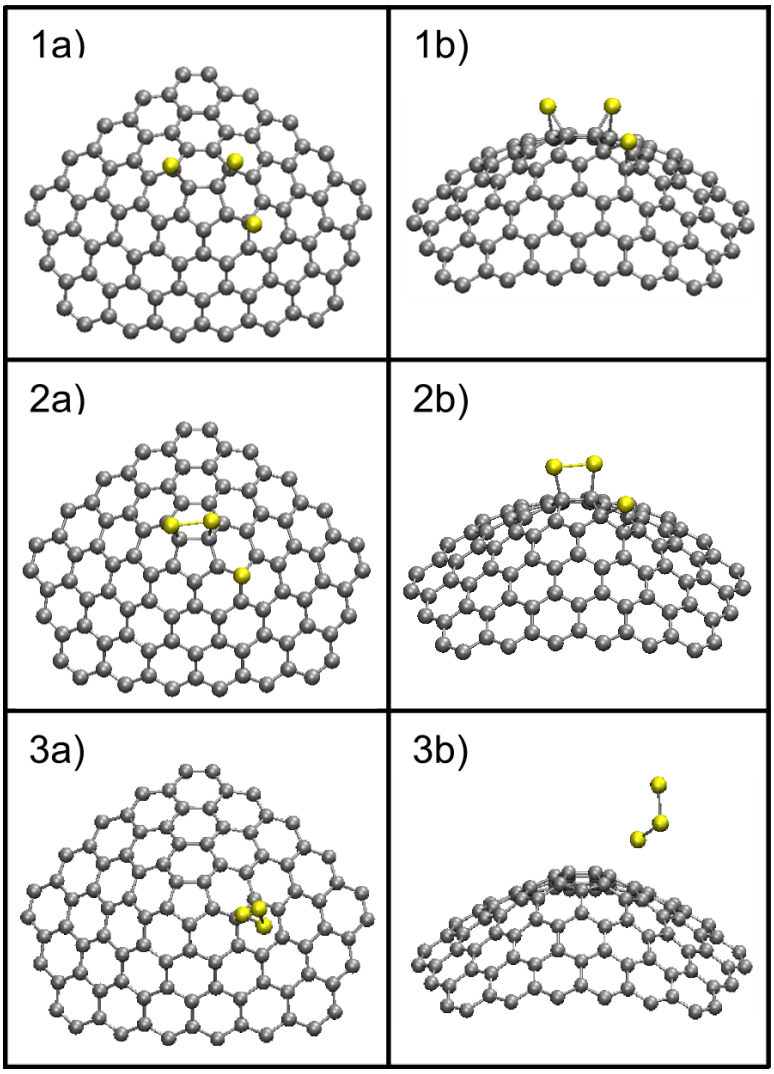

Figure 5.17: Triple sulphur adsorption on 5-fold ring defect formation. 1) Sulphur atoms are individually bonded, 2) bridge formation on the tip and individual bonding, 3) .

carbon atoms in pentagonal ring and make bond with one carbon atom in pentagonal ring and one carbon atom in hexagonal ring (sp3 type of bonding). For both cases sulphur atom prefers to locate on C-C bond, similar to planar graphene calculations. The binding energy, is given in 5.3, of sp^3 type slightly smaller than first case which suggest that sulphur preferred "defected" regions as binding sites as an adatom.

When the second sulphur atom is introduced to the system we observed three different final geometry depending on starting positions of sulphur. The individual bonding of sulphur atoms again exist. Different from our previous calculations the bridge formation on the pentagonal defect is established. Dimerization occurs also for this system but sulphur dimer is not completely removed from graphene defect, physisorption takes place. When we investigate the final structures (Fig. 5.16) and binding energies (5.3) we arrive at some important conclusions.

1 - We found that sulphur preferred "defected" regions as binding sites as an adatom, that is carbon atoms which are members of non-hexagonal rings.

2 - The interaction between the sulphur and carbon atoms remained strong for defected structures, even when sulphur is dimerised.

3 - In none of the cases sulphur binding was observed to induce significant changes in the pre-existing curvature of the carbon networks, where an abrupt increase in the local curvature could be a key step leading to branching.

5.3.2 Conclusion

The results so far shows that there is no direct relationship between Y-junction or kink formation on CNTs and sulphur adsorption as proposed by earlier works. The contradictory result of observation of sulfur at an emerging branch by Romo-Herrera et al. [106] can be explained by interaction of sulphur atoms with defected regions as DFT calculations show. Also, Deepak et al. [108] offered the combined effect of several process parameters for the explanation of the Y-junction morphology even with presence of sulphur in the reactant mixture.

Defect Type	Number of Atoms (C S H)	Binding Energy (eV)
1S on top of bond	94 1 22	-2.78
1S - sp3 type	94 1 22	-2.69
2S - individual bonding	94 2 22	-5.15
2S - bridge	94 2 22	-6.40
3S - individual bonding	94 3 22	-9.54
3S bridge + single S	94 3 22	-8.57

Table 5.3: Binding energies of sulphur adsorption in 5-fold ring defect. Number of atoms in each structure are also given. The optimized structures are shown in Figures 5.15, 5.16 and 5.17.

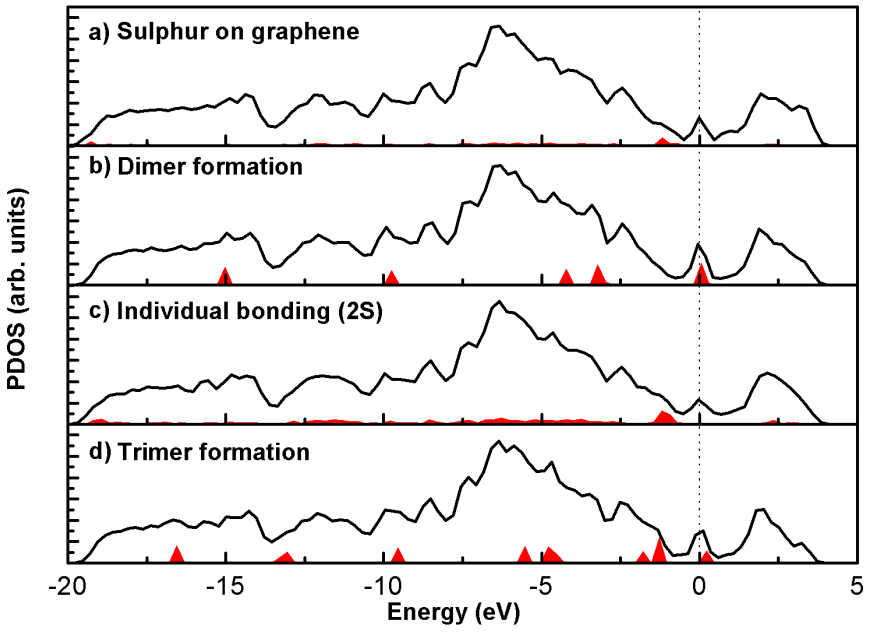

Figure 5.18: Density of states diagram for graphene and sulphur.

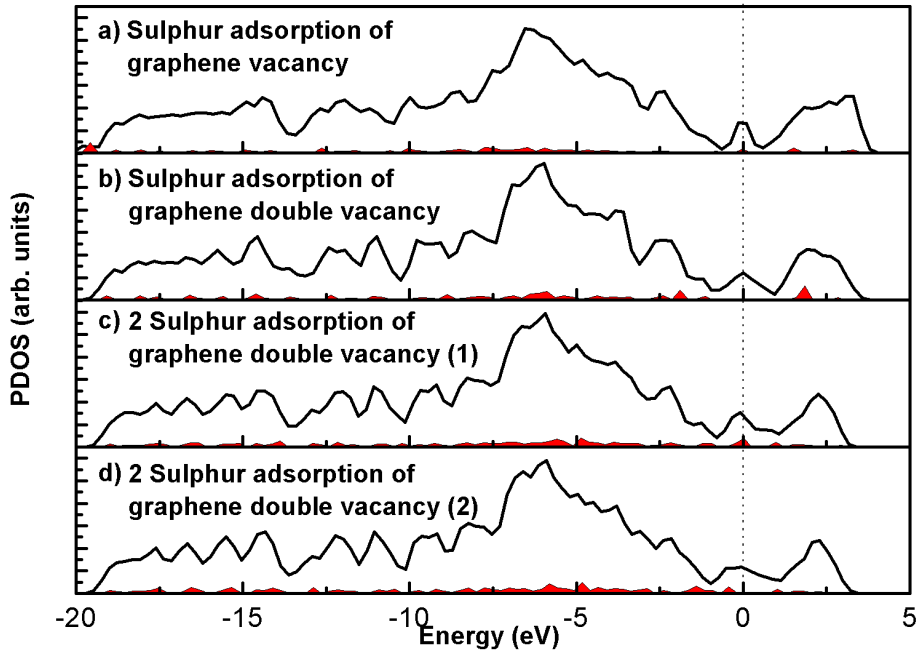

Figure 5.19: Density of states diagram for vacancies and sulphur.

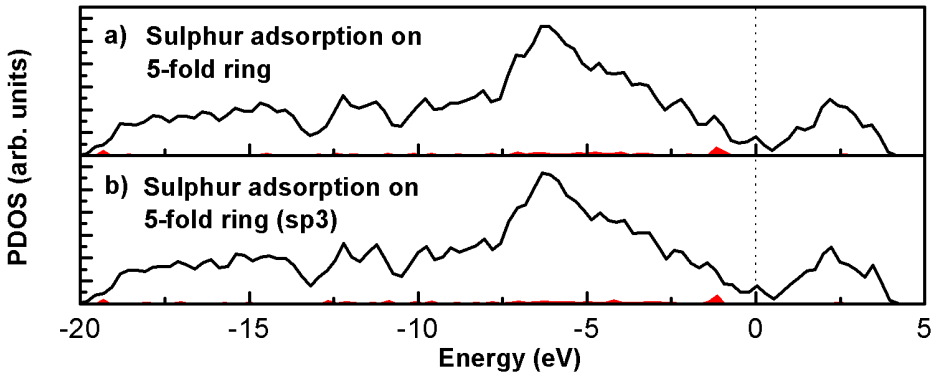

Figure 5.20: Density of states of single sulphur adsorption on 5-fold ring defect structure.

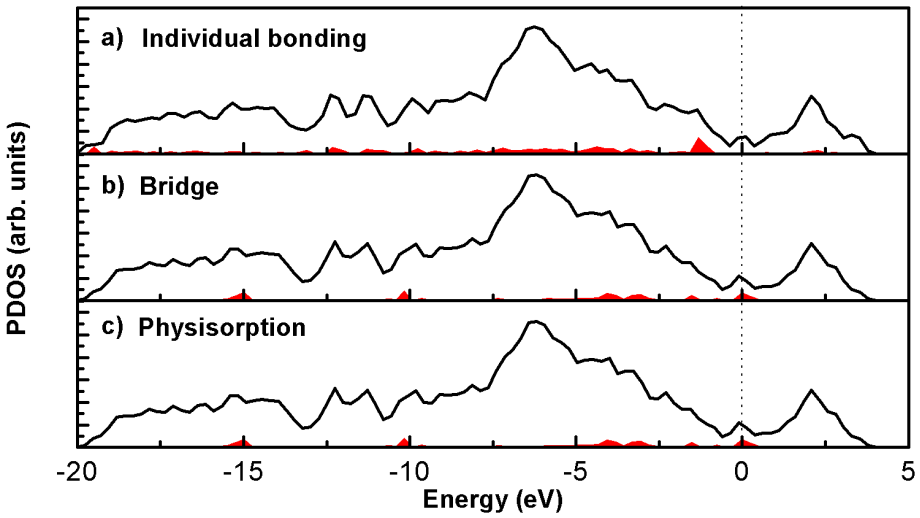

Figure 5.21: Density of states of double sulphur adsorption on 5-fold ring defect structure.

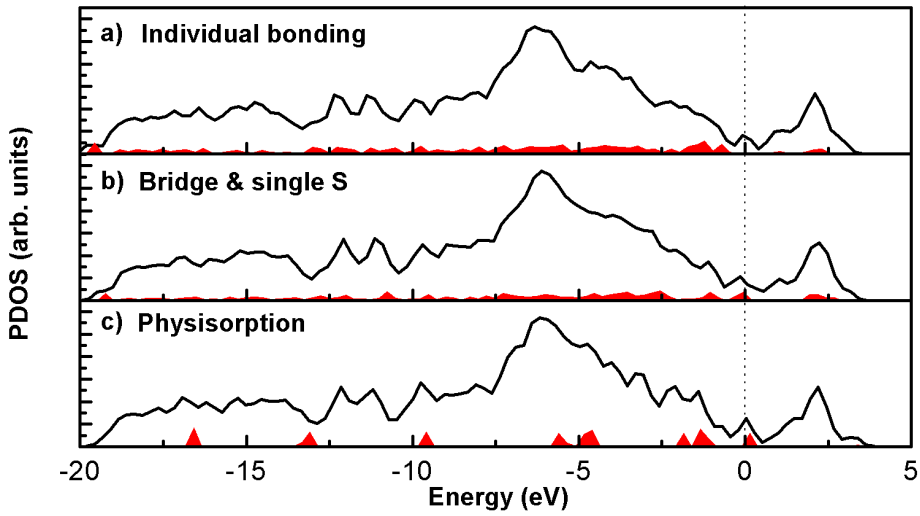

Figure 5.22: Density of states of triple sulphur adsorption on 5-fold ring defect structure.

Chapter 6

Conclusion

In this thesis, we have presented the mechanical and electronic properties of 2D boron nitride and graphene nanostructures based on first-principles calculations. In first chapter, we showed that 4-fold ring defect formation of hexagonal boron nitride can be considered as the metaphase between the hexagonal and cubic phases of boron nitride during cubic boron nitride thin film nucleation. Detailed investigation on various defect types of boron nitride showed that 4-fold and 5-fold pair defects are well matched with experimentally observed defect formations, whereas point defects, such as vacancies and anti-sites, did not bear strong resemblance to that of experimentally observed. Moreover, formation energy analysis in N-rich and B-rich synthesis environments suggest that 4-fold ring is energetically more favorable than other defect types. In addition, we plotted charge density isosurfaces of these defect types. These plots suggest that there is a charge transfer from boron atoms to nitrogen atoms, thus charges aggregate on nitrogen atoms. For the single vacancy cases, we observed defect induced magnetization with magnetic moment 1.0 μ_B due to vacancies. Spin difference charge density isosurfaces showed that the up spin is located at nitrogen atom for boron vacancy case and at three boron atoms for nitrogen vacancy case. The spin density of states point out the difference between up and down spin densities. In addition, dangling bonds at the edges of boron nitrite pristine introduce magnetization and the structure exhibits half-metallic behavior. Hydrogenation

of dangling bonds passivate the magnetization.

In second chapter, carbon aggregation in boron nitride films is investigated. We have performed various calculations for different orientations of different numbers of carbon atoms. Defect energies and formation energy figures in N-rich an B-rich synthesis environments of these B-N-C ternary systems are given. Due to these analysis, the defect energy of carbon atom on boron site is slightly lower than on nitrogen site, therefore carbon atom is initially prefer the position of nitrogen. For the double carbon substitution, pair structure has the lowest defect energy, thus energetically favorable than separated carbon atoms. Therefore, carbon atoms tend to aggregate in boron nitride monolayer. The difference in defect energies is between 2 eV and 4 eV. Substitutions with three or four carbon atoms verified similar results that structures with highest C-C bond have lowest defect energies. Moreover, we have performed calculations with five, six and seven carbon atoms forming ring (or incomplete ring for five carbon substitution), zigzag and armchair structures as well as random distribution of carbon atoms. Hexagonal ring of six carbon atoms has lowest defect energy, even 0.36 eV lower than incomplete ring of five carbon, which is the consequence of high symmetry of the structure. For the ten carbon case, we observed that two hexagonal ring, adjacent to each other, is the most favorable structure. The random distribution of carbon atoms for all B-N-C ternary systems have highest defect energies. In general, we can say that carbon-carbon interaction in BN is so strong that carbon atoms tend to aggregate in BN layer, preferring ring like structures. In this chapter, we also publish the results of phonon frequencies for B-N-C systems. The investigated systems are single carbon structures, C-C pair formation, six carbon ring, zigzag and armchair structure as well as boron nitride pristine. Phonon density of states plots suggest that structures contain C-C bond exhibit extra oscillations after 1500 cm^{-1}, which is clearly explains the unidentified band between 1500 and 1580 cm^{-1} observed in the experiment. The phonon modes at unidentified peak positions are governed by carbon-carbon oscillations from the plotted phonon modes of these frequencies. Therefore, carbon aggregation in boron nitride layer is verified.

In third chapter, graphene defects and interaction of these defects with sulphur

atom is investigated. The 2D and 3D networks, such as Y-junctions, T junctions and kinks, can be occurred with high chance during carbon nanotube synthesis. As the walls of carbon nanotubes with large radius behaves like graphene, we investigated the graphene defects, especially the ones with high curvature, and interaction of sulphur with these defects. Five-fold defects are the good candidates to initiate the junction and kink formation. The curvature is increasing with the number of pentagonal defects. Moreover, sulphur calculations show that sulphur preferred "defected" regions as binding sites as an adatom, that is carbon atoms which are members of non-hexagonal rings. The interaction between the sulphur and carbon atoms remained strong for defected structures, even when sulphur dimerised. In none of the cases, sulphur binding was observed to induce significant changes in the pre-existing curvature of the carbon networks, where an abrupt increase in the local curvature could be a key step leading to branching.

Bibliography

[1] M. Born and J. R. Oppenheimer, Ann. der Phys. **84**, 457 (1927).

[2] P. Güttinger, Z. Phys. **73**, 169(1932).

[3] W. Pauli, Handbuch der Physik, Berlin, Springer. p. 162 (1933).

[4] H. Hellmann, Einführung in die Quantenchemie, Leipzig, Franz Deuticke. p. 285 (1937).

[5] R. P. Feynman, Phys. Rev. **56**, 340 (1939).

[6] D. R. Hartree, Proc. Cambridge. Philos. Soc. **24**, 89 (1928).

[7] V. Fock, Z. Phys. **61**, 126 (1930).

[8] J. C. Slater, Phys. Rev. **35**, 210 (1930).

[9] L. H. Thomas, Proc. Cambridge. Philos. Soc. **23**, 542 (1927).

[10] E. Fermi, Z. Phys. **48**, 73 (1928).

[11] See, e.g., N. H. March in Theory of the inhomogeneous electron gas, eds. S. Lundqvist and N. H. March (Plenum, NY, 1983).

[12] P. Hohenberg and W. Kohn, Phys. Rev. **136**, B864 (1964).

[13] M. Levy, Phys. Rev. A **26**, 1200 (1982).

[14] E. Lieb, Int. J. Quant. Chem. **24**, 243 (1983).

[15] W. Kohn and L. J. Sham, Phys. Rev. **140**, A1133 (1965).

[16] M. C. Payne, M. P. Teter, D. C. Allan, T. A. Arias, and J. D. Joannapoulos, Rev. Mod. Phys. **64**, 1045-1097 (1992).

[17] D. M. Ceperley and B. J. Alder, Phys. Rev. Lett. **45**, 566 (1980).

[18] See, e.g., J. Kohanoff and N. Gidopoulos in The Handbook of Molecular Physics and Quantum Chemistry. Ed S Wilson, Vol. 2, Molecular Electronic Structure, John Wiley and Sons, (2002).

[19] D. C. Langreth and M. J. Mehl, Phys. Rev. Lett. **47**, 446 (1981); Phys. Rev. B **28**, 1809 (1983).

[20] J. P. Perdew and J. Wang, Phys. Rev. B **33**, 8822 (1986).

[21] J. P. Perdew and Y. Wang, Phys. Rev. B **45**, 13244 (1991).

[22] A. D. Becke, Phys. Rev. A **38**, 3098 (1988).

[23] F. Bloch, Z. Physik **52**, 555 (1928)

[24] J. Ihm, A. Zunger, and M. L. Cohen, J. Phys. C: Solid State Phys. **12**, 4409 (1979).

[25] E. Kaxiras, *Atomic and Electronic Structure of Solids* (Cambridge University Press, UK, 2003).

[26] D. J. Chadi and M. L. Cohen, Phys. Rev. B **8**, 5747 (1973).

[27] J. D. Joannopoulos and M. L. Cohen, J. Phys. C **6**, 1572 (1973).

[28] H. J. Monkhorst and J. D. Pack, Phys. Rev. B **13**, 5188 (1976).

[29] R. A. Evarestov and V. P. Smirnov, Phys. Status Solidi **119**, 9 (1983).

[30] A. V. Kanaev, J-P. Petitet, L. Museur, V. Marine, V. L. Solozhenko, and V. Zafiropulos, J. Appl. Phys. **96**, 4483 (2004).

[31] N. G. Chopra, R.J. Luyken, K. Cherrey, V.H. Crespi, M.L. Cohen, S.G. Louie, and A. Zettl, Science **26**, 966 (1995).

[32] D. Goldberg, Y. Bando, O. Stephan, and K. Kurashima, Appl. Phys. Lett. **73**, 2441 (1998).

[33] S.S. Alexandre, M.S.C. Mazzoni, and H. Chacham, Appl. Phys. Lett. **75**, 61 (1999).

[34] L. Vel, G. Demazeau, and J. Etourneau, Mat. Sci. and Eng. B **10**, 49 (1991).

[35] S. L. Rumyantsev et al., in Properties of Advanced Semiconductor Materials GaN, AlN, InN, BN, SiC, SiGe, edited by M. E. Levinshtein, S. L. Rumyantsev, and M. S. Shur (John Wiley and Sons, New York, 2001), pp. 67-92.

[36] R. H. Wentorf, J. Chem. Phys. **36** (1962) 1990.

[37] O. Mishima, K. Era, J. Tanaka, S. Yamaoka, Appl. Phys. Lett. **53**, 932 (1988).

[38] R. H. Wentorf, J. Chem. Phys. **26**, 956 (1957).

[39] F. P. Bundy and R. H. Wentorf, J. Chem. Phys. **38**, 1144 (1963).

[40] P. B. Mirkarimi; K. F. McCarty, and D. L. Medlin, "Review of advances in cubic boron nitride film synthesis", Materials Science and Engineering R Reports **21**, 47-100 (1997).

[41] E. Bengü, L. D. Marks, R. V. Ovalı, and O. Gülseren, Ultramicroscopy **108**, 1484-1489 (2008).

[42] V. L. Solozhenko, Proc. Phys. Chem. **301**, 592 (1988) [Doklady Ac. Sci. URSS].

[43] R. Liu and C. Cheng, Phys. Rev. B. **76**, 014405 (2007).

[44] X. Blase, A. Rubio, S. G. Louie, and M. L. Cohen, Europhys. Lett. **28**, 335 (1994).

[45] P. E. Blöchl, Phys. Rev. B **50**, 17953 (1994).

[46] G. Kresse and D. Joubert, Phys. Rev. B **59**, 1758 (1999).

[47] Computations have been carried out with the VASP software: G. Kresse and J.Hafner, Phys. Rev. B **48**, 13115-13118 (1993).

[48] G. Kresse and J. Furthmüller, Comput. Mater. Sci. **6**, 15 (1996).

[49] G. Kresse and J. Furthmüller, Phys. Rev. B **54**, 11169 (1996).

[50] J. P. Perdew, J. A. Chevary, S. H. Vosko, K. A. Jackson, M. R. Pederson, D. J. Singh, and C. Fiolhais, Phys. Rev. B **46**, 6671 (1992).

[51] C. Collazo-Davila, E. Bengü, C. Leslie, and L. D. Marks, Appl. Phys. Lett. **72**, 314 (1998).

[52] E. Bengü and L. D. Marks, Phys. Rev. Lett. **86**, 2385 (2001).

[53] S. Azevedo, J. R. Kaschny, C. M. C. de Castilho, and F. de Brito Mota, Nanotechnology **18**, 495707 (2007).

[54] A. Zobelli, C. P. Ewels, A. Gloter, G. Seifert, O. Stephan, S. Csillag and C. Colliex, Nano Letters **6**, 1955 (2006).

[55] A. Y. Liu, R. M. Wentzcovitch, and M. L. Cohen, Phys. Rev. B **39**, 1760 (1989).

[56] E. Knittle, R. B. Kaner, R. Jeanloz, and M. L. Cohen, Phys. Rev. B **51**, 12149 (1995).

[57] V. L. Solozhenko, D. Andrault, G. Fiquet, M. Mezouar, and D. C. Rubie, Appl. Phys. Lett. **78**, 1385 (2001).

[58] M. Kawaguchi, Y. Imai, N. Kadowaki, Intercalation Chemistry of Graphite-like Layered Material BC6N for Anode of Li Ion Battery, J. Phys. Chem. Solids **67**, 1084-1090 (2006).

[59] S. Umeda, T. Yuki, T. Sugiyama, and T. Sugino, Diam. Relat. Mater. **13**, 1135 (2004).

[60] D. Watanabe, H. Aoki, R. Moriyama, M. K. Mazumder, C. Kimura, and T. Sugino, Diamond and Related Materials **17**, 669-672 (2008).

[61] E. Bengu, M.F. Genisel, O. Gulseren and R. Ovali, Thin Solid Films **518**, 1459-1464 (2009).

[62] M. Endo, T. Hayashi, Y. A. Kim, M. Terrones, and M. S. Dresselhaus, Phil. Trans. R. Soc. Lond. A **362**, 2223-2238 (2004).

[63] A. K. Geim and K. S. Novoselov, Nature Materials **6**, 183-191 (2007)

[64] M. J. Allen, V. C. Tung, and R. B. Kaner, Chem. Rev. **110**, 132-145 (2010).

[65] K. S. Novoselov, A. K. Geim, S. V. Morozov, D. Jiang, Y. Zhang, S. V. Dubonos, I. V. Grigorieva, and A. A. Firsov, Science **306**, 666-669 (2004).

[66] K. S. Novoselov, A. K. Geim, S. V. Morozov, D. Jiang, M. I. Katsnelson, I. V. Grigorieva, S. V. Dubonos, and A. A. Fursov, Nature **438**, 197-200 (2005).

[67] Y. Zhang, Y-W. Tan, H. L. Stormer, and P. Kim, Nature **438**, 201-204 (2005).

[68] J. Wu, W. Pisula, and K. Müllen, Chem. Rev. **107**, 718-747 (2007).

[69] A. H. C. Neto, F. Guinea, N. M. R. Peres, K. S. Novoselov, and A. K. Geim, Rev. Mod. Phys. **81**, 1 (2009).

[70] J. Dai, J. Yuan, and P. Giannozzi, Appl. Phys. Lett. **95**, 232105 (2009).

[71] S. Y. Zhou, D. A. Siegel, A. V. Federov, and A. Lanzara, Phys. Rev. Lett. **101**, 086402 (2008).

[72] L. Rosales, M. Pacheco, Z. Barticevic, A. Latgé, and P. A. Orellana, Nanotechnology **20**, 095705 (2009).

[73] J. Berashevich, and T. Chakraborty, Phys. Rev. B **80**, 033404 (2009).

[74] R. M. Ribeiro, N. M. R. Peres, J. Coutinho, and P. R. Briddon, Phys.Rev. B **78**, 075442 (2008).

[75] P. A. Denis, R. Faccio, and A. W. Mombru, ChemPhysChem **10**, 715-722 (2009).

[76] X. Wang, X. Li, L. Zhang, Y. Yoon, P. K. Weber, H. Wang, J. Guo, and H. Dai, Science **324**, 768-771 (2009).

[77] J. O. Sofo, A. S. Chaudhari, and G. D. Barber, Phys. Rev. B **75**, 153401 (2007).

[78] I. Zanella, S. Guerini, S. B. Fagan, J. M. Filho, and A. G. S. Filho, Phys. Rev. B **77**, 073404 (2008).

[79] A. A. Avetisyan, B. Partoens, and F. M. Peeters, Phys. Rev. B **79**, 035421 (2009).

[80] M. Y. Han, B. Özyilmaz, Y. Zhang, and P. Kim, Phys. Rev. Lett. **98**, 206805 (2007).

[81] Y-W. Son, M. L. Cohen, and S. G. Louie, Phys. Rev. Lett. **97**, 216803 (2006).

[82] P. Shemella, Y. Zhang, M. Mailman, P. M. Ajayan, and S. K. Nayak, App. Phys. Lett. **91**, 042101 (2007).

[83] S. Souma, M. Ogawa, T. Yamamoto, and K. Watanabe, J. Comput. Electron. **7**, 390-393 (2008).

[84] Y. P. Chen, Y. E. Xie, and X. H. Yan, J. Appl. Phys. **103**, 063711 (2008).

[85] M. Han, B. Özyilmaz, Y. Zhang, P. Jarillo-Herero, and P. Kim, Phys. Status Solidi B **244**, 11, 4134 (2007).

[86] S. Hong, Y. Yoon, and J. Guo, Appl. Phys. Lett. **92**, 083107 (2008).

[87] R. N. C. Filho, G. A. Farias, and F. M. Peeters, Phys. Rev. B **76**, 193409 (2007).

[88] D. S. Novikov, Phys. Rev. Lett. **99**, 056802 (2007).

[89] E-J. Kan, Z. Li, J. Yang, and J. G. Hou, Appl. Phys. Lett. **91**, 243116 (2007).

[90] J. Fernández-Rossier, J. J. Palacios, and L. Brey, Phys. Rev. B **75**, 205441 (2007).

[91] S. Okada, Phys. Rev. B **77**, 041408(R) (2008).

[92] O. Hod, J. E. Peralta, and G. E. Scuseria, Phys. Rev. B **76**, 233401 (2007).

[93] L. A. Agapito, and H-P. Cheng, J. Phys. Chem. C **111**, 14266-14273 (2007).

[94] R. Saito, G. Dresselhaus, and M. S. Dresselhaus, *Physical Properties of Carbon Nanotubes*, Imperial College Press, (2003).

[95] S. Iijima, Nature **254**, 56-58 (1991).

[96] Z. Yao, H. W. C. Postma, L. Balents, and C. Dekker, Nature **402**, 273-276 (1999).

[97] S. J. Tans, A. R. Verschueren, and C. Dekker, Nature **393**, 49-52 (1998).

[98] M. S. Fuhrer, J. Nygárd, L. Shih, M. Forero, Y-G. Yoon, M. S. C. Mazzoni, H. J. Choi, J. Ihm, S. G. Louie, A. Zettl, and P. L. McEuen, Science **288**, 494-497 (2000).

[99] E. Frackowiak and F. Béguin, Carbon **40**, 1775-1787 (2002).

[100] P. Chen, X. Wu, J. Lin, and K. L. Tan, Science **285**, 91-93 (1999).

[101] A. Chambers, C. Park, R. T. K. Baker, and N. M. Rodriguez, J. Phys. Chem. B **102**, 22 (1998).

[102] J. R. Wood, Q. Zhao, M. D. Frogley, E. R. Meurs, A. D. Prins, T. Peijs, D. J. Dunstan, and H. D. Wagner, Phys. Rev. B **62**, 11 (2000).

[103] S. Chopra, A. Pham, J. Gaillard, A. Parker, and A. M. Rao, Appl. Phys. Lett. **80**, 4632-4634 (2002).

[104] J-C. Charlier, M. Terrones, M. Baxendale, V. Meunier, T. Zacharia, N. L. Rupesinghe, W. K. Hsu, N. Grobert, H. Terrones, and G.A.J. Amaratunga, Nano Lett. **2**, 1191-1195 (2002).

[105] H. Dai, J. H. Hafner, A. G. Rinzler, D. T. Colbert, and R. E. Smalley, Nature **384**, 147-150 (1996).

[106] J. M. Romo-Herrara, B. G. Sumper, D. A. Cullen, H. Terrones, E. Cruz-Silva, D. J. Smith, V. Meunier, and M. Terrones, Angew. Chem. Int. Ed. **47**, 2948-2953 (2008).

[107] G. H. Du, W. Z. Li, Y. Q. Liu, Y. Ding, and Z. L. Wang, J. Phys. Chem. C **111**, 14293-14298 (2007).

[108] F. L. Deepak, A. Govindaraj, and C. N. R. Rao, Chem. Phys. Lett. **345**, 5-10 (2001).

[109] G. Küçükayan, R. V. Ovalı, S. İlday, B. Baykal, H. Yurdakul, S. Turan, O. Gülseren, and E. Bengü, Submitted to Carbon (unpublished work).

[110] J. Dai, and J. Yuan, J. Phys.: Condens. Matter **22**, 225501 (2010).

[111] P. A. Denis, Chem. Phys. Lett. **492**, 251-257 (2010).

[112] N. Demoncy, O. Stéphan, N. Brun, C. Colliex, A. Loiseau, and H. Pascard, Synthetic Metals **103**, 2380-2383 (1999).

[113] M. S. Mohlala, X-Y. Liu, M. J. Witcomb, and N. J. Coville, Appl. Organometal. Chem. **21**, 275-280 (2007).

[114] A. L. E. Garcia, S. E. Baltazar, A. H. Romero, J. F. P. Robles, and A. Rubio, J. Comput. Theor. Nanosci. **5**, 1-9 (2008).

[115] M. Methfessel and A. T. Paxton, Phys. Rev. B **40**, 3616 (1989).

[116] G. E. Scuseria, Chem. Phys. Lett. **195**, 534 (1992).

[117] L. Chernozatonskii, Phys. Lett. A **172**, 173 (1992).

[118] A. N. Andriotis, M. Menon, D. Strivastava, and L. Chernozatonskii, Phys. Rev. Lett. **87**, 066802 (2001).

[119] V. Meunier, M. B. Nardelli, J. Bernholc and T. Zacharia, Appl. Phys. Lett. **81**, 5234 (2002).

[120] J. M. Romo-Herrera, M. Terrones, H. Terrones, S. Dag and V. Meunier, Nano Lett. **7**, 570 (2007).